VALIDATION OF OXYGEN-16 IRON-56 COPPER-63 AND COPPER-65 ENDF/B-VIII.0 CROSS SECTION PERFORMANCE IN CRITICALITY SAFETY BENCHMARKS

A Dissertation
Presented to
The Academic Faculty

by

Alex Shaw

In Partial Fulfillment
of the Requirements for the Degree
Master's in Nuclear Engineering in the
George W. Woodruff School of Mechanical Engineering

Georgia Institute of Technology
May 2020

VALIDATION OF OXYGEN-16 IRON-56 COPPER-63 AND COPPER-65 ENDF/B-VIII.0 CROSS SECTION PERFORMANCE IN CRITICALITY SAFETY BENCHMARKS

Approved by:

Dr. Farzad Rahnema, Advisor
School of Mechanical Engineering
Georgia Institute of Technology

Dr. Douglas Bowen
Nuclear Data and Criticality Safety
Oak Ridge National Laboratory

Dr. Dingkang Zhang
School of Mechanical Engineering
Georgia Institute of Technology

Dr. Andrew Holcomb
Nuclear Data and Criticality Safety
Oak Ridge National Laboratory

Date Approved: April 13, 2020

ACKNOWLEDGEMENTS

This research was performed using funding received from the DOE Nuclear Criticality Safety Program. Additionally, the access and use of the Oak Ridge National Laboratory's High-Performance Computing cluster Romulus was instrumental in producing the data reported. ORNL staff assistance and guidance is greatly appreciated, particularly the oversight and technical assistance from Drs. Andrew Holcomb, Doug Bowen, and BJ Marshall.

TABLE OF CONTENTS

LIST OF TABLES

LIST OF FIGURES

LIST OF SYMBOLS AND ABBREVIATIONS

NCSP	Nuclear Criticality Safety Program
ORNL	Oak Ridge National Laboratory
LANL	Los Alamos National Laboratory
ICSBEP	International Criticality Safety Benchmark Evaluation Project
DICE	Database for the International Criticality Safety Benchmark Evaluation Project
NNDC	National Nuclear Data Center
ENDF	Evaluated Nuclear Data File
CIELO	Collaborative International Evaluated Library Organization
HMF	Highly Enriched Uranium Metal Fast ICSBEP Identifier
HMI	Highly Enriched Uranium Metal Intermediate ICSBEP Identifier
HMT	Highly Enriched Uranium Metal Thermal ICSBEP Identifier
HST	Highly Enriched Uranium Solution Thermal ICSBEP Identifier
IMF	Intermediate Enriched Uranium Metal Fast ICSBEP Identifier
IMI	Intermediate Enriched Uranium Metal Intermediate ICSBEP Identifier
LCT	Low Enriched Uranium Compound Thermal ICSBEP Identifier
PMF	Plutonium Metal Fast ICSBEP Identifier
PST	Plutonium Solution Thermal ICSBEP Identifier
SMF	Special Isotope Metal Fast ICSBEP Identifier
C/E	Ratio of Calculated Criticality Eigenvalue to Evaluated Benchmark Experimental Criticality Eigenvalue
$\Delta k/\Delta\Sigma$	Criticality Eigenvalue Sensitivity to Cross-Section Change
eV	Electron-volt

keV	Kiloelectron-volt
MeV	Megaelectron-volt
k_{eff}	Criticality Eigenvalue
pcm	Per-cent milli; 10^{-5}

SUMMARY

Nuclear data detailing the interactions between various fundamental particles is the very center of nuclear science and engineering, foremost among them the multitude of reactions an incident neutron can undergo. Such reactions are exceptionally difficult to measure, and vary substantially based on the material, chemical bonding, incident energy and angle, and material temperature. A large component of these nuclear data are the neutron cross sections, which describe the probability of neutrons undergoing various reactions as functions of said parameters. With so many parameters there is considerable error in even the most rigorous experimental observations and evaluations, resulting in periodic revisions to the accepted values.

One of the most used and accepted compilations of this data are the Evaluated Nuclear Data Files (ENDF) libraries. The eighth major release of the ENDF library, ENDF/B-VIII.0, was released in 2018 as the revision to the 2011 release of ENDF/B-VII.1. The limits of the accuracy of ENDF data are recognized, and as a result, efforts are taken to independently validate the performance of the library, particularly relative to past revisions. A primary method of such validation is the use of independent criticality safety and reactor physics experiments performed at a variety of laboratories worldwide. This work aims to examine the accuracy of criticality eigenvalues produced by the ENDF/B-VIII.0 library relative to the ENDF/B-VII.1 library, regarding several materials of interest, by comparing calculated and experimental criticality eigenvalues. Materials of interest were several of those recently evaluated as a part of the Nuclear Criticality Safety Program

(NCSP): Oxygen-16 (^{16}O), Iron-56 (^{56}Fe), Copper-63 (^{63}Cu), Copper-65 (^{65}Cu), and the natural elemental composition of Copper (69.15% ^{63}Cu and 30.85% ^{65}Cu).

In order to determine the performance of cross section revisions for these materials of interest, such materials must be a part of the experiments performed, and closely correlated to the effective multiplication factor (criticality eigenvalue). Benchmarked critical experiments were selected based on a high cross section total integrated sensitivity, a quantitative measure of the criticality impact due to a change in cross section values. These experiments were then modeled in the CSAS Monte Carlo sequence of the SCALE code system, developed and distributed by Oak Ridge National Laboratory (ORNL). SCALE results were cross-checked with MCNP in most cases for full library substitution calculations for confirmation of criticality values. In total, 102 benchmarked experimental configurations were selected; 63 exhibiting sensitivity to ^{16}O, 32 to all copper variants, and 25 to ^{56}Fe. Experiments were modeled in SCALE using the full ENDF/B-VII.1 library, the ENDF/B-VII.1 library with ENDF/B-VIII.0 substitutions for individual isotopes of interest, and the full ENDF/B-VIII.0 library.

With calculated results, ratios of the calculated criticality eigenvalue to the benchmark experimental criticality eigenvalue (C/E) could be determined. The lesser the deviation from unity, the better the accuracy of the nuclear data in a singular experimental configuration; different configurations have different spectra, materials, geometries, and as a result, sensitivities. With a full set of sensitive experiments, trends and averages can be established. These averages include the following for models of systems sensitive to:

i. ^{16}O, with isotope substitution yielding an average decrease in C/E of 137.4 pcm; a 0.34σ increase in the average deviation relative to experimental uncertainty

ii. ^{56}Fe, with isotope substitution yielding an average increase in C/E of 30.7 pcm; a 0.07σ decrease in the average deviation relative to experimental uncertainty

iii. ^{63}Cu, with isotope substitution yielding an average decrease in C/E of 520.2 pcm; a 1.51σ decrease in the average deviation relative to experimental uncertainty

iv. ^{65}Cu, with isotope substitution yielding an average increase in C/E of 90.1 pcm; a 0.51σ increase in the average deviation relative to experimental uncertainty

v. Elemental copper ($^{63,65}Cu$), with the substitution of both copper isotopes yielding an average decrease in C/E of 443.5 pcm; a 1.39σ decrease in the average deviation relative to experimental uncertainty

Additionally, to measure the overall performance of the ENDF/B-VIII.0 library relative to the ENDF/B-VII.1 library for selected models, the ENDF/B-VII.1 library was replaced by ENDF/B-VIII.0 for all materials. This change in library resulted in an average decrease in C/E of 125.9 pcm, with a 0.56σ decrease in the average deviation relative to experimental uncertainty.

Given an increase in average deviation, or bias, relative to experimental uncertainty reflects less accurate cross section data, ^{16}O and ^{65}Cu ENDF/B-VIII.0 data have slightly worsened, whereas ^{63}Cu has considerable improvement, when contrasted to ENDF/B-VII.1 calculated and experimental agreement. The magnitude of change in ^{56}Fe is an insignificant improvement, and elemental copper improves, being majority ^{63}Cu. Those results still give insight, as an insignificant improvement for ^{56}Fe is better than a significant worsening, and modeling using copper will be based on experimental arrangements with

copper in its elemental form (i.e., using enriched copper of one isotope or the other is never done). Although these averages across all cases are within 2 sigma of experimental values, individual cases can show change greater than 2 sigma. Over all 102 configurations, the full ENDF/B-VIII.0 revision resulted in considerable improvement. Based on these results, while ENDF/B-VIII.0 cross sections for the selected benchmarks result in extensive improvements, there is the potential for improvement in ^{16}O and ^{65}Cu data.

CHAPTER 1. INTRODUCTION

Recently completed cross section evaluations sponsored by the US Nuclear Criticality Safety Program (NCSP) have been incorporated into the release of the Evaluated Nuclear Data File ENDF/B-VIII.0 cross section library [1, 2]. Evaluations of note include ^{16}O, ^{56}Fe, ^{63}Cu, and ^{65}Cu. Performance of this data requires validation relative to ENDF/B-VII.1 to determine the significance of recent revaluation. For ENDF/B-VIII.0 cross section testing and validation purposes, benchmarks models defined in the International Criticality Safety Benchmark Evaluation Project (ICSBEP) Handbook were selected based on an elevated sensitivity to these NCSP isotopes of interest [3]. Improvements in cross section performance were determined by substituting the isotope of interest with its ENDF/B-VIII.0 cross section and comparing criticality deviations from experimental values to those of the previous ENDFB-VII.1 release. Finally, as a measure of the full ENDF/B-VIII.0 library's performance, the entire ENDF/B-VIII.0 library was substituted in place of ENDF/B-VII.1 for all materials in the 102 benchmark configurations included in this paper.

Nuclear criticality safety entails the management of fissile materials as to prevent criticality accidents. Generally, criticality safety involves the storage of fresh or spent nuclear reactor fuel, the storage of fissile material for weapons, or the chemical processing of fissile material, particularly liquid chemistry for fuel production and reprocessing. In the situation where true experimental data is lacking for a criticality safety analysis of fissile material management or use, a validated computational method may be used, i.e., a radiation transport code, for estimation of the eigenvalue to ensure subcriticality. These radiation transport codes simulate the conditions of a situation in question, by modeling its

geometric, material, and temperature properties. These material and temperature inputs then utilize cross section data from cross section libraries for the appropriate nuclide and temperature to determine neutron propagation characteristics and reactions.

The fundamental characteristic of concern from these calculations, as per namesake, is the situation's criticality, the ability to maintain a chain reaction of fissions. Preventing chain reactions and maintaining subcriticality is the goal of criticality safety, to prevent radiation exposure to workers from fission events. However, the accuracy of criticality safety codes depends heavily on the accuracy of the nuclear data at the core of the neutronics calculations. That is to say, even high-fidelity methods are limited by the accuracy of the cross sections used to investigate the criticality, or k_{eff}. Therefore, the cross sections themselves must be validated so that their performance is known.

Cross section performance is key for their usage and meaning. Physically, so called microscopic cross sections represent the probability of the varying reactions a neutron can undergo with a material. These reactions include but are not limited to: elastic scattering, where an impinging neutron collides with and transfers kinetic energy to a target nucleus; inelastic scattering, where an impinging neutron collides with and excites a target nucleus in addition to the transfer of kinetic energy; and neutron induced fission, where an impinging neutron is captured by a fissionable nucleus, resulting in a fission event where the nucleus splits releasing gamma radiation and new neutrons. The likelihood of these events is characterized by the reaction's cross section, which depends on the impinging neutron's original kinetic energy as well as the target material.

With nuclear criticality safety aiming to prevent fissions, these competing reactions have varying effects on system criticality. For example, the ^{235}U fission cross section largely follows a "1/v" trend, with an increasing fission cross section with reduced neutron velocity and kinetic energy. Whereas a pure slab of ^{235}U may not have enough material to reach criticality, the introduction of elastic scattering, through a moderator or reflecting material, can lower the energy and increase the cross section (and therefore the likelihood of fission), or change the direction of neutrons so that they interact with more fissile material, again increasing the likelihood of fission. With many variables to account for in the determination of these cross sections, estimating their values is painstakingly difficult. In hopes of improving the data on cross sections, cross section libraries are periodically released so that reaction probabilities, and criticality eigenvalues, can more accurately be predicted.

With validated performance, real world applications can model critical configurations and account for known cross section biases accordingly. To ensure observed biases are meaningful, a high-fidelity method must be used to ensure accuracy. As the preeminent high-fidelity method to solve transport calculations, Monte Carlo codes directly sample the complete continuous-energy cross section with no simplifications or discretization; for this reason, Monte Carlo codes SCALE and MCNP were selected for validation. SCALE k_{eff} results were compared against MCNP and used for validation purposes and isotope substitutions.

Validation was completed relative to ENDF/B-VII.1, being the second most recent ENDF release, as to determine the effect of revisions on the standard choice of cross section library. Copper and its constituent isotopes were selected for validation based on noted

discrepancies between observed and calculated criticalities, particularly in recent critical assemblies. Additionally, its use as a structural material is of note for reactor and waste storage facilities. Oxygen and iron were both chosen for validation because of their dual inclusion in the list of CIELO isotopes and NCSP isotopes of interest [2, 4]. The CIELO program aims to increase international cooperation to reconcile cross section evaluations for crucial isotopes. Iron, as a main component in many reactor and storage systems, as well as critical assemblies, was of interest for the effect of resonance region cross section updates. Oxygen is of interest in many critical assemblies and general chemical processing, due to its presence in water. The next subsection goes into greater detail regarding the Background and Relevance of selected isotopes, as well as exhibited cross section changes.

Independent experiments related to the propagation of neutrons through these materials of interest were utilized to determine the accuracy of updated cross sections, by examining trends across a number of configurations with varying material quantities. This data gives feedback on whether new cross sections reflect more accurate revisions or require additional evaluation. The next chapter details the methods used for the selection of appropriate experiments, where sensitivity data representing the change in k_{eff} due to cross section variations were taken to quantitatively measure the significance of these materials. An overview of the standardized modeling techniques used is also given, detailing input parameters for SCALE and MCNP. Brief descriptions of selected experiments follow, with condensed geometric and material data identifying said significant materials of interest. With a sense of how experiments are configured and the role of the sensitive materials, comparisons between calculated and experimental k_{eff} results are given to show variations from ENDF/B-VIII.0 isotopic substitutions. These

data are then accordingly represented by their sensitivities, and the results of the entire ENDF/B-VIII.0 library are shown, and overall conclusions on performance summarized.

1.1 Background and Relevance

Beyond the total cross section sensitivities tabulated in APPENDIX A, sensitivity data is produced for every neutron reaction, including but not limited to elastic scattering, inelastic scattering, and radiative capture. Having estimates of these data from DICE, relevant reactions for the isotopes of interest can be prioritized. These reactions and their revisions between ENDF/B-VII.1 and ENDF/B-VIII.0 are summarized in the following sections [1, 5]. Figures detailing the ratios between ENDF/B-VIII.0 and ENDF/B-VII.1 were plotted using the National Nuclear Data Center's online ENDF tool and are readily available and reproducible [6].

1.1.1 Oxygen-16 Cross-Section Revisions

Oxygen is of interest due to its significant presence in reactors and critical assemblies, therefore its inclusion as a CIELO isotope. A key component of water, which is used as a moderator and solvent for critical assemblies and processing, oxygen is also present in Uranium Dioxide, a common uranium compound with a significant presence in fuel production and waste storage. In cases examined, the most sensitive and relevant reaction for ^{16}O was elastic scattering. In the ENDF/B-VIII.0 release, thermal and intermediate elastic scattering reduced on the order of 1.5%, shown in Figure 1. Given positive sensitivities to elastic scattering, a reduction in cross section would result in a reduction in the likelihood of criticality; such a guess is made with the understanding that there are other variables that may counter it. Additionally, as noted in the ENDF/B-VIII.0

release and Chadwick et al, while sensitivities to the $^{16}O(n,\alpha)^{13}C$ reaction are small and the reaction has a threshold around 2 MeV, the magnitude of the increase, on the order of 40%, in cross section from ENDF/B-VII.1 to ENDF/B-VIII.0 produces significant reductions in calculated criticality [1, 7]. Given this reaction is neutron capture, removing neutrons from the system, sensitivities will be negative as a result of the reduced neutron balance, resulting in additional expected negative reactivity. Particularly resonances, where impacts from changing resonances are too energy specific and variable to be useful in estimating variation. Additionally, there are changes in the fast region; several experiments have fast spectrums, which will dull the accuracy of this conjecture. However, with elastic scattering being the most relevant reaction sensitivity, coupled with a broad and considerable decrease, a reduction in criticality is expected in most cases.

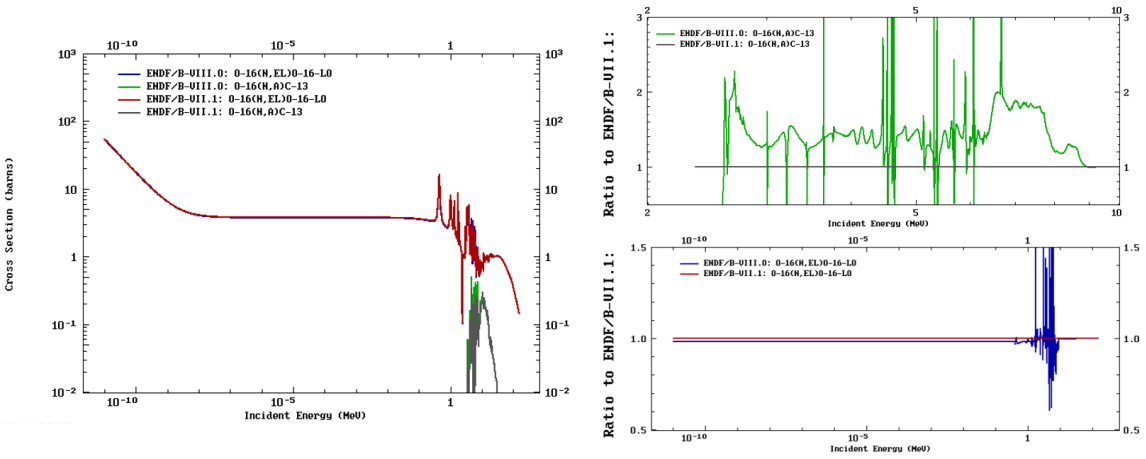

Figure 1– Oxygen-16 Thermal Scattering and (n,α) Absolute and Relative Changes (Figures from [6])

Previous validations confirm these expected changes [8]. Particularly regarding HST and LCT systems, the effect of the elastic scattering decrease and increase in capture and alpha production largely results in a reduction in the likelihood of criticality.

1.1.2 Iron-56 Cross-Section Revisions

A commonly used structural material included as a part of the CIELO project, there is interest in having more accurate iron cross section data, as it is found in reactor and critical assemblies worldwide. As structural material, critical assemblies having accurate cross sections is particularly relevant regarding benchmark simplifications. Were there to be significant cross section revisions, there could be inaccuracies as a result of the exclusion of structural material for geometry simplification. In cases examined, the most sensitive and relevant reactions for ^{56}Fe were elastic scattering, inelastic scattering, and radiative capture. While attempts at hypothesizing performance are convoluted as a result of multiple competing reactions, taking note that elastic reactions are the most sensitive reactions, with the fact that the second most relevant reaction inelastic scattering has a high energy threshold, lead to estimates based on changes and sensitivities to elastic scattering. As seen in Figure 2, thermal and intermediate elastic scattering is relatively stable, and marginally increased by about 0.25% relative to ENDF/B-VII.1. At fast energies, resonances become a major factor, reducing interpretive ability; above 10 MeV these resonances largely disappear in lieu of overall cross section decreases. However, this is well beyond the average neutron energy of fissions, and as a result inconsequential. Inelastic scattering at its onset is detailed by resonances, but at several MeV, there is a clear increase in cross section, which remains for the rest of energies of note for fission reactions. While not visible due to larger variations at higher energies, radiative capture increases at thermal energies by about 0.6%. In intermediate energies, the capture cross section background was artificially increased based on previously observed critical assembly

sensitivities to the energy region, in addition to adjusting resonance typos and resolving to a “1/v” trend [1, 7].

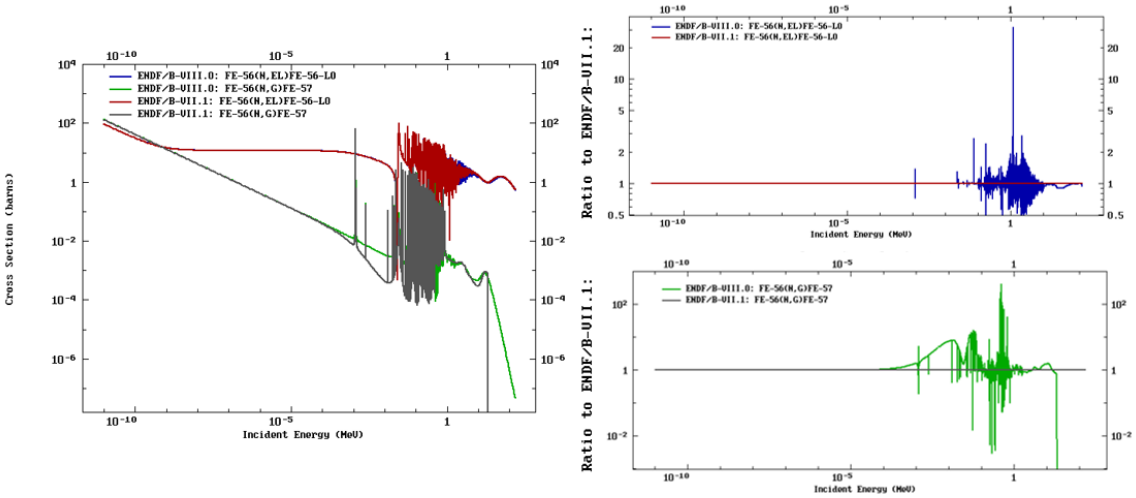

Figure 2– Iron-56 Elastic Scattering and Radiative Capture Absolute and Relative Changes (Figures from [6])

With positive sensitivities to elastic and inelastic scattering, and a negative sensitivity to capture, it is difficult to draw basic estimates on changes. Of note though, is that for thermal elastic and capture cross sections, changes are quite small; potentially statistically insignificant when propagated through Monte Carlo calculations. While inelastic scattering does have quite significant changes, these changes are at very high energies for a fission neutron source, and as a result unlikely to produce significant variations in even some of the faster spectrums. While elastic scattering is the more sensitive reaction, capture has larger variations as a countering effect; no conclusive estimate can be made. This lies within expectations based on Herman et al., where the introduction of the new CIELO data, incorporated into the ENDF/B-VIII.0 release, produced results where variations resulted in effective equivalency and minimal improvement, based on 24 separate benchmarks [8].

1.1.3 Copper-63 Cross-Section Revisions

Copper has been noted in multiple instances as a source of discrepancy between calculated and experimental data and was therefore noted by the DOE Nuclear Data Advisory Group as important for evaluation [1]. Copper, while also used as a minor structural material and trace element in alloys, is used as material for nuclear waste canisters, such as the KBS-3 copper shielded high level waste capsules in Sweden and Finland [9]. Particularly for waste storage, having accurate criticality data is incredibly vital to ensure subcriticality. Were cross sections to be inaccurate and underestimating criticality, circumstances could change to the point of reaching critical, resulting in a criticality accident. In cases examined, the most sensitive and relevant reactions for ^{63}Cu were elastic scattering, radiative capture, and inelastic scattering. Again, with multiple relevant reactions, the actual Monte Carlo simulations will provide the definite trends. As seen in Figure 3, thermal elastic scattering and radiative capture are unchanged relative to ENDF/B-VIII.0, but with significant reduction in the intermediate and fast energies.

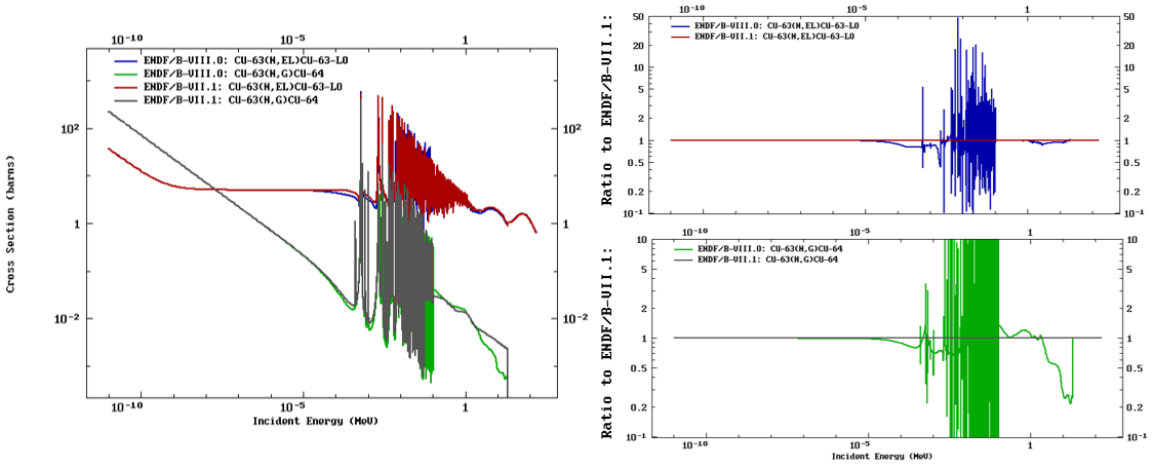

Figure 3– Copper-63 Elastic Scattering and Radiative Capture Absolute and Relative Changes (Figures from [6])

Intermediate energies see nearly a 20% reduction in scattering before reaching resonances, which then stabilize at the onset of fast energies. As energies increase to 1 MeV and higher, there is another significant decrease of 5-10% until values become irrelevant at 10 MeV. Inelastic scattering shows a clear increase by 10% or more for the entire range of viability. Following a similar trend as elastic scattering, intermediate energy radiative capture cross sections have a 20% reduction, before resonances. Where it differs however, is in initial fast energies between 100 keV and 1 MeV, where rather than being unchanged, capture cross sections increase up to 30%.

With positive sensitivities to elastic and inelastic scattering, and a negative sensitivity to capture, it is difficult to draw basic estimates on changes with large competing changes. A constant between revisions is the lack of variation in thermal cross sections. With similar changes in elastic scattering and capture, to estimate overall effect, the most prominent of the two must be investigated. Since intermediate and fast elastic scattering cross sections are about two orders of magnitude higher than capture cross sections, changes to elastic scattering will have a larger impact than to capture, reflected in their elevated sensitivities. While inelastic scattering does have quite significant changes, these changes are at high energies for a fission neutron source, and likely to be overshadowed by the broad and significant reductions in elastic scattering. Therefore overall, elastic scattering is expected to be the dominant source of criticality changes; with a decrease in cross section and a positive sensitivity, a reduction in k_{eff} is expected for ^{63}Cu experiments.

1.1.4 Copper-65 Cross-Section Revisions

As with ^{63}Cu, applications and reasoning behind accurate copper cross sections are the same for ^{65}Cu. In cases examined, the most sensitive and relevant reactions for ^{65}Cu were elastic scattering. As with ^{63}Cu, the intermediate and fast cross sections showed significant reduction. However, the overall change is muted in comparison. Figure 4 repeats the ^{63}Cu elastic scattering cross section on the left and plots the ^{65}Cu cross section on the right. Whereas at 10 eV (10^{-5} MeV in the image), ^{63}Cu has been reduced 10%, ^{65}Cu is just beginning to reduce. Further, the intermediate drop is less pronounced, with a lesser reduction over a shorter interval. The first resonance also appears earlier than for ^{63}Cu, interrupting the decrease in cross section, depressing the overall reduction. Based on the positive sensitivity to elastic scattering and reductions in the elastic scattering cross section, a reduction in k_{eff} is expected for ^{65}Cu experiments.

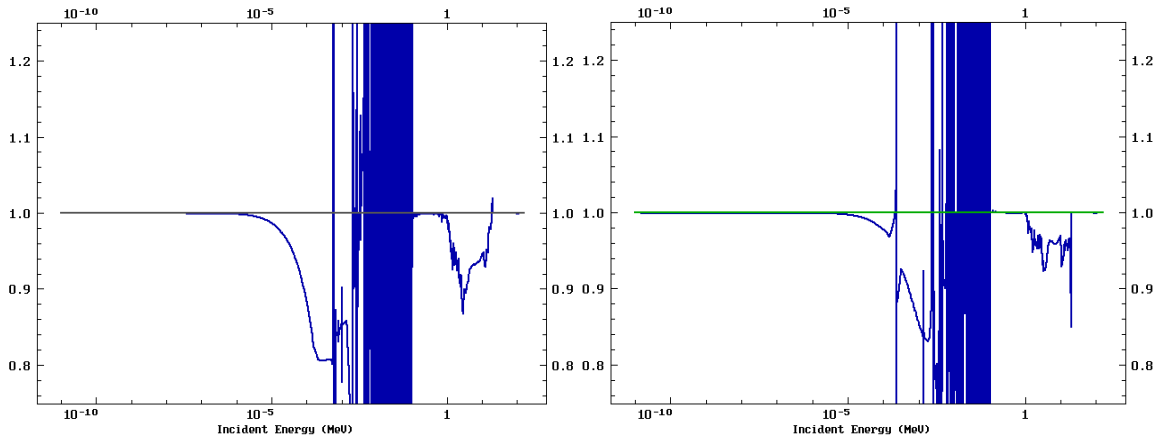

Figure 4– Copper-63 and Copper-65 Elastic Scattering Relative Changes (Figures from [6])

CHAPTER 2. METHODOLOGY OF BENCHMARK SELECTION AND MODELING

ICSBEP evaluations in the Appendices and throughout this paper are referred to by their evaluation identifier expressed in shorthand. For example, HEU-MET-INTER-006-001 is referred to as HMI-006-001.

2.1 Appropriate Benchmark Experiment Selection

To determine cross section performance, the ICSBEP Handbook was consulted for the selection of evaluated experiments with a neutronically significant quantity of ^{16}O, ^{56}Fe, ^{63}Cu, and ^{65}Cu. The included Database for the International Criticality Safety Benchmark Evaluation Project (DICE) program, a database of ICSBEP identifying information, key parameters, and experimental data was used to search the available sensitivity data for oxygen iron and copper sensitivities of 0.01 $\%\Delta k/\%\Delta\Sigma$ or greater [10]. While DICE does not contain sensitivity data for all evaluations, 85% of evaluations have such data pre-produced and included. Limiting benchmark integral total reaction sensitivities to 0.01% or greater aims to reduce the impact of computational uncertainties on any potential variations in criticality. Higher sensitivities allow for variations as a result of cross section changes to be noticeable, if any.

Sensitivities to cross section reactions are as defined in Equation 1, to a neutron reaction x. . ϕ and $\phi^{\dagger}$ represent the forward and adjoint neutron flux, respectively By utilizing the adjoint neutron flux, the effective importance of an individual reaction and material is determined; the adjoint flux effectively representing a “backwards” transport calculation. With the fission operator (B) and transport operator (A), the neutron transport equation is integrated over all spatial and energy variables to produce the sensitivity. The

sensitivity of the criticality eigenvalue (k) to the cross section (Σ) is a derivative of the change in criticality with respect to macroscopic cross section changes. As macroscopic cross sections are density dependent, a sample of density perturbations for confirmation of produced sensitivities are provided in APPENDIX D.

$$S_{k,\Sigma_{x,g}} = \frac{\partial k_{eff}/k_{eff}}{\partial \Sigma_{x,g}/\Sigma_{x,g}}$$

$$S_{k,\Sigma(\mathrm{r})} = \frac{\partial k/k}{\partial \Sigma(\mathrm{r})/\Sigma(\mathrm{r})} = -\frac{\Sigma(\mathrm{r})}{k}\frac{\langle \phi^{\dagger}(\xi)\left(\frac{\partial A[\Sigma(\xi)]}{\partial \Sigma(\mathrm{r})} - \frac{1}{k}\frac{\partial B[\Sigma(\xi)]}{\partial \Sigma(\mathrm{r})}\right)\phi(\xi)\rangle}{\langle \phi^{\dagger}(\xi)\frac{1}{k^2}B[\Sigma(\xi)]\phi(\xi)\rangle} \quad (1)$$

In the instances of oxygen and iron, the set of sensitive experiments were drawn from a preselected and prioritized collection of benchmarks sensitive to various other NCSP materials of interest. They still represent a large suite of oxygen and iron sensitive experiments; additionally, the sheer number of iron and oxygen sensitive benchmark configurations (on the order of several thousand) is beyond the capability of one individual. While not explicitly chosen initially for their oxygen and iron sensitivities, the selection process remained the same despite drawing from a smaller pool of cases. Despite the different experiment selection pool, DICE was applied to search the available sensitivity data for oxygen, iron, and copper sensitivities of 0.01%Δk/%ΔΣ or greater. 0.01% was selected as the lower bound on sensitivity, as it is equivalent to 10 pcm/%ΔΣ, a 10 pcm change in criticality per percent change in cross section; a total cross section increase (equivalent to an increase in number density) of 1% results in a 10 pcm change in criticality.

Using 0.01%, the lower bound on change in criticality is 10 pcm for every percent change in cross sections; while sensitivity is spectrum dependent and cross section changes

are not necessarily a full percent change, 10 pcm correlates to the computational uncertainty used in calculations. Thus, limiting benchmarks to 0.01% or greater aims to reduce the impact of computational uncertainties in any potential variations in criticality. As natural copper is comprised of both ^{63}Cu and ^{65}Cu, and natural oxygen and iron are majority (by greater than a factor of 10) comprised of ^{16}O and ^{56}Fe, the sensitivity search included natural abundance oxygen iron and copper sensitivity data, as well as isotope specific sensitivities. As copper has more pronounced and energy localized cross section changes from ENDF/B-VII.1 to ENDF/B-VIII.0, DICE sensitivities were further parsed for 0.01% sensitivity in intermediate or fast spectrums only. As a result, all configurations used in the validation of copper cross sections were intermediate and fast evaluations from the handbook. The ICSBEP method for determining the spectrum identifier is as quoted below [3]:

"In [the ICSBEP] handbook, fast, intermediate and thermal systems are defined as systems in which more than 50% of the fissions occur at energies greater than 100 keV, from 0.625 eV to 100 keV, and less than 0.625eV, respectively."

The full set of selected experiments for ^{16}O ^{56}Fe ^{63}Cu and ^{65}Cu are listed in APPENDIX A; By Isotope with their benchmark experimental criticality and associated uncertainty, as well as their calculated ENDF/B-VII.1 total cross section sensitivity. While DICE was used for the selection of benchmarks, DICE sensitivity data is largely a result of automated sensitivity calculations. Sensitivity data produced by DICE may be obsolete for several reasons, as most calculations were performed using outdated cross section libraries, and recent revisions to the ICSBEP evaluations may not be accounted for. While such effects may be negligible, it is simpler to let the computer cluster run to known standards than to investigate the accuracy of every configuration's preproduced sensitivities. Additionally, as uncertainty in the sensitivity data is not standardized or directly given in DICE, sensitivity data were reproduced to have a known standard of the sensitivity precision. For more precise sensitivity data used for analysis, self-constructed

SCALE CSAS inputs were altered to SCALE TSUNAMI inputs so that sensitivity data directly related to the same criticality calculation input conditions [12]. These results are the ENDF/B-VII.1 sensitivity data reported in APPENDIX A.

2.2 Modeling Methods

After the selection of appropriate benchmarks, configurations were modeled in the continuous-energy Monte Carlo SCALE 6.2.3 CSAS sequence, as well as in MCNP 6.2 for the validation of most CSAS results [13, 14]. Models were run using both ENDF/B-VII.1 and ENDF/B-VIII.0 libraries. For CSAS calculations, the least computationally intensive of 2 options were used in the parameters block. CSAS calculations were run to either a computational uncertainty of 10 pcm, or to the full parameter specifications of 10150 generations with 15000 particles per generation. 150 generations were skipped, resulting in 10000 active generations and 150 million potential particle histories. However, every configuration required less than 150 million histories before converging to 10 pcm uncertainty. 10 pcm was chosen to allow for a more efficient modeling process, as reducing uncertainty is generally proportionally quadratic with time, and 10 pcm relative to experimental uncertainty is negligible. Effectively, C/E values for 10 pcm as opposed to say, 5 pcm, are functionally equivalent in exchange for requiring approximately a quarter of the computational time.

However, for sensitivity data and analysis, SCALE TSUNAMI calculations were performed to a higher degree of precision; sensitivity and uncertainty data have higher degrees of error, as the separation into individual reactions of individual materials and isotopes reduces sampling histories to converge on. Therefore, TSUNAMI calculations made from modified CSAS inputs were run to either a computational uncertainty in the

replicated criticality search of 5 pcm, or 26500 generations with 25000 particles per generation, and 2500 generations skipped. The TSUNAMI CLUTCH method for continuous-energy sensitivity calculations was utilized, with a 1 cm uniform mesh and 10 latent generations. CLUTCH was selected over the Iterative Fission Probability (IFP) method due to its parallel computing capabilities and lower memory footprint.

MCNP parameters were set to run 150000 particles per generation, with 3050 generations. 150 cycles were inactive, leaving 2900 active cycles and 435 million active particle histories. MCNP does not have an uncertainty limiting parameter, so 435 million histories were performed, resulting in uncertainties ranging from 3 to 7 pcm based on the simplicity of the model. In instances where CSAS and MCNP results were not sufficiently computationally equivalent (generally taken to mean over 50 pcm difference, or about 3-4 sigma of propagated uncertainty), the change in both codes from ENDF/B-VII.1 to ENDF/B-VIII.0 was compared instead to determine the similarity between criticality changes from ENDF/B-VIII.0.

While differences in criticality calculations or cross section processing may result in the statistically different results, the scope of this project is not to discover discrepancies between the two calculating methods. Rather, determining the effect of new ENDF/B-VIII.0 cross sections is the goal. It is assumed that even though there may be absolute discrepancies, the change to the cross-section data will appropriately affect the calculations themselves in the same way. Using this view as well as the general computational equivalency between results, nearly all models resulted in similar changes from cross section substitutions. Thus, the comparison between CSAS and MCNP relative changes as a result of ENDF/B-VII.1 to ENDF/B-VIII.0.

Models were constructed according to Section 3 benchmark specifications of the corresponding ICSBEP evaluation, as well as structured around the nearly correct inputs often included in various appendices of the evaluation. CSAS calculations were performed for the ENDF/B-VII.1 library, a base ENDF/B-VII.1 library with ^{16}O, ^{56}Fe, ^{63}Cu, and ^{65}Cu ENDF/B-VIII.0 cross sections, and the ENDF/B-VIII.0 library. Additionally, copper sensitive benchmarks were run with both ^{63}Cu and ^{65}Cu ENDF/B-VIII.0 cross sections to determine the effect of revisions on natural copper performance. MCNP calculations were performed for the ENDF/B-VII.1 library and ENDF/B-VIII.0 library.

Specifically, the CSAS geometry block and MCNP surface and cell cards were built from ICSBEP Section 3.2, Dimensions. The CSAS composition block and MCNP data card were built from ICSBEP Section 3.3, Materials. ICSBEP Section 3.4, Temperature was rarely required, as most assemblies were at room temperature, or assessed to have no temperature effect based on the experimental temperature deviation from evaluated temperature. ICSBEP Section 3.5, Experimental and Benchmark-Model k_{eff}, was used to supply the benchmark experimental criticality and uncertainty values located in Appendix A; also referred to as the E values.

ENDF/B-VII.1 data libraries are included in the public release of both SCALE 6.2.3 and MCNP 6.2. For SCALE calculations, ENDF/B-VIII.0 criticality and sensitivity calculations were performed on the Oak Ridge National Laboratory (ORNL) Romulus Linux cluster. ENDF/B-VIII.0 AMPX data was used by accessing libraries ready for release with the SCALE 6.3 Beta testing, and eventual full release. MCNP ENDF/B-VIII.0 ACE libraries can be found provided online by Los Alamos National Lab (LANL) and downloaded and added to xsdir file listings [15]. After full library comparisons were made

in SCALE and MCNP, SCALE was chosen as the code for testing impacts of individual isotope substitions. SCALE was chosen for its familiarity in a Linux HPC cluster environment, the project link to ORNL, the package's TSUNAMI sensitivity sequence, and governable uncertainty limits. This work could be corroborated in MCNP with the appropriate cross section data, variation of the ZAID library identifiers, and the WHISPER sensitivity module.

KENO inputs for CSAS isotopic substitution calculations were altered to include a shell script provided by Dr. Andrew Holcomb, which linked self-constructed xml files containing a mix of ENDF/B-VII.1 and ENDF/B-VIII.0 directories [16]. Figure 6 shows a censored version of said shell script. For isotopes of interest, the original base library listing was deconstructed, removing the data paths for said isotopes, and saving the remaining data into a new base library listing. The base library listing referenced in the figure is the new and altered base, free of isotopes of interest.

This was done for both the ENDF/B-VII.1 and ENDF/B-VIII.0 libraries. For every isotope this is done for, two specific xml files per isotope were generated. As shown, this was done for seven isotopes: ^{1}H, ^{16}O, ^{56}Fe, ^{235}U, ^{238}U, ^{63}Cu, and ^{65}Cu. Therefore, there were the two base libraries, and 14 isotope xml files, an ENDF/B-VII.1 and ENDF/B-VIII.0 file for each of the seven isotopes after deconstruction. Of interest in this work are the variations as a result of ^{16}O, ^{56}Fe, ^{63}Cu, ^{65}Cu, and the full library. In order to use the script and substitute specific isotope libraries, this script is affixed to the beginning of the CSAS input file and adjusted to the isotope of interest accordingly. For instance, in the figure, the base library and all isotopes other than ^{56}Fe are ENDF/B-VII.1, while ^{56}Fe uses ENDF/B-VIII.0 data.

```
=shell
ln -fs ***ENDF/B-VII.1 Base Library*** .
ln -fs ***ENDF/B-VIII.0 Base Library*** .
ln -fs ***ENDF/B-VIII.0 Library ID*** sclib
cat ***/isotope_swap/PHYSOR/***ENDF/B-VII.1 Base Library*** > temp0.xml
cat temp0.xml ***/isotope_swap/PHYSOR/endf71_H-1.xml   > temp1.xml
cat temp1.xml ***/isotope_swap/PHYSOR/endf71_O-16.xml  > temp2.xml
cat temp2.xml ***/isotope_swap/PHYSOR/endf80_Fe-56.xml > temp3.xml
cat temp3.xml ***/isotope_swap/PHYSOR/endf71_U-235.xml > temp4.xml
cat temp4.xml ***/isotope_swap/PHYSOR/endf71_U-238.xml > temp5.xml
cat temp5.xml ***/isotope_swap/PHYSOR/endf71_Cu-63.xml > temp6.xml
cat temp6.xml ***/isotope_swap/PHYSOR/endf71_Cu-65.xml > temp7.xml
cat temp7.xml ***/isotope_swap/PHYSOR/end_library.xml  > ce_mixed.xml
rm temp*xml
end

=csas5
HST-015 Case2
ce_mixed
```

Figure 5– SCALE Isotope Substitution Shell Script

The script is affixed to all configurations utilizing ENDF/B-VIII.0 data listed in this work and varied based on the analysis being performed and the sensitivities of the configuration. Isotope data is incrementally coupled to the base library with temporary xml files and stored into an arbitrarily named ce_mixed.xml file. ce_mixed.xml is called by modifying the library name in the input to ce_mixed, which will then reference the constructed xml files for cross section data.

In doing so, CSAS calculations were performed for a base ENDF/B-VII.1 library with, individually ^{16}O, ^{56}Fe, ^{63}Cu, and ^{65}Cu ENDF/B-VIII.0 cross sections, by varying the specific isotope xml from endf71 to endf80. Additionally, copper sensitive benchmarks were run with both ^{63}Cu, and ^{65}Cu ENDF/B-VIII.0 cross sections, to determine the effect of evaluations on natural copper. For the full ENDF/B-VIII.0 library substitution, temp0.xml is assigned the ENDF/B-VIII.0 base library, and all isotopic xml files are set to endf80.

CHAPTER 3. BENCHMARK DESCRIPTIONS

All experiments were taken from the ICSBEP handbook as acceptable benchmark evaluations. More detailed descriptions and figures of the benchmark models can be found in Section 3 of the referenced handbook's evaluation. While most evaluations have multiple configurations per evaluation, the general specifications of each overall evaluation are described, as well as the varying parameters for different configurations. Benchmark experimental criticalities, uncertainties, and sensitivities are tabulated in APPENDIX A, pulled from the referenced evaluations as follow.

3.1 HEU-MET-FAST-072: ZEUS: Fast-Spectrum Critical Assemblies with an Iron-HEU Core Surrounded by a Copper Reflector [16]

This set of experiments, part of the ZEUS experiments performed at LANL, exhibited sensitivities to iron and copper. The evaluation contains three configurations, all three of which are copper and iron sensitive. The general geometry of the assembly consists of interspersed HEU and iron plates, and in the third configuration polyethylene plates, and is displayed in Figure 7. Various aluminium support structures are shown as grey; HEU plates are shown in black and surrounded by 4 iron plates shown in green on either side. Copper reflector is shown in orange surrounding the core. The first configuration is as shown; the second has a removed support shim, and shorter radial reflector; the third configuration has additional interspersed polyethylene slivers with a shorter radial copper reflector and central core.

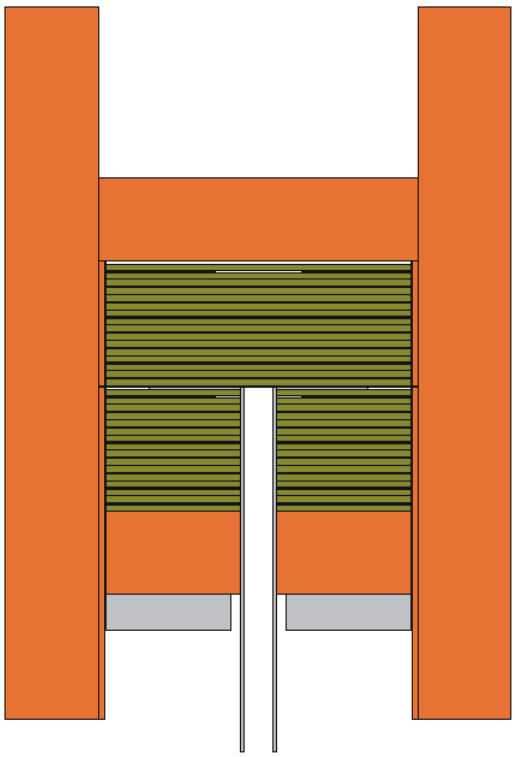

Figure 6– HEU-MET-FAST-072 Vertical Cross Section (Figure from [16])

A horizontal cross section is shown in Figure 8. All plates regardless of material were of the same radius but varied in thickness. In total, the assembly measures just over one meter vertically, and under a meter horizontally.

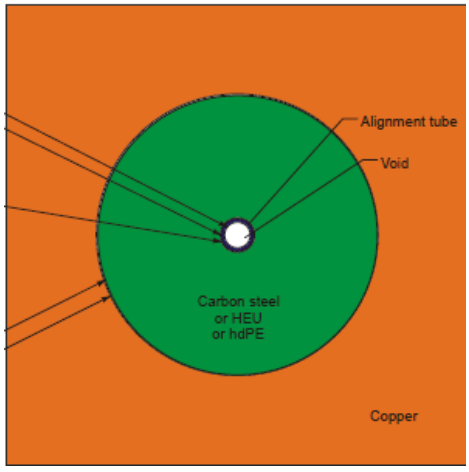

Figure 7– HEU-MET-FAST-072 Horizontal Cross Section (Figure from [16])

Materials used were HEU, carbon steel, high density polyethylene, copper, and steel and aluminums for support structuring. Impurities in the HEU and carbon steel were included in the first two configurations, having a significant impact, but deemed inconsequential in the final configuration. The various steels and aluminum have the same homogenized densities, with impurities across all configurations. The copper and polyethylene, when used, were homogenized and free of impurities.

3.2 HEU-MET-FAST-073: The Unmoderated ZEUS Experiment: A Cylindrical HEU Core Surrounded by a Copper Reflector [17]

This experiment, the final ZEUS experiment performed at LANL, exhibited sensitivities to copper. The evaluation contains one configuration. The general geometry of the assembly consists of a central HEU core surrounded by copper reflectors. As shown in the enhanced Figure 9, there are multiple distinct copper reflectors. This was done as each reflector has marginally different densities; yellow, orange, pink, and purple all represent copper reflector, while light and dark green represent varying densities of HEU, and blue the structural material.

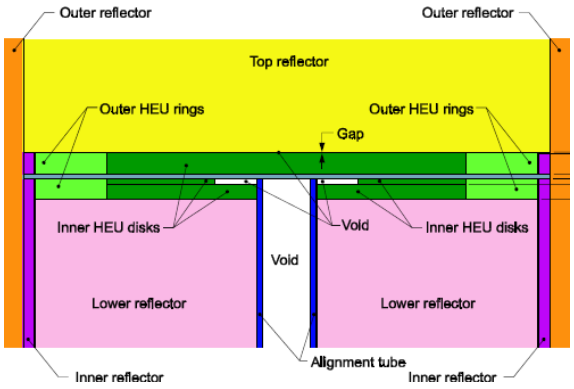

Figure 8– HEU-MET-FAST-073 Enhanced Vertical Cross Section (Figure from [17])

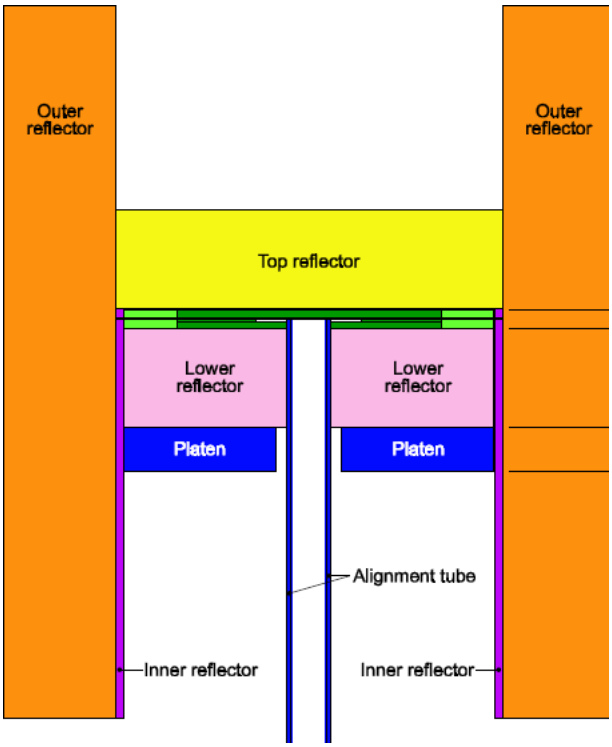

Figure 9– HEU-MET-FAST-073 Vertical Cross Section (Figure from [17])

The full vertical cross section of the core is shown in Figure 10. Fuel is constructed with varying rings and disks rather than full plates. The horizontal cross section is largely the same as Figure 8, adjusted for rings and disks rather than just disks of fuel. HEU and copper were free of impurities and divided into heterogenous regions with separate densities. Aluminum and steel contained impurities.

3.3 HEU-MET-FAST-084: HEU Metal Cylinders with Mild Steel, Copper, and Aluminum Oxide Reflectors [18]

These incredibly basic configurations of an HEU core with varying reflectors were performed at LANL in the late 1950s to determine the critical mass of Oralloy with different reflectors. The evaluation contains 27 configurations, of which 8 were included

for their sensitivity to copper, iron, and/or oxygen. Configurations were constructed in a fashion as shown in Figure 11. Critical masses were calculated by varying the core height, which was formed by a number of stacked discs of HEU and keeping a constant thickness of reflector material around the core. Experiments were then repeated, using a decreased constant thickness of reflector material. Finally, two additional experiments were performed, using an initial layer of beryllium, with an additional coating of iron.

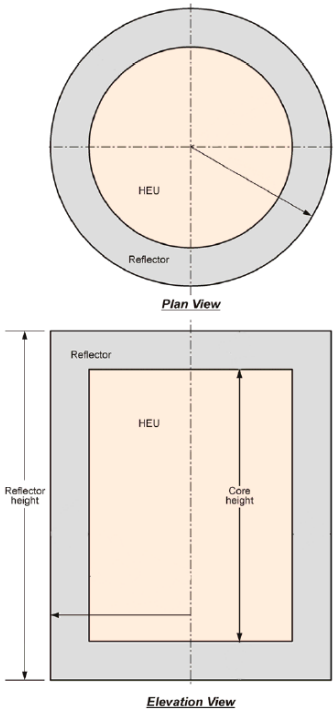

Figure 10– HEU-MET-FAST-084 Horizontal and Vertical Cross Sections (Figure from [18])

Reflectors tested include titanium, aluminium, graphite, mild steel, nickel, copper, cobalt, molybdenum, natural uranium, tungsten, beryllium, aluminium oxide, molybdenum carbide, and polyethylene. Of interest to this study are the two varying reflector thickness cases of aluminium oxide, copper, and mild steel: additionally, the two final configurations with beryllium and iron reflector. From a material basis, the HEU

used in all cases was identical and free from impurities. Reflector materials were also largely free from impurities, but occasionally included trace materials.

3.4 HEU-MET-FAST-085: Highly Enriched Uranium Metal Spheres Surrounded by Copper, Cast Iron, and Nickel-Copper-Zinc Alloy Reflectors [19]

Like the previous evaluation, these simple experiments were performed at LANL in the 1950's for the evaluation of Oralloy critical masses and reflector transport cross sections. Rather than concentric cylinders, these experiments were shaped in concentric spheres. The evaluation contains 6 configurations, of which 4 are sensitive to copper or iron. In a divergence from the previous evaluation, the density of HEU was not a constant, nor was the HEU or reflector materials radius. Additionally, as displayed in Figure 12, the fourth and sixth configurations contained a central cylindrical cavity for the placement of the neutron source.

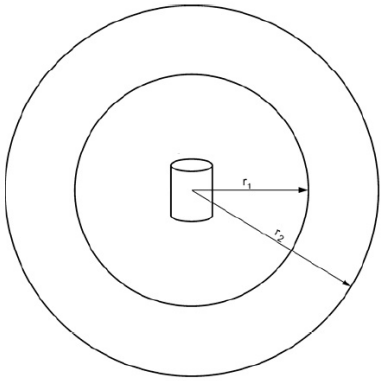

Figure 11– HEU-MET-FAST-085 Radial Cross Section (Figure from [19])

HEU isotopics were given without impurities, and for reflector materials as well. Additionally, elemental densities were optionally given in isotopic densities; this option was not modelled.

3.5 HEU-MET-INTER-006: The Initial Set of ZEUS Experiments: Intermediate-Spectrum Critical Assemblies with a Graphite-HEU Core Surrounded by a Copper Reflector [20]

This set of experiments make up the first ZEUS experiments performed at LANL, exhibiting sensitivities to copper. The evaluation contains four configurations, all of which are copper sensitive. The general geometry of the assembly consists of interspersed HEU and graphite plates. Figure 13 displays the first configuration. As observed in the figure, there is significantly more graphite than HEU. With each consecutive configuration, the ratio of graphite to HEU plates decreases, as does the number of units (HEU plate together with surrounding graphite plates). While the core compresses, the radial reflectors remain the same, and the top and bottom reflectors track the core compression. Horizontally, it remains the same basic layout as in other ZEUS experiments, as shown in Figure 8.

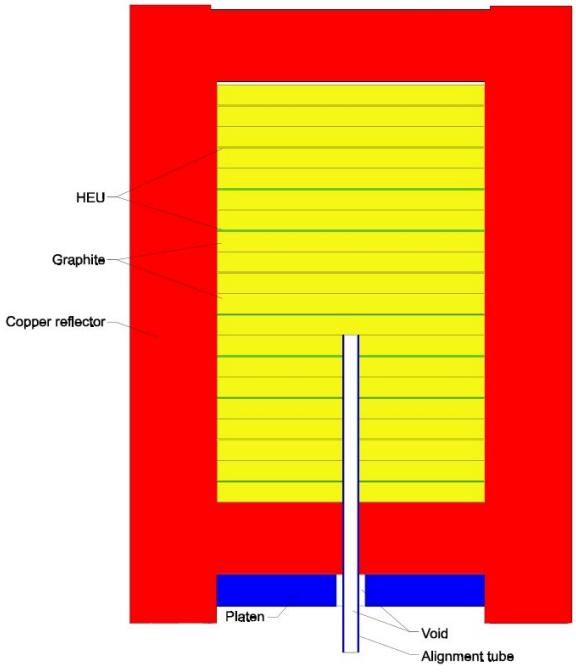

Figure 12– HEU-MET-INTER-006 Vertical Cross Section (Figure from [20])

HEU material compositions were homogenized and free of impurities, with changing densities across the configurations. Graphite plates were also homogenized and impurity free, with changing density across configurations. All copper reflectors were taken to be a singular homogenized impurity free density, across all configurations. The aluminium support structures had no variation across configurations but included several trace materials.

3.6 HEU-MET-THERM-013: Polyethylene Reflected and Moderated Highly Enriched Uranium Systems with Iron [21]

This evaluation consists of repeating slabs of polyethylene, iron, and HEU. The evaluation contains 2 configurations, where the thickness of the inserted iron slabs was varied, and number of unit layers increased. Both configurations exhibit a sensitivity to iron. An enhanced view of the unit layout can be seen in Figure 14.

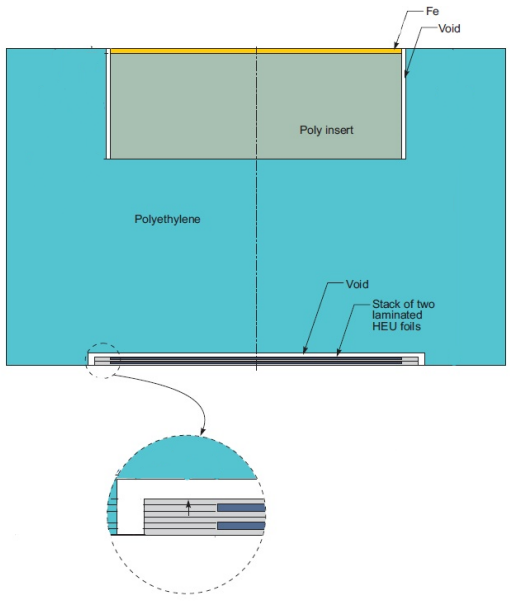

Figure 13– HEU-MET-THERM-013 Enhanced Vertical Cross Section (Figure from [21])

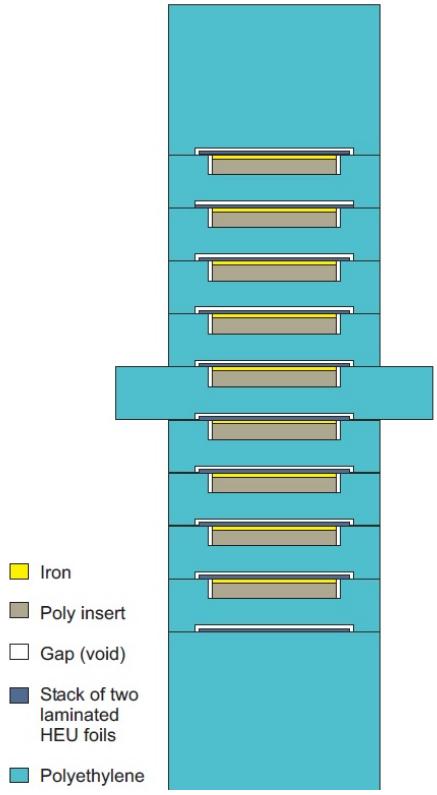

Figure 14– HEU-MET-THERM-013 Vertical Cross Section (Figure from [21])

The structure consists of cuboid polyethylene blocks with iron, laminated HEU, and polyethylene inserts and can be viewed above in Figure 15. HEU foils were laminated with thin layers of polyethylene and inserted into a gap in the polyethylene block. Additionally, separate polyethylene inserts were added to a larger gap in the block and capped with an iron plate. Horizontally, all components are square with various square cut-outs. The models presented here represent the simplified version of the benchmark evaluation; the detailed configurations have a more comprehensive process for the arrangement of the foils and blocks. For the simplified models, the densities for all inserts and layers were homogenized with no impurities. In detailed configurations, each individual insert block and HEU foil and lamination had unique values for the densities and thicknesses. Detailed configurations contained no impurities.

3.7 HEU-MET-THERM-015: 2 x 2 Array of Highly Enriched Uranium with Iron, Moderated and Reflected by Polyethylene [22]

Similar to the previous evaluation, this experiment consists largely of polyethylene blocks and iron, laminated HEU, and polyethylene inserts. This evaluation consists of one configuration, sensitive to iron. The full layout is effectively the same, with a taller central broad section, and an altered unit definition. The revised unit is shown in Figure 16.

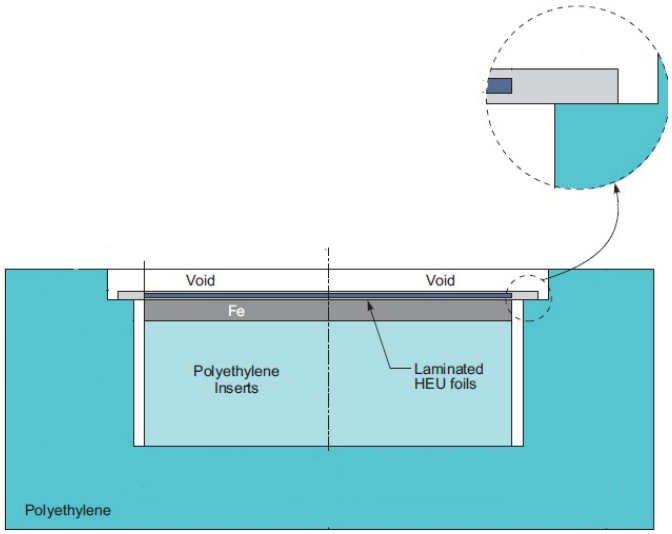

Figure 15– HEU-MET-THERM-015 Revised Unit Definition (Figure from [22])

Like the previous evaluation, there is both a simplified model and detailed model. More information on the detailed configuration can be found in the ICSBEP evaluation, but as before, materials for the simplified model were taken as the average density for all components. Impurities are ignored.

3.8 HEU-SOL-THERM-014: Uranium Nitrate Solution (70 gU/l) With Gadolinium [23]

Performed at the Solution Physical Facility of the Institute of Physics and Power Engineering in Russia, this evaluation was part of a series of water reflected HEU solution experiments. In total, six separate evaluations were produced from the series of experiments, all six of which were incorporated into this work. This evaluation, the first of the six evaluations, consists of three configurations, all three of which exhibit sensitivity to oxygen. The configuration governing all configurations in all six evaluations is presented in Figure 17. All configurations consist of a central stainless-steel cylinder filled with a uranium nitrate solution, arranged at a certain water level inside an outer steel cylinder filled with water. In this evaluation, configurations vary the volume of solution and water while maintaining the physical positions of the cylinders.

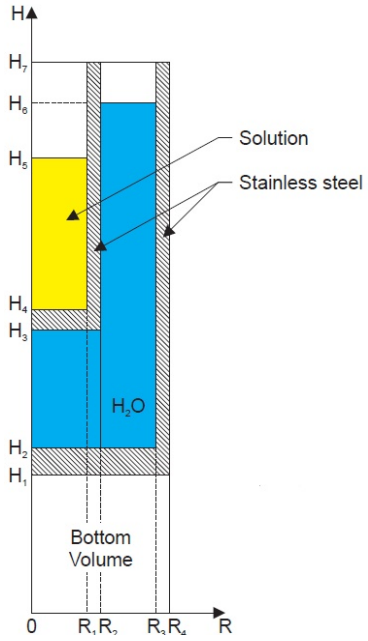

Figure 16– HEU-SOL-THERM-014 Through HEU-SOL-THERM-019 Vertical Cross Sections (Figure from [23])

In each configuration, unique fuel solution concentrations and thus number densities are used. Additionally, as the volume of the fuel solution and water increase with configurations, gadolinium is introduced into the fuel solution in minute concentrations due to gadoliniums extremely strong thermal absorption. The first configuration has none, which is increased with configuration. Water and steel number densities are a constant across configurations as well.

3.9 HEU-SOL-THERM-015: Uranium Nitrate Solution (100 gU/l) With Gadolinium [24]

The overall set up of this evaluation is based on the previous evaluation HEU-SOL-THERM-014, with several distinct differences. Mainly, the concentration of uranium in the fuel solution is slightly higher. This evaluation contains five configurations, which all exhibit sensitivity to oxygen. Whereas the configurations in the first evaluation consisted of a stationary fuel cylinder, the five configurations in this evaluation vary the position of the inner cylinder, in addition to varying the levels of fuel solution and water. Finally, in the fifth configuration, rather than void in the Bottom Volume of Figure 17, the configuration rests on an additional volume of water.

Material compositions vary by configuration but remain constant between cases when the fuel solution cylinder is fixed. The first two configurations have no gadolinium, but the next two have a set concentration added, and the final configuration adds further gadolinium. Water and structural materials remain the same.

3.10 HEU-SOL-THERM-016: Uranium Nitrate Solution (150 gU/l) With Gadolinium [25]

The overall set up of this evaluation is based on the previous evaluation HEU-SOL-THERM-014, with several distinct differences. Mainly, the concentration of uranium in the fuel solution is higher. This evaluation contains three configurations, which all exhibit a sensitivity to oxygen. Whereas the configurations in the first evaluation consisted of a stationary fuel cylinder, the three configurations in this evaluation vary the height of the inner cylinder, in addition to varying the levels of fuel solution and water. Finally, in the third configuration, rather than void in the Bottom Volume in Figure 17, the configuration rests on an additional volume of water.

Material compositions vary by configuration. The first configuration has no gadolinium, but the next two add gadolinium. Water and structural materials remain the same.

3.11 HEU-SOL-THERM-017: Uranium Nitrate Solution (200 gU/l) With Gadolinium [26]

The overall set up of this evaluation is based on the previous evaluation HEU-SOL-THERM-014, with several distinct differences. Mainly, the concentration of uranium in the fuel solution is higher. This evaluation contains eight configurations, which all exhibit a sensitivity to oxygen. Additionally, two of the configurations display a high enough iron sensitivity to meet the selection requirements. Whereas the configurations in the first evaluation consisted of a stationary fuel cylinder, the three configurations in this evaluation vary the height of the inner cylinder. Across the eight configurations, there are 3 set heights

that the assembly operates at. There are also two different cylinder radii that the fuel solution is held in across the eight cases. Fuel solution and water level heights vary as well. Finally, in the last three configurations, rather than void in the Bottom Volume in Figure 17, the configuration rests on an additional volume of water.

Material compositions vary by configuration when the height of the fuel solution cylinder varies. The first three configurations have no gadolinium, but the remainder add gadolinium in three increments. Water and structural materials remain the same.

3.12 HEU-SOL-THERM-018: Uranium Nitrate Solution (300 gU/l) With Gadolinium [27]

The overall set up of this evaluation is based on the previous evaluation HEU-SOL-THERM-014, with several distinct differences. Mainly, the concentration of uranium in the fuel solution is higher. This evaluation contains 12 configurations, which all exhibit a sensitivity to oxygen. Additionally, four configurations meet the sensitivity selection criteria for iron. Whereas the configurations in the first evaluation consisted of a stationary fuel cylinder, the 12 configurations in this evaluation vary the height of the inner cylinder, in addition to varying the levels of fuel solution and water. Across the 12 configurations, there are four fuel solution cylinder heights. There are two fuel cylinder radii that are used across the 12 configurations. In the final seven configurations apart from the seventh, rather than void in the Bottom Volume in Figure 17, the configuration rests on an additional volume of water.

Material compositions vary by configuration when the height of the fuel solution cylinder varies. The first three configurations have no gadolinium, but the remainder have

four varying levels of gadolinium concentration. Water and structural materials remain the same.

3.13 HEU-SOL-THERM-019: Uranium Nitrate Solution (400 gU/l) With Gadolinium [28]

The overall set up of this evaluation is based on the previous evaluation HEU-SOL-THERM-014, with several distinct differences. Mainly, the concentration of uranium in the fuel solution is higher. This evaluation contains three configurations, which all exhibit a sensitivity to oxygen. Whereas the configurations in the first evaluation consisted of a stationary fuel cylinder, the three configurations in this evaluation vary the height of the inner cylinder, in addition to varying the levels of fuel solution and water. The Bottom Volume in all cases consists of void.

Material compositions vary by configuration. The first configuration has no gadolinium, but the remainder have gadolinium. Water and structural materials remain the same across configurations.

3.14 IEU-MET-FAST-020: The FR0 Series 1: Copper-Reflected "Cylindrical" Uranium (20 % U-235) Metal [29]

As part of the Swedish zero power facility FR0, several tests were performed with the uranium cores coated with copper reflector. The evaluation contains a total of nine configurations. The selected experiments included in this evaluation contain sensitivities to copper in all nine configurations, and iron sensitivities in four. The general layout of the evaluation is presented in Figure 18 Figure 19 and Figure 20. As is typical for reactor

physics experiments, different configurations used a varying number of fuel assemblies and reflector materials, so the images presented can be significantly different than the actual configuration for several cases. In addition to variable assemblies, their positions were consistently shifted.

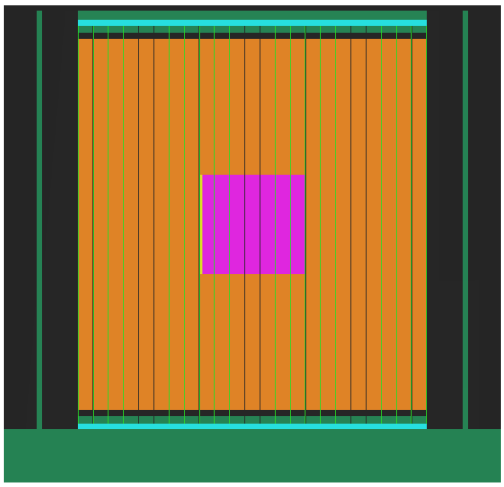

Figure 17– IEU-MET-FAST-020 Vertical Cross Section (Figure from [29])

The reactor assembly measures over a meter wide and high. For operation, the entire assembly is split in two horizontal halves on movable locking rails. To approach criticality, the halves are slid together. Locking rails are modeled as the top layer of dark green in Figure 18. The layers of dark green within the light blue layers are stainless steel inside end blocks of the elements; the outer light blue layers are the diluted steel outside end blocks. The remaining green below the lower outer end blocks, and on the periphery of the model, represents the facility to account for the room return of neutrons. From the vertical cross section, the IEU core is represented in pink. Further details on the fuel and copper arrangement are touched on later. Figure 19 displays the horizontal layout of the

full assembly; as noted, operation is performed by closing the two halves together, as is shown in the figure. The pink core is radially centered and surrounded by copper reflectors.

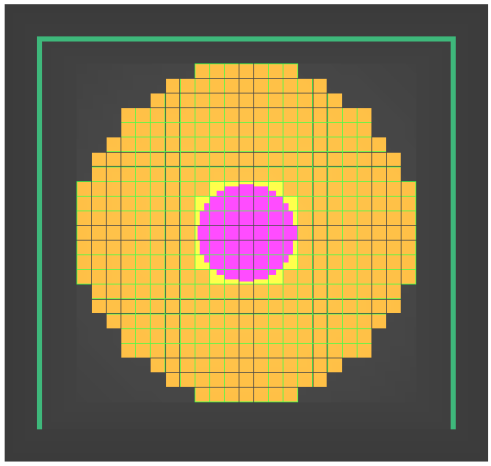

Figure 18– IEU-MET-FAST-020 Horizontal Cross Section (Figure from [29])

Yellow areas represent copper plate reflector blocks, which share space with the uneven peripheral fuel loading. Further detail is shown in Figure 20. Orange areas represent the remainder of the copper reflector blocks, which are entirely composed of copper. The grid spacing here is magnified above for visual purposes, and not to scale.

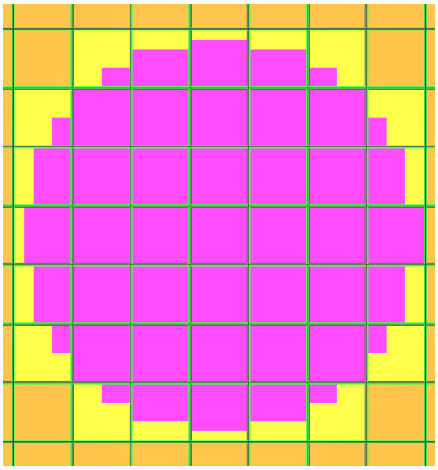

Figure 19– IEU-MET-FAST-020 Enhanced Horizontal Cross Section (Figure from [29])

Figure 20 being an enhanced cross section goes into further detail of the core arrangement, showing how periphery fuel elements were trimmed to form a more rounded core. Figure 21 details the fuel assemblies that comprise the overall evaluation. The elements were simplified to model square blocks. Fuel elements were simplified to a single material, except for the core periphery. This is a simplification as the elements were loaded with individual cells of Teflon and fuel or copper, rather than a pure block of fuel and copper. Regardless, fuel elements are represented by blocks of fuel and copper encased in a thin steel frame. Vertically each element is divided into multiple regions; the outer end blocks, inner end blocks, locking rails, and the fuel and copper regions. In copper reflector elements, the three axial zones of the fuel region all consist of copper. In fuel elements, the central axial zone is composed of fuel blocks, while the zones surrounding it consist of copper reflector. Variations by configuration are too detailed for inclusion in this summary; for further details consult the ICSBEP handbook.

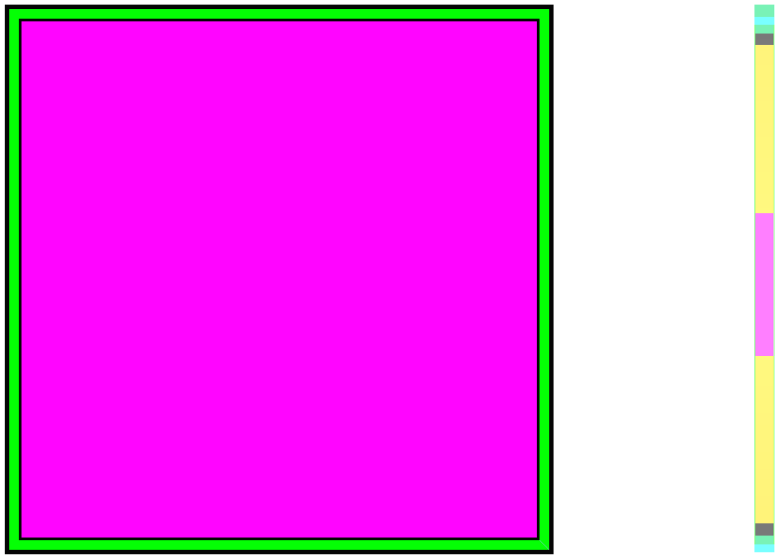

Figure 20– IEU-MET-FAST-020 Fuel Element (Figure from [29])

The evaluation is also referenced in the International Handbook of Evaluated Reactor Physics Benchmark Experiments as FR0-FUND-RESR-001. The fuel material is composed of IEU homogenized with its Teflon coating free of impurities. The partial assembly copper blocks have a different copper density than the full copper plates, but both remain homogenized throughout the reactor when required. The copper in both cases contains trace elements. The various end blocks and frames use a homogenized steel, with different densities between inner and outer blocks to account for different void fractions. The reactor core structure, support table, locking rails and room return are all modeled with homogenized pure iron.

3.15 IEU-MET-FAST-022: The FR0 Experiments with Diluted 20%-Enriched "Cylindrical" Uranium Metal Reflected by Copper [30]

As part of the same series of FR0 experiments as IEU-MET-FAST-020, the general configuration of the core remains largely the same, with many of the same variations. There are seven configurations in this evaluation; however, three of the configurations were determined to have an intermediate spectrum, and as a result, are referred to as IEU-MET-INTER-001. All seven configurations remain described in the IEU-MET-FAST-022 evaluation. All seven configurations are copper sensitive, with one configuration sensitive to iron, and two sensitive to oxygen. Rather than homogenizing the IEU and Teflon fuel, the core model remains heterogeneous, using graphite cells interspersed between fuel cells to form the assembly. A quarter cut away view of the model is shown in Figure 22. In the image, IEU fuel is purple and graphite is green. As opposed to the previous evaluation, the fuel assembly cell compositions vary substantially between configurations. Like the previous evaluation, the position of the fuel assemblies vary by configuration, as does the

axial location of the fuel and core. Graphite is not the only added heterogeneity across the configurations, as the assembly compositions change. Configurations include additional polyethylene, aluminium, nickel, heavy water, and iron oxide cells incorporated into the fuel elements. The exact specifications of such additions are described in further detail in the ICSBEP evaluation.

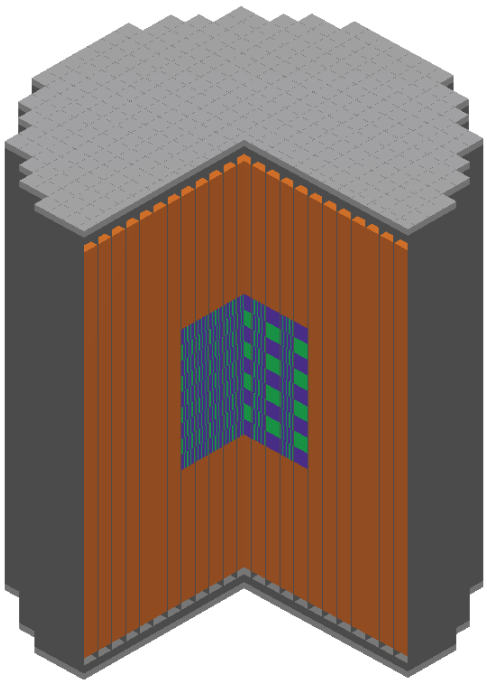

Figure 21– IEU-MET-FAST-022 Full Core (Figure from [30])

The evaluation is also referenced in the International Handbook of Evaluated Reactor Physics Benchmark Experiments as FR0-FUND-RESR-003. In all configurations, the IEU fuel is diluted with Teflon and homogenized without impurities. Again, partial copper plates and full copper blocks are homogenized with different densities for each, with trace materials. End blocks and structural materials use the same steel as the previous evaluation, with slightly different densities to account for different voiding. Additional fuel element cells were homogenized and without impurities.

3.16 IEU-MET-INTER-001: The FR0 Experiments with Diluted 20%-Enriched "Cylindrical" Uranium Metal Reflected by Copper [31]

See IEU-MET-FAST-022: The FR0 Experiments with Diluted 20%-Enriched "Cylindrical" Uranium Metal Reflected by Copper.

3.17 LEU-COMP-THERM-079: Water-Moderated U (4.31)O2 Fuel Rod Lattices Containing Rhodium Foils [32]

This evaluation contains 10 configurations, all of which are sensitive to oxygen. The assembly consists of LEU rods in an array submerged in water, with varying amounts of rhodium foils, varied rod positionings, and varied number of rods. As shown in Figure 23, there are four major elements to the structure: the driver elements, the experiment elements, the source element, and the grid plates. Driver elements consist of a cylindrical rod of LEU, encased with zircaloy cladding and top and bottom plugs. Experiment fuel elements consist of dozens of LEU pellets stacked together, interspersed with a certain rhodium foil thickness which varies by configuration. These pellets are also wrapped in zircaloy and capped with top and bottom plugs. The source element contains the source, which is held by a cylindrical aluminium holder. The holder is in the middle of two same length cylindrical LEU rods and encased in cladding and plugs.

Driver, experiment, and source elements all have the same diameters, though the source element is slightly longer (note the extended bottom plug in the figure). The grid plates consist of aluminium, with the lower plate supporting the fuel elements and the upper plate positioned to maintain straight fuel rods. Two grid plates were used, with different pitches; the first five configurations were performed at a lower pitch with more fuel

elements, and the last five performed at a higher pitch with fewer. Each subset of configurations then followed the same pattern of increasing rhodium, with no fuel elements(hence no rhodium) present in the first configuration per subset, no foils present in the second of the five configurations, and three increasing thicknesses of foils being used through the final three of the subset.

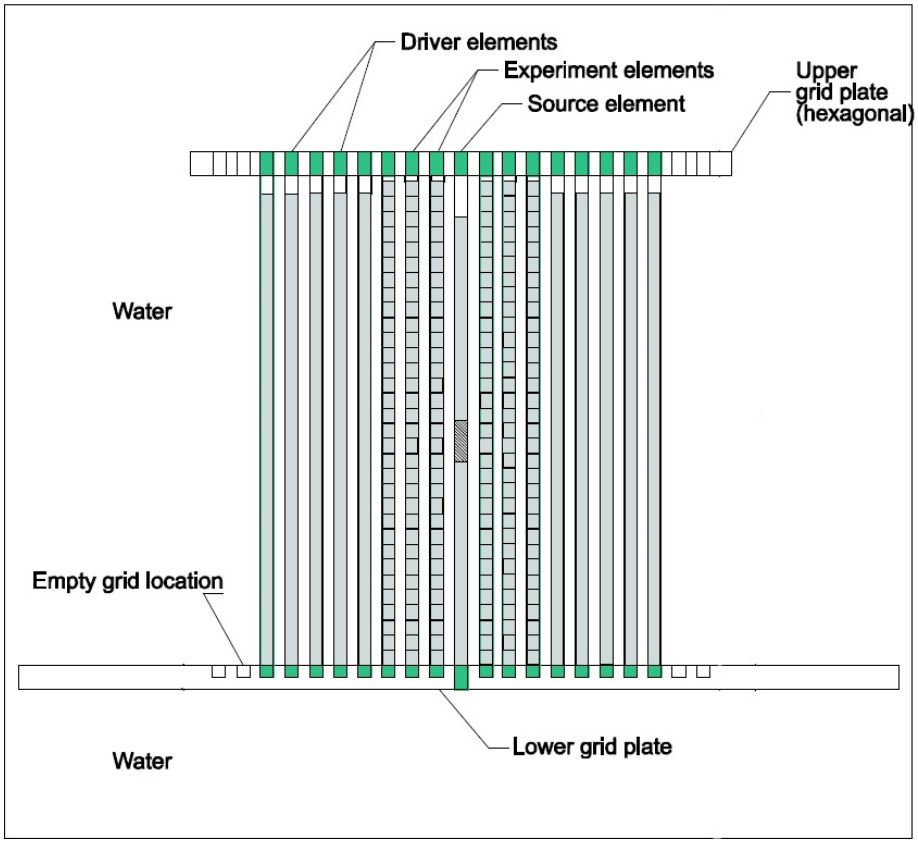

Figure 22– LEU-COMP-THERM-079 Vertical Cross Section (Figure from [32])

Figure 24 displays the fifth configuration, as it contains the highest number of fuel elements out of all configurations, as well as the experimental elements. Being the fifth case, this arrangement is using the lower pitch grid. With each configuration, experimental elements would be added to counter rhodium foils being added; being the fifth and final

configuration for this pitch, this represents the configuration with the thickest rhodium foils present.

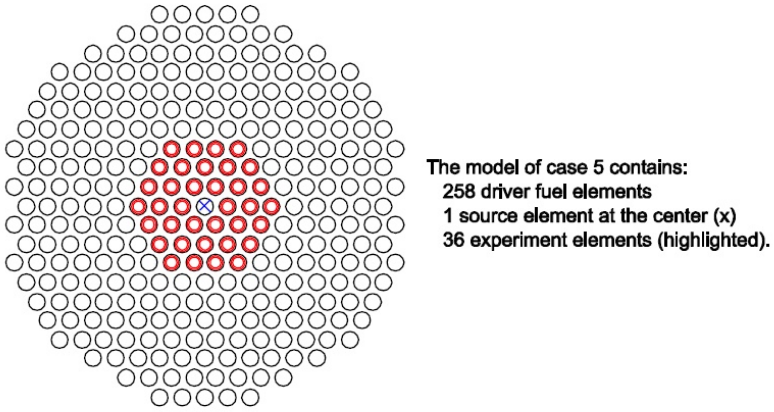

Figure 23– LEU-COMP-THERM-079 Radial Cross Section (Figure from [32])

The LEU fuel was UO_2, with no impurities and homogenized across all rods and pellets in every element. Zircaloy was taken as the given composition for the class of cladding it was, and free of impurities. Two of the rhodium foil thicknesses were the same density, but the thickness used in the fifth and tenth configuration were unique; all foils were pure rhodium. The water the assembly was submerged in was free of impurities, as was the aluminum and steel structural materials.

3.18 PU-MET-FAST-013: Copper-Reflected Array of Plutonium Fuel Rods [33]

This evaluation consists of a single iron and copper sensitive configuration, an array of plutonium rods surrounded by copper reflector. However, major simplifications were adopted, converting the assembly into a series of cylindrical regions rather than fuel pins.

In total, the assembly is divided into 14 homogenized zones; these zones are found in Figure 25, but can be difficult to read.

Zone 1 represents the core, which consists of plutonium fuel rods and copper foils, located mid-height in Figure 25 and on the left side of the figure; the figure extends radially from the center of the assembly. Zone 2 comprises the inner copper radial reflector, to the right of the core. Zone 3 are the steel fuel rod ends above and below the core. Zones 4, 5, and 6 are copper layers of reflectors located above and below the outer steel rod ends. Zone 7 is additional copper reflector radially outward from Zone 4. Zones 8 and 9 are the same as Zone 7, though radially outward from Zones 5 and 6, and the upper steel cap. Zone 10 is the central channel, a stainless-steel tube. Zone 11 represents the outermost rings of solid copper. Zones 12, 13, and 14 are a variety of structural materials made of stainless-steel and German-silver (a copper nickel alloy).

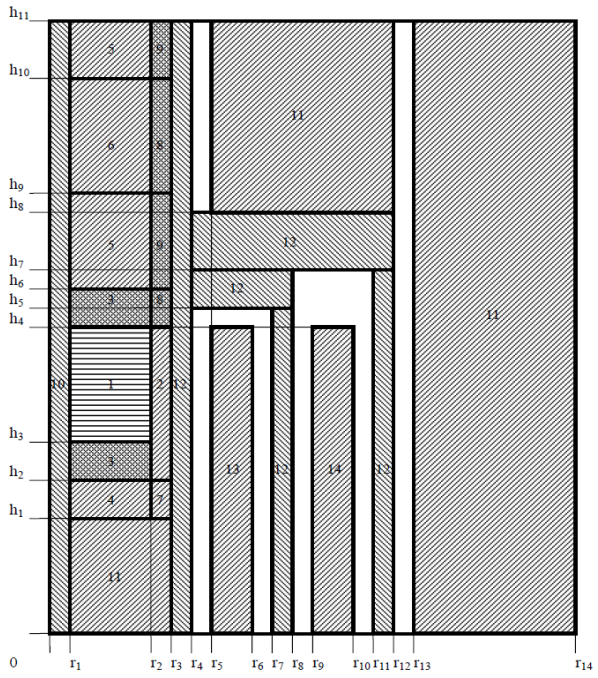

Figure 24– PU-MET-FAST-013 Axial Cross Section (Figure from [33])

Each Zone represents an independent density of a homogenized region of the assembly. Zone 1 is a mixture of plutonium and copper, with impurities from both materials included. Zones 2, 4, 5, 6, 7, and 11 are all pure copper free from impurities. Zones 3, 8, and 9 are a mixture of steel and copper, with impurities. Zones 10 and 12 are stainless steel. Zone 13 and 14 a pure mixture of copper and nickel.

3.19 PU-MET-FAST-014: Nickel-Reflected Array of Plutonium Fuel Rods [34]

As a part of the same series of experiments as PU-MET-FAST-013, the overall configuration remains largely the same. This evaluation also contains one configuration, which is sensitive to both copper and iron. The assembly is composed of homogenized zones, forming various cylinders and rings. This evaluation has an additional Zone, 15 in total. The most significant difference between evaluations is the use of nickel reflectors, as opposed to copper. Additionally, the periphery of the core is rearranged, as shown in Figure 26.

Zone 1 again represents the core, which has the same simplifications, but for a slightly larger number of fuel rods. Zone 2 comprises the inner nickel radial reflector, to the right of the core. Zone 3 are the steel fuel rod ends above and below the core. Zones 4, 5, and 6 are nickel layers of reflectors located above and below the outer steel rod ends. Zone 7 is additional nickel reflector radially outward from Zone 4. Zones 8 and 9 are the same as Zone 7, though radially outward from Zones 5 and 6, and the upper steel cap. Zone 10 is the central channel, a stainless-steel tube. Zone 11 represents the outer rings of solid nickel. Zones 12, 13, and 14 are a variety of structural materials made of stainless-steel and German-silver (a copper nickel alloy). Zone 15 is a separate outermost cylinder of nickel.

Each Zone represents an independent density of a homogenized region of the assembly. Zone 1 is a mixture of plutonium and copper, with impurities from both materials included. Zones 2, 4, 5, 6, 7, 11, and 15 are all pure nickel free from impurities. Zones 3, 8, and 9 are mixtures of steel and nickel, with impurities. Zones 10 and 12 are stainless steel with impurities. Zone 13 and 14 are German-silver alloys of copper and nickel.

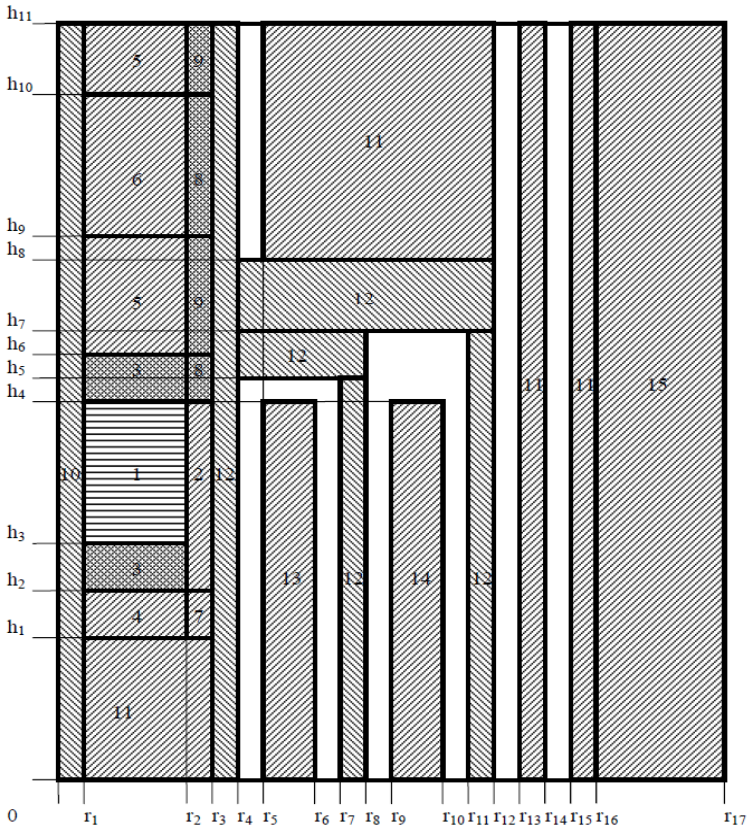

Figure 25– PU-MET-FAST-014 Axial Cross Section (Figure from [34])

3.20 PU-MET-FAST-040: Spherical Assembly of Pu-239 (δ, 98%) with a 1.6-cm Copper Reflector [35]

This evaluation consists of one configuration, which exhibits sensitivity to copper. The assembly is simplified to represent a series of layered plutonium spheres with a central source cavity. Figure 27 shows the un-simplified model, with various support structures included. To account for the slight changes in positioning and removal of support structures, the density and thicknesses of the shells are adjusted to keep mass constant. Surrounding the final layer of plutonium is a copper reflector. The benchmark model is therefore similar to the experimental configuration shown in the figure with the following simplifications: every layer is considered fully spherical, with no gaps or voids between layers or upper and lower assemblies; all support structures were removed, and the central cavity is left as void.

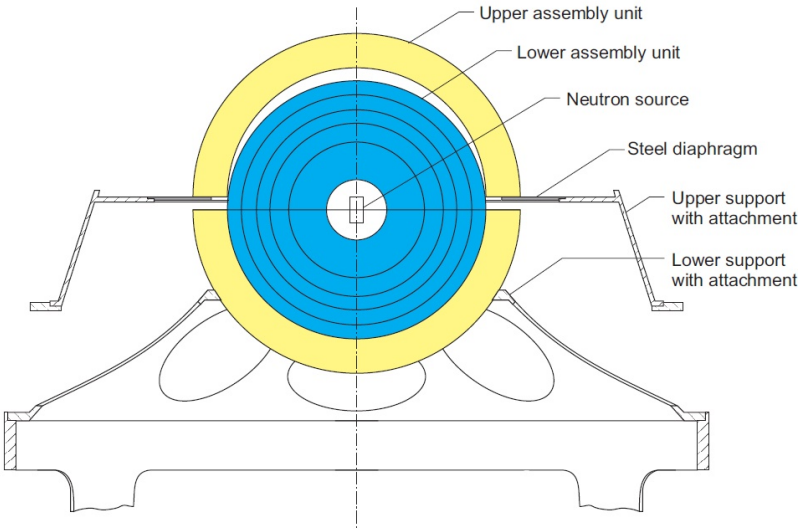

Figure 26– PU-MET-FAST-040 Vertical Cross Section (Figure from [35])

Each layer of plutonium has a unique density, homogenizing the plutonium and coating material, as well as impurities. The copper reflector has slight iron impurities included.

3.21 PU-SOL-THERM-034: Plutonium (8.3 wt.% Pu-240) Nitrate Solution with Gadolinium in Water-Reflected 24-Inch Diameter Cylinder [36]

This evaluation consists of 15 configurations, which all exhibit sensitivity to oxygen. The evaluation consists of a cylindrical tank of fissile solution, supported within a cylindrical tank of water reflector. Figure 28 shows the general geometry of all configurations. These components are fixed in space, with varying fissile solution heights and concentrations. The fissile solution consists of two plutonium concentrations mixed with nitric acid being used in the 15 configurations. Following the first configuration which contains no gadolinium, with each configuration, gadolinium is incrementally introduced into the solution, resulting in an increased height and volume of the fissile solution. After the first six configurations, the plutonium concentration is increased to offset the continued increase of gadolinium concentration, given the physical constraints of the solution cylinder height.

In the first six configurations, the plutonium and nitric acid concentrations remain the same, resulting in constant densities. Gadolinium densities increase with each configuration. The seventh through final configurations follow the same pattern, with constant plutonium and nitric acid densities, and increasing gadolinium densities. In all cases, the solution is free of impurities in plutonium, nitric acid, and gadolinium. The water

reflector uses a constant density though all configurations with no impurities. The stainless-steel tanks and support structures are constant and free of impurities.

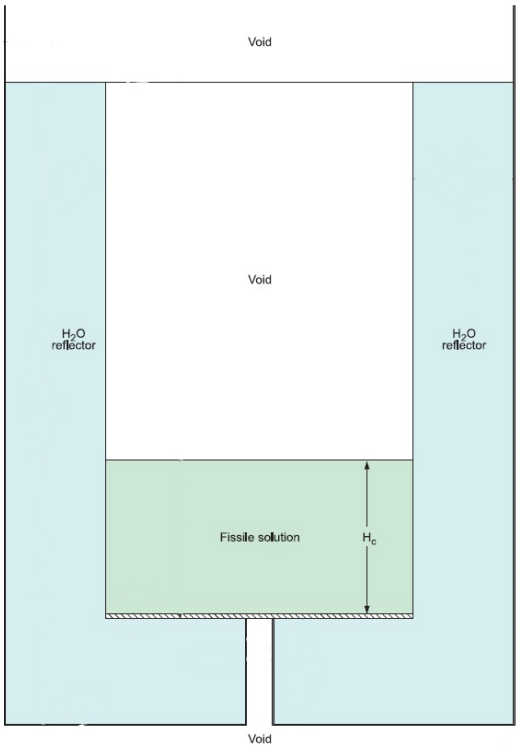

Figure 27– PU-SOL-THERM-034 Vertical Cross Section (Figure from [36])

3.22 SPEC-MET-FAST-014: Neptunium-237 Sphere Surrounded by Highly Enriched Uranium and Reflected by Low-Carbon Steel [37]

One of the few neptunium experiments incorporated into the ICSBEP handbook, this evaluation contains one configuration which displays a sensitivity to iron. Consisting of a central neptunium sphere, the sphere is then nested in a layer of tungsten and two layers of nickel. Encasing this sphere are two aluminium shells on the top and bottom, with stems at the center-points. This spherical configuration is further encased in hemispherical shells of HEU, from the top and bottom, with centered holes to account for the aluminium stems.

These shells, while nearly uniform, are unique and have slight differences in thickness, resulting in a slightly thicker lower half than top half. This sphere is further placed on top of a bottom hemisphere of reflector material. An aluminium spacer ring is then placed around the sphere, and on top of the bottom shell of reflector, and another reflector shell placed on top of the spacer. The detailed configuration is shown in Figure 29, which adds additional aluminium support plates, a mount tube, and an xy table for movement.

HEU hemispherical shells are impurity free with a homogenized density. The neptunium sphere itself contains impurities. The tungsten shield is free of impurities, as are the individual nickel shells which have unique compositions. The iron reflectors are free of impurities with separate densities for each hemisphere. The spacer and support plates have different densities, but free of impurities, as is the stainless steel xy table.

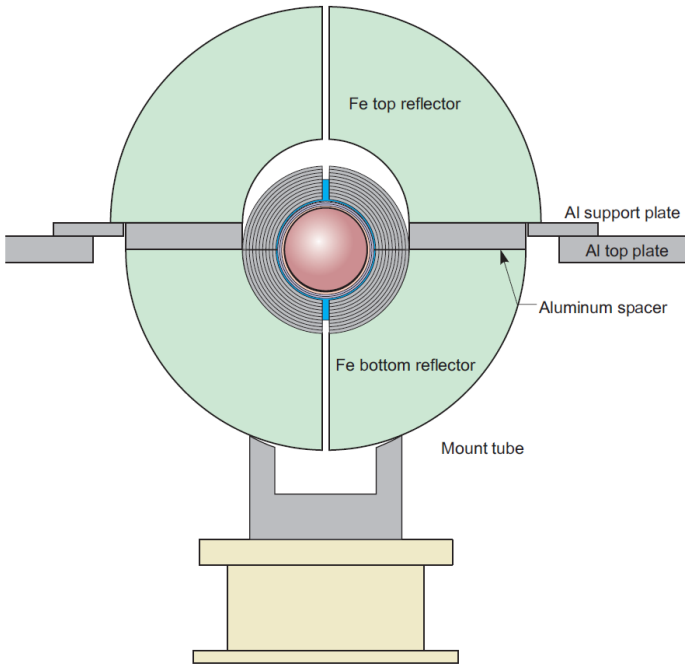

Figure 28– SPEC-MET-FAST-014 Vertical Cross Section (Figure from [37])

CHAPTER 4. RESULTS

Experimental criticalities (E) and uncertainties (δE), calculated sensitivities, calculated criticalities (C), and C/E values are tabulated in APPENDIX A, APPENDIX B, and APPENDIX C. The translation from criticalities to C/E values and the propagation of experimental and computational uncertainty are expressed in Equation 2, with a constant δC of 0.0001 Several methods of averaging C/E deviations were calculated to determine the performance of ENDF/B-VIII.0 cross sections across the selection of configurations.

$$C/E = \left(\frac{C}{E} - 1\right) * 1E5$$
$$\delta_{(C/E)} = \sqrt{\left(\frac{\delta C}{C}\right)^2 + \left(\frac{\delta E}{E}\right)^2} * 1E5 \quad (2)$$

Average Relative Deviations are calculated by first finding the absolute value of C/E values for each configuration, as uncertainty is expressed positively and negatively. The absolute C/E is divided by the corresponding configuration's experimental benchmark uncertainty, expressing C/E deviation in terms of experimental sigma. This averaging method is effective for determining the effect of cross section change relative to the various inaccuracies and simplifications in the experimental and evaluation process. Effectively, changes are weighted by the precision of the benchmark; a 500 pcm change in criticality in a configuration with 500 pcm uncertainty is less meaningful than the same criticality change in a configuration with 100 pcm uncertainty. Equation 3 demonstrates the calculation of this averaging method.

$$\text{Absolute Relative Deviation} = X_i = \frac{|\mathrm{C/E}|_\mathrm{i}}{\delta_{(\mathrm{C/E})_\mathrm{i}}}$$

$$\text{Average Absolute Relative Deviation} = \frac{1}{\mathrm{N}}\sum_{\mathrm{i}}^{\mathrm{N}} X_i \tag{3}$$

Mean Deviations are calculated by performing a straightforward average over the selected configurations. Equation 4 details the averaging and the propagation of C/E uncertainty. This method is effective in measuring the deviation from criticality, while also accounting for the cross-section changes. Whereas a change from 100 pcm to -100 pcm has the same absolute deviation from experimental criticality, therefore not accounted for in absolute averages, such a case has 200 pcm of variation from the ENDF/B-VIII.0 data. This type of change is only visible in this averaging method, and while not as effective at determining improved performance, it allows general trends in criticality changes to be noticed. As C/E uncertainty is effectively constant and dominated by experimental error, the uncertainty in the mean is constant for the same set of configurations across all library changes and substitutions. These average deviations also reflect the bias of the cross sections, being the mean deviation from critical.

$$Mean\ Deviation = \frac{1}{N}\sum_{i}^{N}(C/E)_i$$

$$\delta_M = \frac{1}{N}\sqrt{\sum_{i}^{N}{\delta_{(C/E)_i}}^2} \tag{4}$$

Absolute Mean Deviations are calculated by performing an average on the absolute deviations in a series of configurations. Equation 5 shows the calculation of the absolute mean of C/E values in the series and the error in the absolute mean. As C/E uncertainty is effectively constant and dominated by experimental error, the uncertainty in the absolute mean is constant for the same set of configurations across all library changes, and the same value as the uncertainty in the mean deviation. The absolute mean, like the relative deviation, evaluates the average departure from experimental values. This method is effective for determining the accuracy of cross sections by finding the change in absolute deviations, unweighted.

$$Absolute\ Mean\ Deviation = \frac{1}{N}\sum_{i}^{N}|C/E|_i$$

$$\delta_{AM} = \frac{1}{N}\sqrt{\sum_{i}^{N}\delta_{(C/E)_i}{}^2} \tag{5}$$

Root Mean Square Deviation is calculated by squaring C/E values; doing so effectively weights the absolute deviations by the magnitude of said deviation [38]. Squared values are summed, normalized by the population, and the square root taken to return to a measure of deviation. Equation 6 details the determination of the Root Mean Square, as well as the uncertainty. Propagation of Root Mean Square uncertainty is more detailed than previous calculations, as the square root adds a function which must be partially differentiated with respect to the various C/E values. Because of that, unlike previous averaging the propagated uncertainty must account for the C/E values in addition to the uncertainties. As

a result, uncertainties in the Root Mean Square are variable depending on the experimental uncertainty weighted C/E. This method is useful for determining the accuracy of cross sections by finding the change in absolute deviations, effectively weighting the deviation by the deviation's magnitude, and was recommended by Dr. Farzad Rahnema.

$$Root\ Mean\ Square\ Deviation = \sqrt{\frac{1}{N}\sum_{i}^{N}(\mathrm{C/E})_i^2}$$

$$\delta_{RMS} = \sqrt{\sum_{i=1}^{N}\left(\frac{(\mathrm{C/E})_i}{\sqrt{N}\sqrt{\sum_{i=1}^{N}(\mathrm{C/E})_i^2}}\right)^2 {\delta_{(C/E)_i}}^2} = \tag{6}$$

$$\sqrt{\frac{1}{N\sum_{i=1}^{N}(\mathrm{C/E})_i^2}}\sqrt{\sum_{i=1}^{N}(\mathrm{C/E})_i^2{\delta_{(C/E)_i}}^2}$$

Finally, non-absolute relative deviations were fit to a normal distribution and tested for normality to represent the statistical spread of the deviations between calculated and experimental data. All code calculated results met convergence criteria such that the distributions were sufficiently normal, and while the effective uncertainties in benchmarks are not necessarily normal in nature, they are derived as to represent normality. All in all, registering the change in magnitude of the average is the goal of this work, and every method of averaging introduces additional information on the performance of new cross sections. In cases where average absolute deviations decrease, such a decrease indicates an improvement in cross section accuracy in the sample of benchmarks selected.

4.1 Isotopic ENDF/B-VIII.0 C/E Assessments

4.1.1 Oxygen-16

The criticality results of isotope substitutions are located in C.1 Oxygen-16, as well as the calculated C/E values and uncertainties from data in A.1 Oxygen-16. These C/E values are plotted by identifier in Figure 30. C/E values are presented with the full ENDF/B-VII.1 library, the base ENDF/B-VII.1 library with ^{16}O ENDF/B-VIII.0 cross section substitution, and with the full ENDF/B-VIII.0 library. While determining variation as a result of ^{16}O ENDF/B-VIII.0 cross sections is the goal, displaying the total library update as well is informative for demonstrating how much of a contributing factor the new ^{16}O evaluation is. Experimental uncertainties from APPENDIX C are mapped to two sigma, representing the boundary of 95% agreement with benchmark experimental values. Whether there is 95% agreement is more easily confirmed by sight than 68%, or one sigma. With dozens of cases, 95% agreement is more likely to appear than 68%. It is notable the regression ENDF/B-VIII.0 data results in, with 75% of benchmarks in ENDF/B-VII.1 bounded by 2 sigma, as opposed to 63% of ENDF/B-VIII.0 substituted ^{16}O cross sections. Expressing deviation in terms of sigma results in an average deviation of 1.35 sigma for ENDF/B-VII.1 and 1.69 sigma for ENDF/B-VIII.0 ^{16}O substituted cross sections. An enhanced version of Figure 30 is displayed below in Figure 31; results where absolute deviations were greater than 2000 pcm were ignored for clarity of outcomes. With so many data points, and wide-ranging axes, it can be difficult to see the actual changes the substitution has resulted in. Therefore, Figure 32 goes into further detail by plotting the absolute changes instigated by the revisions. Foremost is the observation that in every configuration, the replacement resulted in a decrease in the C/E ratio.

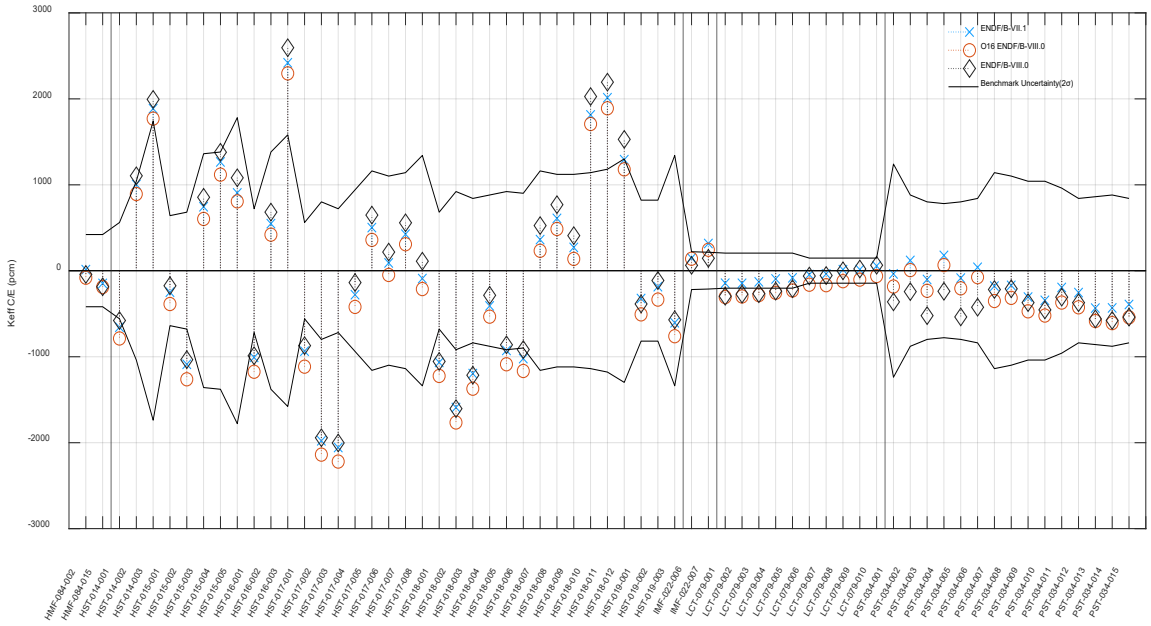

Figure 29– Oxygen-16 ENDF/B-VIII.0 C/E by Library

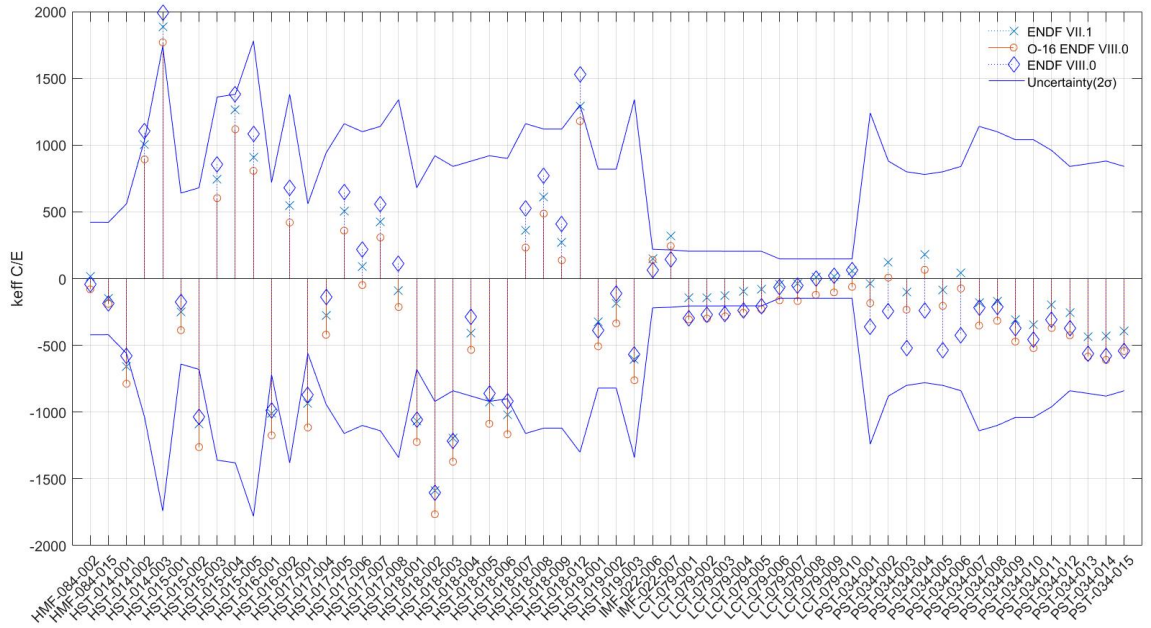

Figure 30– Oxygen-16 ENDF/B-VIII.0 C/E by Library; Vertically Constrained

Given the brief assessment and opinion noted earlier in Background and Relevance, discussing the changes made to the reactions of note between ENDF/B-VII.1 and ENDF/B-

VIII.0, this observation agrees with the opinion that the widespread and consistent reduction in the thermal and intermediate elastic scattering cross section would correspondingly reduce criticality. Changes with respect to sensitivity are shown in 4.2.1 Oxygen-16.

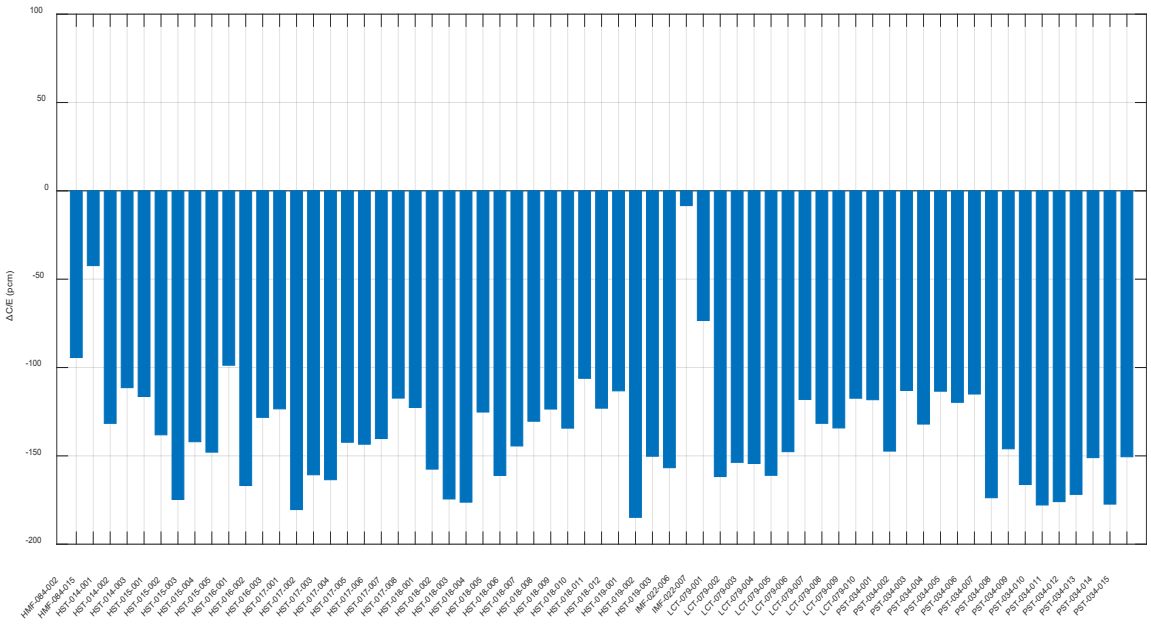

Figure 31– Oxygen-16 ENDF/B-VIII.0 Change in C/E

However, as has already been touched upon, such a decrease is not always for the better; Table 1 lists the various averages of the different libraries. The trend of an overall decrease is especially noted in the mean deviation, as the mean decreases 137.4 pcm. 16% of cases had a decrease of 1 sigma experimental uncertainty or greater, and no configurations had a decrease of 2 sigma or greater. Absolute measures of deviation, however, show an increasing deviation from criticality; in terms of experimental error, deviations increased 0.34 sigma; in absolute terms, experiment deviations increased an average of 61.3 pcm; and expressed as a root mean square, deviations increased 31.8 pcm.

Table 1– Oxygen-16 Isotopic Substitution Averages

Average:	ENDF/B-VII.1	O-16 ENDF/B-VIII.0	ENDF/B-VIII.0
Relative Deviation	1.35σ	1.69σ	1.56σ
Mean Deviation	-37.2±59.0	-174.6±59.0	-53.1±59.0
Absolute Mean Deviation	578.9±59.0	640.2±59.0	655.3±59.0
Root Mean Square Deviation	839.4±73.9	871.2±69.9	896.0±75.1

While the 63 cases here are only a small subset of the 3600 ^{16}O sensitive ICSBEP configurations, they still represent a diverse arrangement of evaluations, spanning 10 evaluations with varying enrichments, fissile materials, chemical forms, and spectrums.

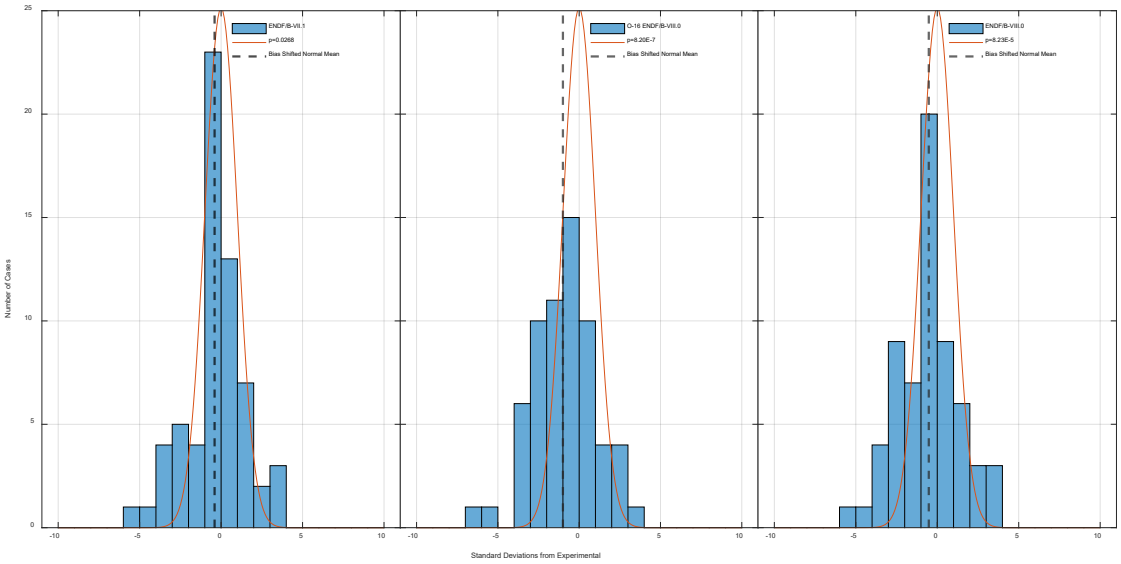

Figure 32– Effect of ENDF/B-VIII.0 Data on Normality; Oxygen-16 and Full Library

As seen in Figure 33, the introduction of the ENDF/B-VIII.0 ^{16}O cross section data results in a skewed distribution, with a resulting decrease in p-value. Whereas the ENDF/B-VII.1 library was bordering on a normal distribution, depending on standardized p-value restrictions, isotope substitution clearly does not pass the test for being the result of a normal distribution. However, while there is a p-value decrease, the potential for the

shape of a normal distribution is still possible; therefore, as tabulated in Table 2, the effect of the shift in the mean is accounted for. Effectively, at the given shift from normality value, the data distribution most matched a normal distribution, resulting in the maximum p-values. Accounting for the general shift from bias, the near shape of normality is nearly preserved, albeit at a biased distance from agreement with experimental data. This confirms the increased negative bias in the data; while the data itself may nearly be normally distributed, the bias causing this shift from agreement is visible, most matching a normal distribution 0.6 standard deviations lower than with ENDF/B-VII.1 data.

Table 2– P-values Accounting for Oxygen-16 Bias

	Maximum P-value	Shift from Normality
ENDF/B-VII.1	0.2299	-0.40σ
O16 ENDF/B-VIII.0	0.0346	-1.00σ
ENDF/B-VIII.0	0.0394	-0.52σ

Even accounting for this bias, the data is less normally distributed, no longer exceeding the generally accepted p-value of 0.05.

4.1.2 Iron-56

The results of isotope substitutions are located in C.2 Iron-56, as well as the calculated C/E values and uncertainties from data in A.2 Iron-56. These C/E values are plotted by identifier in Figure 34. C/E values are presented with the full ENDF/B-VII.1 library, the base ENDF/B-VII.1 library with ^{56}Fe ENDF/B-VIII.0 cross section substitution, and with the full ENDF/B-VIII.0 library. The ENDF/B-VIII.0 data results in a fairly trivial improvement, with 48% of benchmarks in ENDF/B-VII.1 bounded by 2 sigma, as opposed to 56% of ENDF/B-VIII.0 substituted ^{56}Fe cross sections. Expressing

deviation in terms of sigma results in an average deviation of 2.61 sigma for ENDF/B-VII.1 and 2.54 sigma for ENDF/B-VIII.0 ^{56}Fe substituted cross sections.

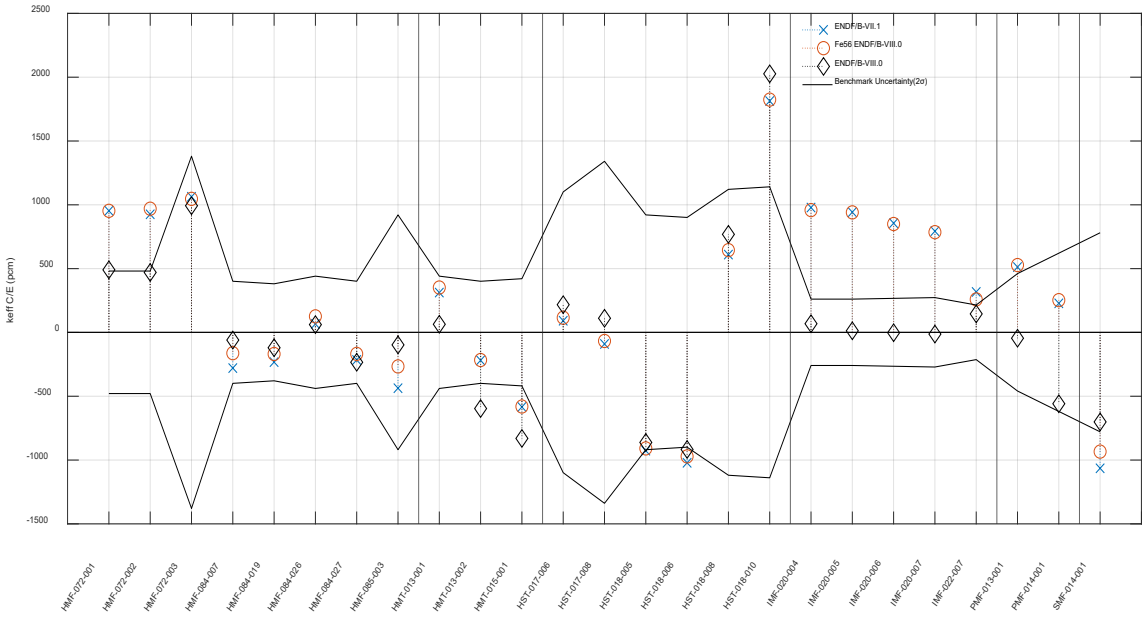

Figure 33– Iron-56 ENDF/B-VIII.0 C/E by Library

Figure 35 goes into further detail by plotting absolute changes between ENDF/B-VII.1 and ENDF/B-VIII.0 as a function of identifier. The primary observation that in many configurations, the replacement results in a change indistinguishable from computational effects. Given the opinion noted earlier in Background and Relevance, discussing the changes made to the reactions of note between ENDF/B-VII.1 and ENDF/B-VIII.0, there is little basis for conclusive changes. The minimal increase in elastic scattering was likely countered by the addition of the intermediate capture background, or changes were too marginal to produce meaningful results. Changes with respect to sensitivity are shown in 4.2.2 Iron-56.

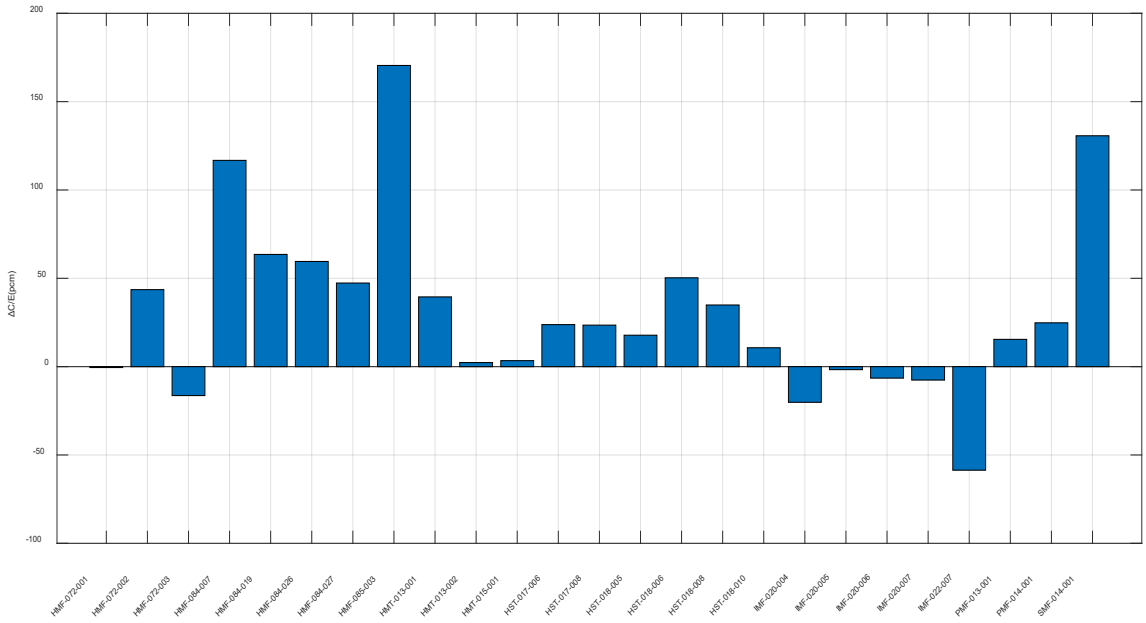

Figure 34– Iron-56 ENDF/B-VIII.0 Change in C/E

Table 3 lists the various averages of the different libraries. The overall mean deviation increases 30.7 pcm. Absolute measures of deviation, however, show a trivial decreasing departure from criticality; in terms of experimental error, deviations decreased 0.07 sigma; in absolute terms, experiment deviations decreased an average of 19.5 pcm; and expressed as a root mean square, deviations decreased 13.9 pcm. As a result of the statistical insignificance, no convincing improvement or regression of ^{56}Fe ENDF/B-VIII.0 evaluations can be concluded. No configurations had an increase or decrease of 1 sigma experimental uncertainty or greater.

Table 3– Iron-56 Isotopic Substitution Averages

Average:	ENDF/B-VII.1	Fe-56 ENDF/B-VIII.0	ENDF/B-VIII.0
Relative Deviation	2.61σ	2.54σ	1.21σ
Mean Deviation	215.8±72.5	246.5±72.5	15.6±72.5
Absolute Mean Deviation	621.4±72.5	601.9±72.5	418.6±72.5
Root Mean Square Deviation	750.8±84.9	736.9±85.1	624.7±101.6

While the 25 cases here are only a small subset of the 1200 ^{56}Fe sensitive ICSBEP configurations, they represent a diverse arrangement of evaluations, spanning 12 evaluations with varying enrichments, fissile materials, chemical forms, and spectrums.

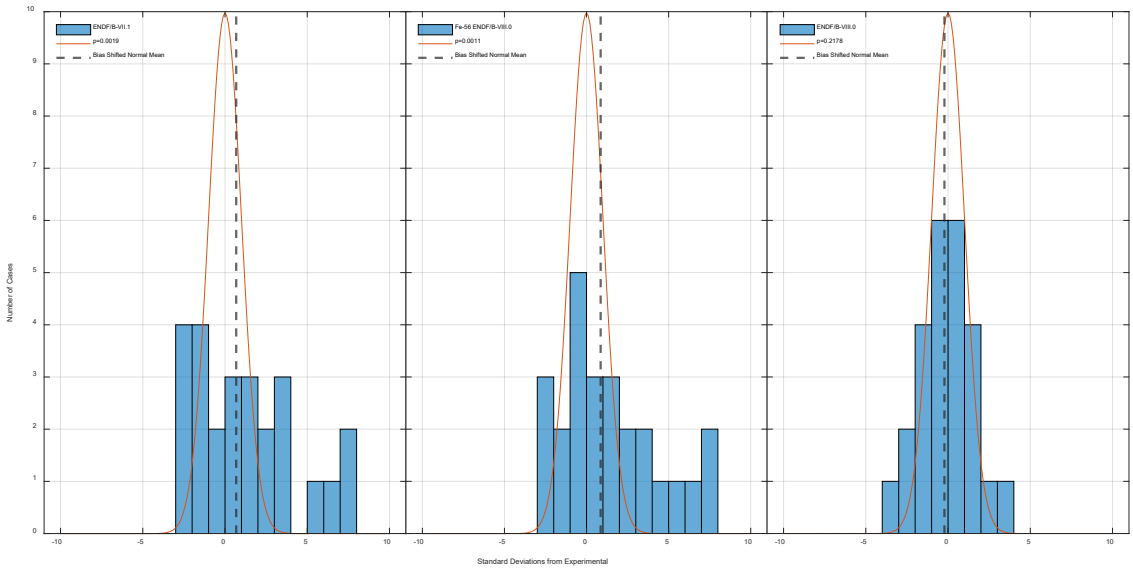

Figure 35– Effect of ENDF/B-VIII.0 Data on Normality; Iron-56 and Full Library

As seen in Figure 36, the introduction of the ENDF/B-VIII.0 ^{56}Fe cross section data results in a skewed distribution, with a resulting decrease in p-value. Whereas the ENDF/B-VII.1 library was not normal, isotope substitution does not improve the results as is to fit a normal distribution. Table 4 accounts for the effect of the shift in the mean or bias, showing that while the data is not normal as is, the general shape of normality improves, albeit at a biased distance from agreement with experimental data. This confirms the increased bias in the data; while the data itself may nearly be normally distributed, the bias causing this shift from agreement is visible, most matching a normal distribution 0.18 standard deviations higher than with ENDF/B-VII.1 data.

Table 4– P-values Accounting for Iron-56 Bias

	Maximum P-value	Shift from Normality
ENDF/B-VII.1	0.0129	0.68σ
Fe56 ENDF/B-VIII.0	0.0274	0.86σ
ENDF/B-VIII.0	0.3330	-0.22σ

Accounting for this bias, the data is more normally distributed, agreeing with the general trend of negligible improvement noted in earlier analysis. This is driven by changes occurring in the peripheral negative instances, where the upward increase in criticality shifts the full distribution positively biased, even as doing so shows improvement in those peripheral values themselves.

4.1.3 Copper-63

The results of isotope substitutions are located in C.3 Copper-63, as well as the calculated C/E values and uncertainties from data in A.3 Copper-63. These C/E values are plotted by identifier in Figure 37. C/E values are presented with the full ENDF/B-VII.1 library, the base ENDF/B-VII.1 library with ^{63}Cu ENDF/B-VIII.0 cross section substitution, and with the full ENDF/B-VIII.0 library. Improvement from ^{63}Cu ENDF/B-VIII.0 data resulted in significant agreement with experimental data, with 41% of benchmarks in ENDF/B-VII.1 bounded by 2 sigma, as opposed to 69% of ENDF/B-VIII.0 substituted ^{63}Cu cross sections. Expressing deviation in terms of sigma resulted in an average deviation of 3.48 sigma for ENDF/B-VII.1 and 1.97 sigma for ENDF/B-VIII.0 ^{63}Cu substituted cross sections.

Figure 38 goes into further detail by plotting absolute changes as a result of cross section adjustments.

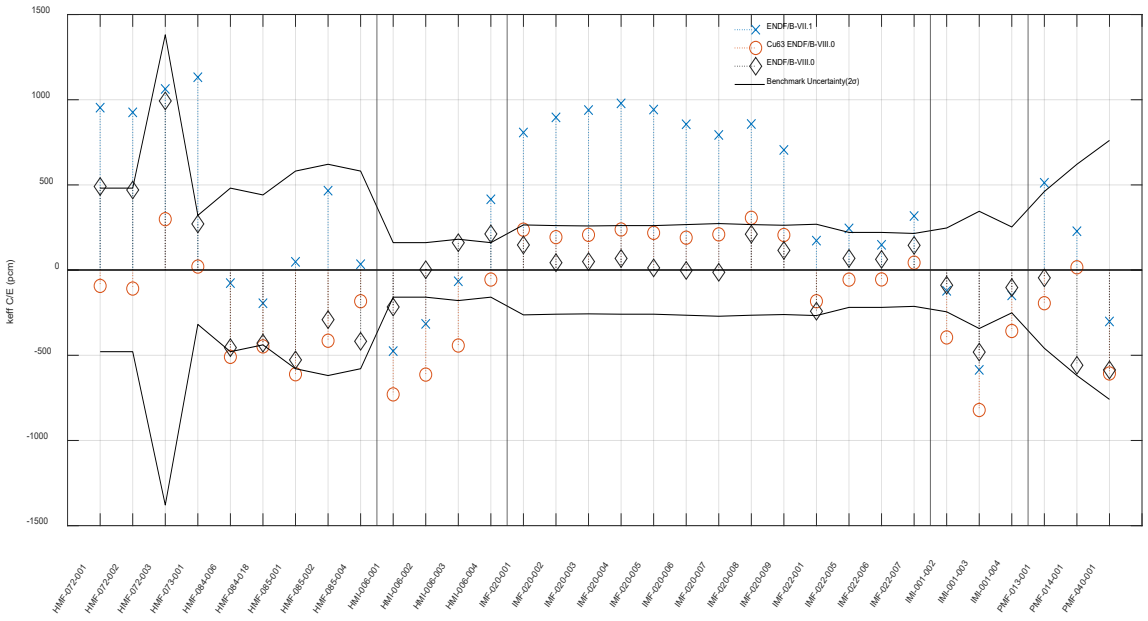

Figure 36– Copper-63 ENDF/B-VIII.0 C/E by Library

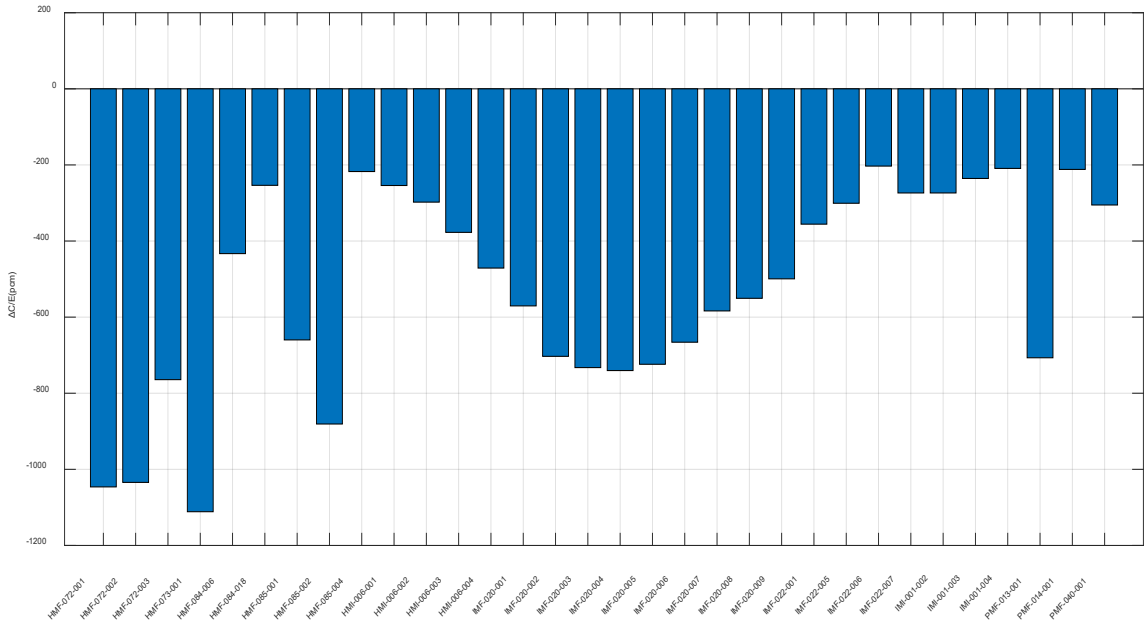

Figure 37– Copper-63 ENDF/B-VIII.0 Change in C/E

The primary observation is that in every configuration, the replacement results in a significant reduction in criticality. These changes are extremely large, with a minimum decrease of 200 pcm, and some cases resulting in a full percentage reduction in criticality.

Given the opinion noted earlier in Background and Relevance, discussing the changes made to the reactions of note between ENDF/B-VII.1 and ENDF/B-VIII.0, the assessment of a reduced criticality is particularly accurate as a result of significant reductions in fast and intermediate elastic scattering cross sections. Changes with respect to sensitivity are shown in 4.2.3 Copper-63.

Table 5 lists the various averages of the different libraries. The overall mean deviation decreases 520.2 pcm. 91% of cases had a decrease of 1 sigma experimental uncertainty or greater, 72% of configurations had a decrease of 2 sigma or greater, with 53% of configurations having a decrease of 3 sigma or greater. Absolute measures of deviation show a significant reduction; in terms of experimental error, deviations decreased 1.51 sigma; in absolute terms, experiment deviations decreased an average of 233.1 pcm; and expressed as a root mean square, deviations decreased 271.7 pcm. This consistent decrease, in contrast to ^{16}O's consistent decrease, resulted in sizeable improvements.

Table 5– Copper-63 Isotopic Substitution Averages

Average:	ENDF/B-VII.1	Cu-63 ENDF/B-VIII.0	ENDF/B-VIII.0
Relative Deviation	3.48σ	1.97σ	1.24σ
Mean Deviation	379.9±39.3	-140.3±39.3	-29.1±39.3
Absolute Mean Deviation	522.6±39.3	289.5±39.3	249.4±39.3
Root Mean Square Deviation	630.5±46.0	358.8±40.4	337.8±74.8

The 32 cases presented are a near complete subset of the 39 $^{63,65}Cu$ sensitive ICSBEP configurations at fast and intermediate spectrums, and 76 $^{63,65}Cu$ sensitive configurations in general. As seen in Figure 39, the introduction of the ENDF/B-VIII.0 ^{63}Cu cross section data results in much improved agreement with a normal distribution, although not nearly normal.

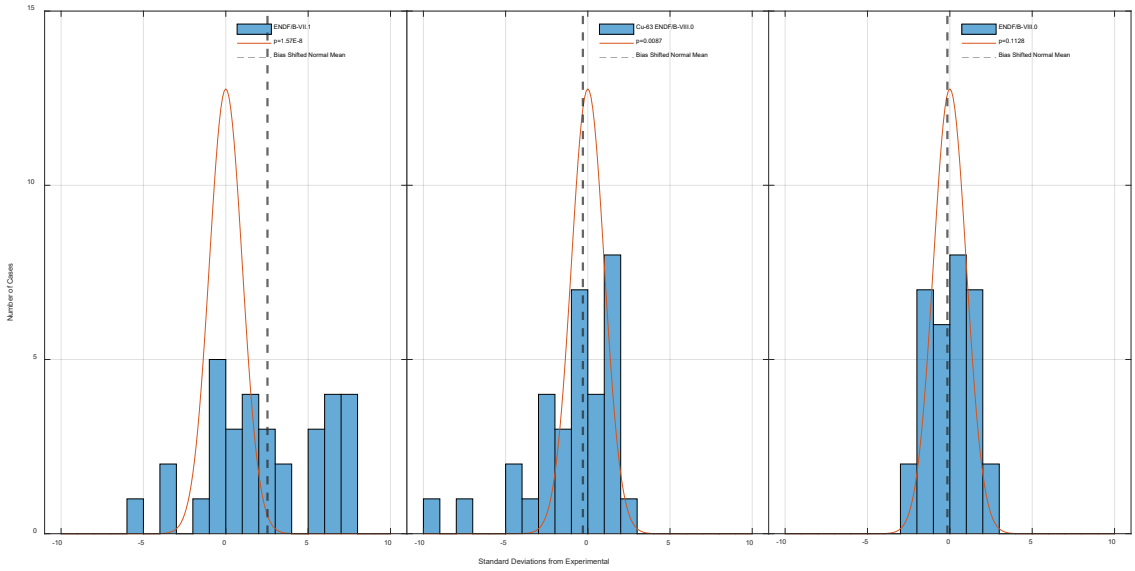

Figure 38– Effect of ENDF/B-VIII.0 Data on Normality; Copper-63 and Full Library

However, the improvements relative to ENDF/B-VII.1 are significant representing the considerable improvement noted before. Table 4 accounts for the effect of the shift in the mean or bias, showing that while the data is not yet normal, the general shape of normality improves, albeit at a biased distance from agreement with experimental data. This confirms the decreased bias in the data; while the data itself may nearly be normally distributed, the bias causing this shift from agreement is visible, most matching a normal distribution 2.83 standard deviations lower than with ENDF/B-VII.1 data.

Table 6– P-values Accounting for Copper-63 Bias

	Maximum P-value	Shift from Normality
ENDF/B-VII.1	8.3937E-4	2.53σ
Cu63 ENDF/B-VIII.0	0.0417	-0.30σ
ENDF/B-VIII.0	0.2016	-0.15σ

Accounting for this bias, the data is more normally distributed, agreeing with the general trend of improvement noted in earlier analysis. This is driven by changes occurring

in the peripheral positive instances and countered by greater negative peripherals, where the decrease in criticality shifts the full distribution. Overall, both result in general improvement in terms of testing for normality and the bias they hold.

4.1.4 Copper-65

The results of isotope substitutions are located in C.4 Copper-65, as well as the calculated C/E values and uncertainties from data in A.3 Copper-65. These C/E values are plotted by identifier in Figure 40. C/E values are presented with the full ENDF/B-VII.1 library, the base ENDF/B-VII.1 library with ^{65}Cu ENDF/B-VIII.0 cross section substitution, and with the full ENDF/B-VIII.0 library.

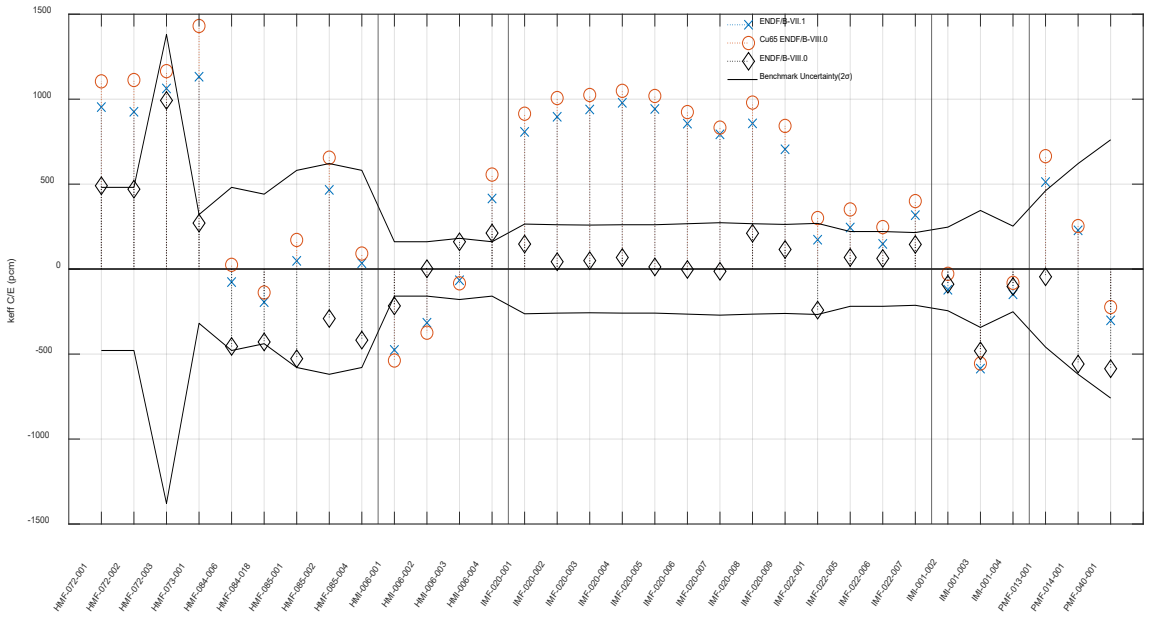

Figure 39– Copper-65 ENDF/B-VIII.0 C/E by Library

Changes from ^{65}Cu ENDF/B-VIII.0 data result in a deterioration in the agreement with experimental data, with 41% of benchmarks in ENDF/B-VII.1 bounded by 2 sigma, as opposed to 31% of ENDF/B-VIII.0 substituted ^{65}Cu cross sections. Expressing

deviation in terms of sigma results in an average deviation of 3.48 sigma for ENDF/B-VII.1 and 3.99 sigma for ENDF/B-VIII.0 ^{63}Cu substituted cross sections. Figure 41 goes into further detail by plotting absolute changes as a result of cross section adjustments. The primary observation is that in most cases, the replacement results in an increase in criticality. However, three configurations do not; the first three HMI cases see a decrease. Surprisingly, these outliers are the only configurations which match the estimate of revisions given in Background and Relevance. Rather, the given expectation appears to be incorrect; while elastic scattering was the dominant sensitivity, and while there was significant reduction in the elastic cross section, there was a net positive effect on criticality. These changes are relatively significant, with most configurations resulting in a statistical increase in criticality. Perhaps as was the case with ^{63}Cu, the capture cross section decrease resulted in the observed increase in criticality. An additional explanation is the placement and dispersion of the resonances.

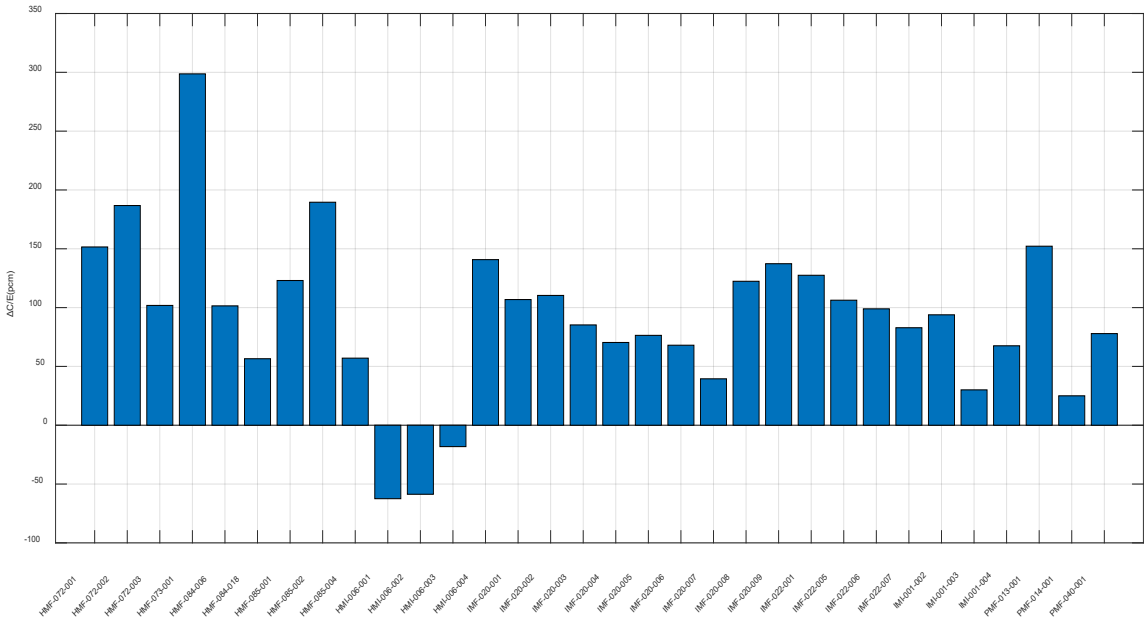

Figure 40– Copper-65 ENDF/B-VIII.0 Change in C/E

Given the lower energy of its first resonance peak, the overall scattering cross sections for the spectrums of the configurations investigated had an elevated sensitivity at that energy, resulting in a significant increase from the lower energy resonance. Changes with respect to sensitivity are shown in 4.2.4 Copper-65. Table 7 lists the various averages of the different libraries. The overall mean deviation increases 90.1 pcm. 9% of cases had an increase or decrease of 1 sigma experimental uncertainty, and no configurations had an increase or decrease of 2 sigma or greater. Absolute measures of deviation show a significant increase; in terms of experimental error, deviations increased 0.51 sigma; in absolute terms, experiment deviations increased an average of 75.7 pcm; and expressed as a root mean square, deviations increased 91.0 pcm. This increase is particularly notable given the extreme improvement in ^{63}Cu.

Table 7– Copper-65 Isotopic Substitution Averages

Average:	ENDF/B-VII.1	Cu-65 ENDF/B-VIII.0	ENDF/B-VIII.0
Relative Deviation	3.48σ	3.99σ	1.24σ
Mean Deviation	379.9±39.3	470.0±39.3	-29.1±39.3
Absolute Mean Deviation	522.6±39.3	598.3±39.3	249.4±39.3
Root Mean Square Deviation	630.5±46.0	721.5±45.1	337.8±74.8

As seen in Figure 42, the introduction of the ENDF/B-VIII.0 ^{65}Cu cross section data results in worsened agreement with a normal distribution. This coincides with previously noted conclusions; presented as such, not only are the general trend and outliers noted, but doing so in effect expands the range of deviations.

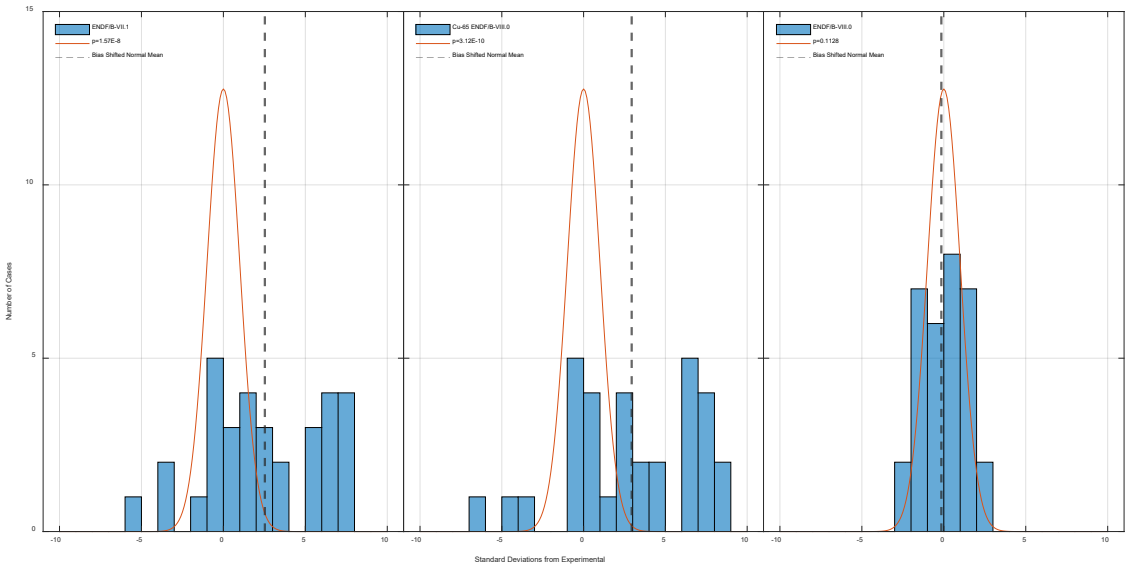

Figure 41– Effect of ENDF/B-VIII.0 Data on Normality; Copper-63 and Full Library

ENDF/B-VII.1 data varied between -6 and 8 sigma, whereas the substitution results in variations between -7 and 9 sigma. Table 8 accounts for the effect of the shift in the mean or bias, showing that adjusting for bias, the general shape of normality worsens as a result of aforementioned outward expansion, along with an increase in bias with experimental data. This confirms the increased bias in the data; the data becomes less likely a result of normal distribution, with an increased overall bias of 0.41 standard deviations greater than with ENDF/B-VII.1 data.

Table 8– P-values Accounting for Copper-65 Bias

	Maximum P-value	Shift from Normality
ENDF/B-VII.1	8.3937E-4	2.53σ
Cu65 ENDF/B-VIII.0	3.5098E-4	2.94σ
ENDF/B-VIII.0	0.2016	-0.15σ

Accounting for this bias, the data remains less normally distributed, agreeing with the general trend noted in earlier analysis. This is driven by changes occurring in the

positive and negative peripherals, where the variations in criticality shifts the full distribution outward.

4.1.5 Elemental Copper

The results of isotope substitutions are located in C.5 Elemental Copper, as well as the calculated C/E values and uncertainties from data in A.3 Copper-63 and Copper-65. These C/E values are plotted by identifier in Figure 43. C/E values are presented with the full ENDF/B-VII.1 library, the base ENDF/B-VII.1 library with natural abundance Cu ENDF/B-VIII.0 cross section substitution, and with the full ENDF/B-VIII.0 library. Changes from Cu ENDF/B-VIII.0 data results in an improvement in the agreement with experimental data, with 41% of benchmarks in ENDF/B-VII.1 bounded by 2 sigma, and 63% of ENDF/B-VIII.0 substituted Cu cross sections. This is to be expected with results from ^{63}Cu and ^{65}Cu showing an extreme improvement and a subtle worsening, respectively.

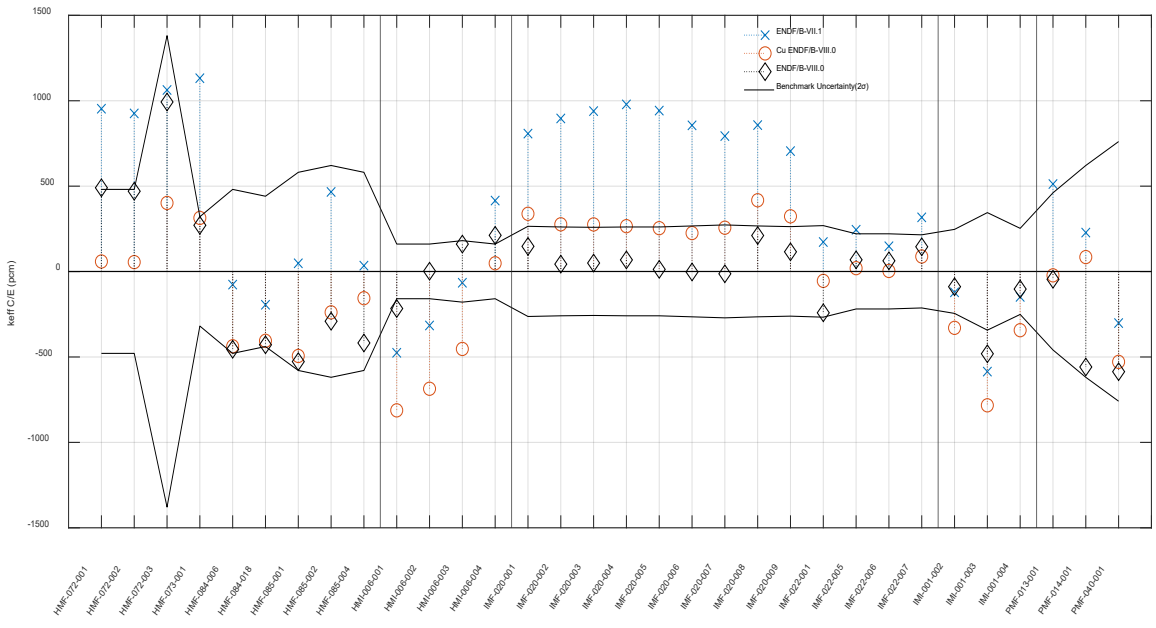

Figure 42– Copper ENDF/B-VIII.0 C/E by Library

Expressing deviation in terms of sigma results in an average deviation of 3.48 sigma for ENDF/B-VII.1 and 2.09 sigma for ENDF/B-VIII.0 Cu substituted cross sections. Figure 44 goes into further detail by plotting absolute changes as a result of cross section adjustments.

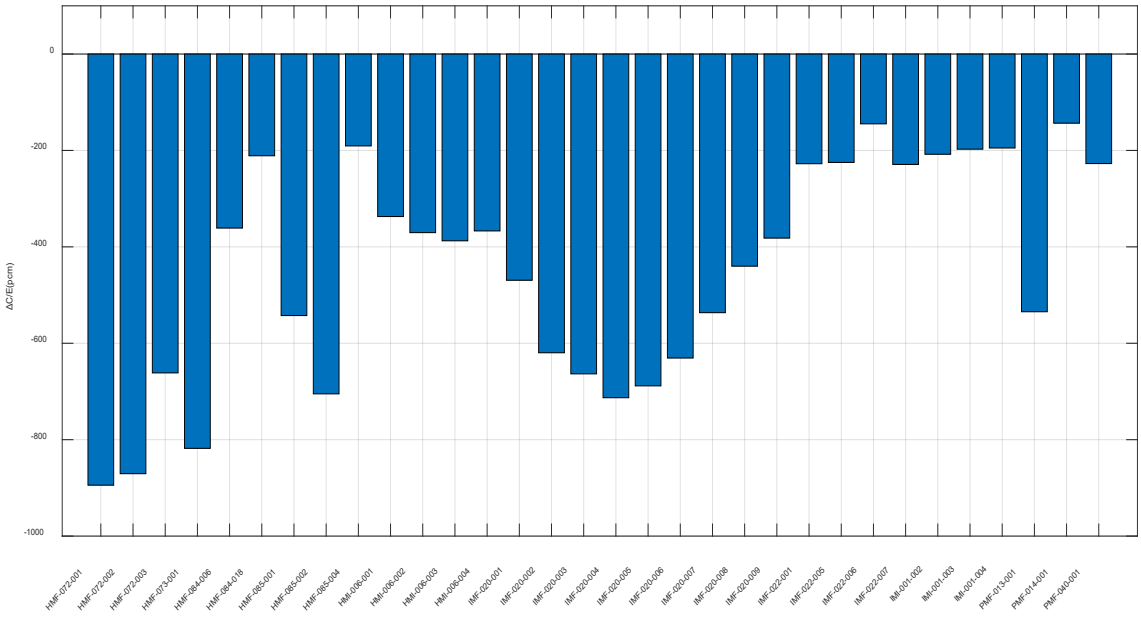

Figure 43– Elemental Copper ENDF/B-VIII.0 Change in C/E

The primary observation that in every configuration, the replacement results in a significant reduction in criticality. These changes are extremely significant, with a minimum decrease of 150 pcm. Given the assessments noted earlier in Copper-63 and Copper-65, and the fact that Cu is majority ^{63}Cu, that the results for natural abundance are effectively suppressed ^{63}Cu is justifiable. Changes with respect to sensitivity are shown in 4.2.5 Elemental Copper.

Table 9 lists the various averages of the different libraries. The overall mean deviation decreases 443.5 pcm. 84% of configurations had a decrease of 1 sigma

experimental uncertainty or greater, 63% of configurations had a decrease of 2 sigma or greater, and 47% had a decrease of 3 sigma or greater. Absolute measures of deviation show a significant decrease; in terms of experimental error, deviations decreased 1.39 sigma; in absolute terms, experiment deviations decreased an average of 227.2 pcm; and expressed as a root mean square, deviations decreased 267.3 pcm.

Table 9– Elemental Copper Isotopic Substitution Averages

Average:	ENDF/B-VII.1	Cu ENDF/B-VIII.0	ENDF/B-VIII.0
Relative Deviation	3.48σ	2.09σ	1.24σ
Mean Deviation	379.9±39.3	-63.6±39.3	-29.1±39.3
Absolute Mean Deviation	522.6±39.3	295.4±39.3	249.4±39.3
Root Mean Square Deviation	630.5±46.0	363.2±39.7	337.8±74.8

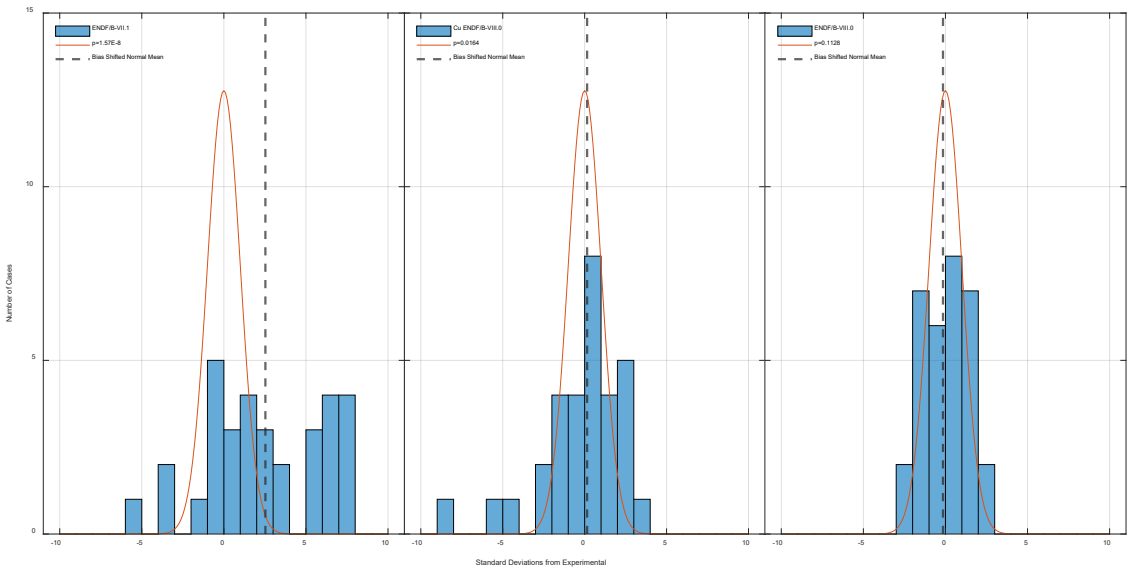

Figure 44– Effect of ENDF/B-VIII.0 Data on Normality; Elemental Copper and Full Library

As seen in Figure 45, the introduction of the ENDF/B-VIII.0 ^{63,65}Cu cross section data results in improved agreement with a normal distribution. Again, improvements are a mix of the impacts from ^{63}Cu and ^{65}Cu. Table 10 displays the effect of the shift in bias,

showing that adjusting for bias, the general shape of normality improves along with an decrease in bias with experimental data. This confirms the decreased bias in the data; the data becomes more likely a result of normal distribution, with a decreased overall bias of 2.38 standard deviations lower than with ENDF/B-VII.1 data.

Table 10– P-values Accounting for Elemental Copper Bias

	Maximum P-value	Shift from Normality
ENDF/B-VII.1	8.3937E-4	2.53σ
Cu ENDF/B-VIII.0	0.0287	0.15σ
ENDF/B-VIII.0	0.2016	-0.15σ

Accounting for this bias, the data becomes more normally distributed, agreeing with the general trend noted in earlier analysis. This is driven by changes occurring in the positive peripherals, where the variations in criticality shifts the full distribution down.

4.2 Sensitivity Analyses

While the various "Change in C/E" figures are useful for visually augmenting the changes, the data itself is unorganized. In this portion of results, these changes will be examined on a sensitivity basis. Rather than by identifier, changes will be plotted by the respective configuration's sensitivity to the isotope of interest. Sensitivity data will be reported as the integrated total sensitivities tabulated in APPENDIX A. Sensitivities; By Isotope.

4.2.1 Oxygen-16

Figure 46 shows the relation between the total ^{16}O sensitivity and the change in C/E values from the substitution of ENDF/B-VIII.0 ^{16}O cross sections. Most changes were outside computational uncertainty and can be attributed to the change in cross section

alone. Given the computational uncertainty in the criticalities, it would be expected that the changes would not result in a perfect fit. Nevertheless, as evidenced by the figure, there is a clear trend in the results, with greater sensitivities resulting in greater changes in criticality. By plotting the data with associated evaluation identifiers, trends in experimental series can be noted. Particularly, PST systems see an amplified reduction relative to other experiments with similar sensitivities; being further below the trend. The HST series are very tightly related and following the trend as well, which would be expected to an extent with similar experimental conditions and operation. Non-thermal experiments show lessened reductions, although accounting for the PST suppression in the trend, these experiments lie in further agreement with others.

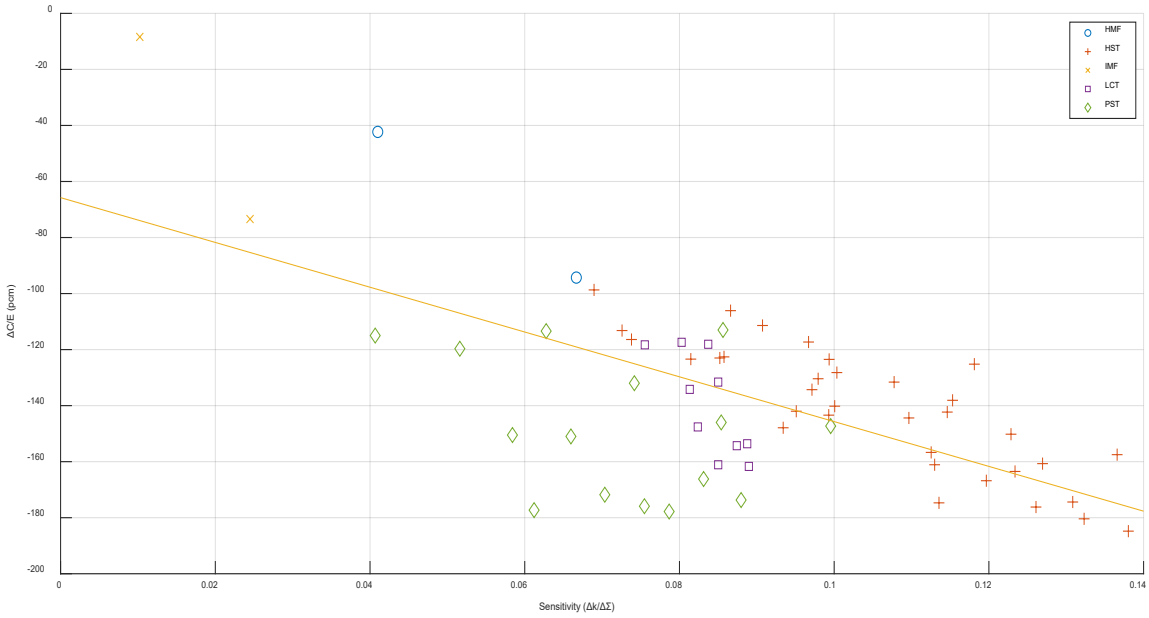

Figure 45– Oxygen-16 ENDF/B-VIII.0 Change in C/E by Sensitivity

Not only does this confirm the selected set of benchmarks as appropriate for measuring the impacts of cross section changes, but it raises the question of how these

results would look with higher precision. While there is a trend of higher sensitivity leading to greater deviation, it is interesting to note that the lowest the deviations reach, -180 pcm, is reached at a wide range of sensitivities, from 0.06 to 0.14.

By increasing the precision of CSAS calculations, the effects of computational uncertainty could be diminished, and whether this bottoming is a result of general uncertainties or an underlying data issue could be determined. Additionally, when repeating this figure with sensitivities in terms of 10 pcm/ΔΣ, and setting the intercept to zero (forcing the trend to be one to one; zero sensitivity should in theory result in zero variability apart from computational variance), the slope of the trendline becomes -1.47; markedly close to the average decrease in the thermal and intermediate cross section as noted in Oxygen-16 Cross-Section Revisions. The slope in these plots are, after all, a Δk_{eff} divided by an expected $\Delta k_{eff}/\Delta\Sigma$; or $\Delta\Sigma$. This observation is likely to be unique in this work, as ^{16}O had one relevant cross section change, which was effectively constant over the majority of the spectrum, with results confirming assessments in Background and Relevance.

4.2.2 Iron-56

Figure 47 shows the relation between the total ^{56}Fe sensitivity and the change in C/E values from the substitution of ENDF/B-VIII.0 ^{56}Fe cross sections. Most changes were within computational uncertainty and cannot be attributed to the change in cross section alone. As shown in the figure, there is no substantial trend in the results, beyond the several configurations with a sensitivity greater than 0.08. This data can produce three conclusions; either the change in cross sections is too marginal to produce any significant

variation in criticalities, the changes in the different reactions counter one another, or the selected experiments are not sensitive enough to show substantial variation. In either case, the inclusion of additional experiments at higher sensitivities and lower computational uncertainties would be the most effective method of improving such an analysis.

Improvements in C/E values are still valid, albeit still marginal; rather, for a more thorough investigation of the three reasonings, increased precision over a greater number of experiments would be more conclusive.

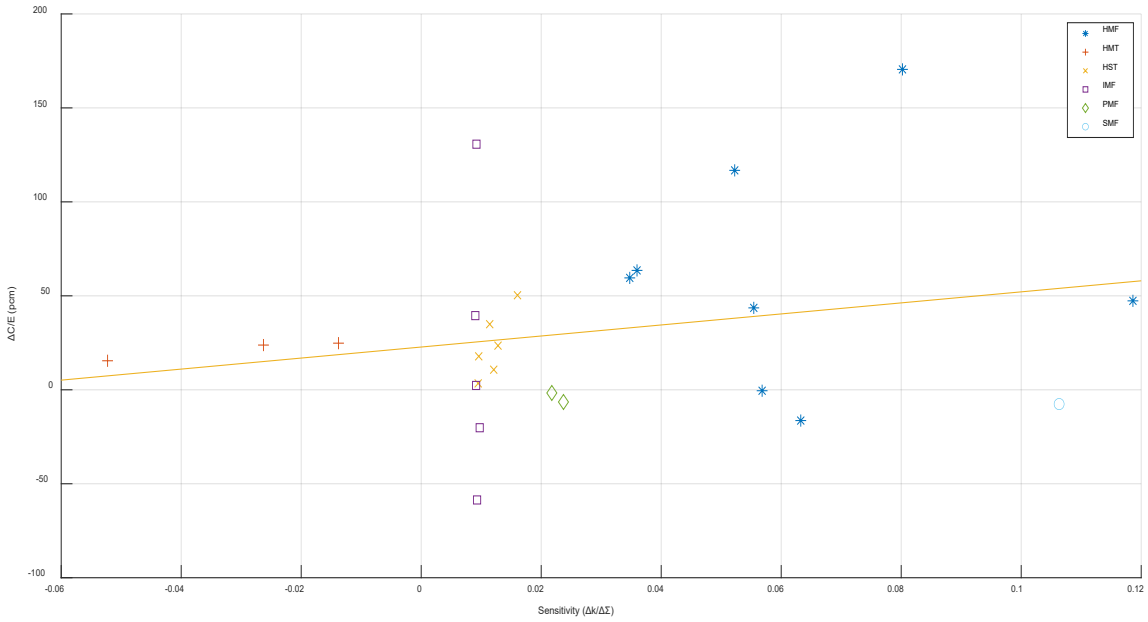

Figure 46– Iron-56 ENDF/B-VIII.0 Change in C/E by Sensitivity

Viewing changes by identifier, it's obvious the inconsistency in the IMF series of experiments. Despite bordering on exclusion for its low sensitivity, the variations as a result of ^{56}Fe show a wide range of variation, from -50 pcm to nearly 150 pcm, consisting of the second largest positive increase, and largest decrease as well. These cases are known for their copper sensitivity, which has been shown to have significant variation between

libraries. A potential reason for this discrepancy is these cases' copper sensitivities, with the changes in iron cross sections such as the increase in intermediate and fast capture, causing cascading effects on the copper. However, this effect is not seen in PMF cases, also copper sensitive, nor the 3 iron sensitive ZEUS cases. Other evaluations show no trends, largely as most changes are irrelevant. Apart from the IMF series, the only significant changes occur with the HMF evaluations.

4.2.3 Copper-63

Figure 48 shows the relation between the total ^{63}Cu sensitivity and the change in C/E values from the substitution of ENDF/B-VIII.0 ^{63}Cu cross sections. All changes were well outside computational uncertainty and can be attributed to the change in cross section alone. Given the computational uncertainty in the criticalities, it would be expected that the changes would not result in a perfect fit. Nevertheless, as evidenced by the figure, there is a clear trend in the results, with greater sensitivities resulting in greater changes in criticality. This confirms the selected set of benchmarks as appropriate for measuring the impacts of cross section changes. Increased precision could factor into updating these results. However, the scale of changes in ^{63}Cu criticalities are nearly an order of magnitude greater than changes from ^{16}O, and therefore computational uncertainty makes up less of a fraction of the variability. Therefore, while improved precision would improve the data, there would be little effective change to the trend.

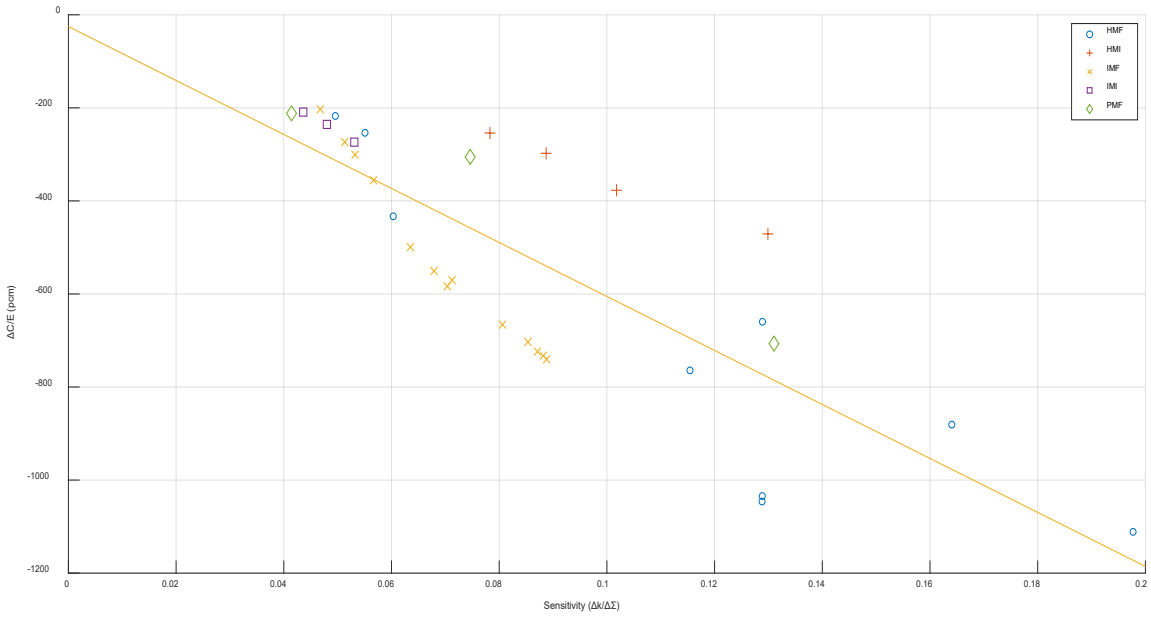

Figure 47– Copper-63 ENDF/B-VIII.0 Change in C/E by Sensitivity

Plotting changes by identifier, there are several noticeable trends. First of which is the increased reduction in the FR0 series (IMI and IMF) relative to the overall trend, with lower sensitivities having less of a reduction, while at higher sensitivities showing greater reduction. Examining sensitivity data as well as fission energy ranges, the FR0 experiments show a general trend of an increased percentage of fast fissions with an increasing sensitivity. Given the increase in sensitivity is clearly shown with the x-axis, the trend of the FR0 series shows greater reductions with faster spectrums. This increased reduction in fast systems relative to intermediate systems of the same experimental series is shown in the ZEUS series as well, where the HMI series having fissions in intermediate energies, show a suppressed reduction relative to the general trend, whereas the HMF ZEUS cases (not explicitly marked in Figure 48, but with sensitivity data given in various figures and appendices) at the bottom right of the graph show increased reductions, at the 0.13 sensitivity mark below 1000 pcm deduction.

4.2.4 Copper-65

Figure 49 shows the relation between the total ^{65}Cu sensitivity and the change in C/E values from the substitution of ENDF/B-VIII.0 ^{65}Cu cross sections. Several changes were within the scope of being attributable to computational uncertainty, but most cases can be attributed to the change in cross section alone. Given the computational uncertainty in the criticalities relative to the changes seen, it would be expected that the changes would not result in a perfect fit. However, the three cases where there is a decrease in criticality are interesting as outliers. Upon investigation of the sensitivity profiles, rather than total integrated sensitivities, the three ZEUS cases at the source of the discrepancy are noticeably more intermediate than other cases in the validation. Further, the elastic sensitivity of the three cases around the 2 keV energies are markedly elevated relative to other cases; as it happens, the noted first resonance revision occurs at a similar (noting that sensitivity data is presented in 252-multigroup) energy. Considering the ZEUS cases were a driving force in noticing the need for revised intermediate copper and ^{235}U cross sections, it seems fitting for the intermediate cases to again provide noteworthy results. Without these outlier cases, the linear fit would be a steeper curve with better agreement across configurations as a function of sensitivity. As evidenced by the figure, there is a clear trend in the results even with outliers, with greater sensitivities largely resulting in greater changes in criticality. With most changes beyond computational uncertainty, this set of benchmarks is appropriate for measuring the impacts of cross section changes. Increased precision could still be a useful factor in updating these results, particularly regarding further examination of the three outliers. Unlike with ^{63}Cu criticalities, ^{65}Cu changes in

criticality do have several cases that could largely be a result of uncertainty; increased precision would confirm whether the variations in those cases were genuine.

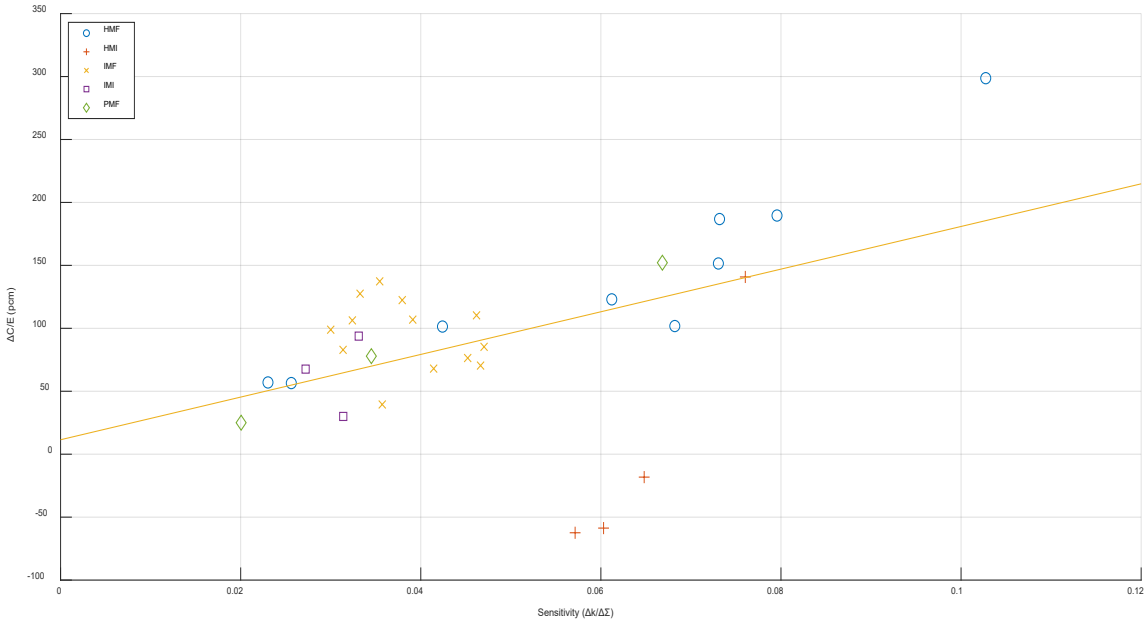

Figure 48– Copper-65 ENDF/B-VIII.0 Change in C/E by Sensitivity

4.2.5 Elemental Copper

Figure 50 shows the relation between the total copper sensitivity and the change in C/E values from the substitution of ENDF/B-VIII.0 copper cross sections. As elemental copper is an amalgamation of ^{63}Cu and ^{65}Cu, the sensitivities and variation in criticalities will be a blend of both results. All changes were well outside computational uncertainty and can be mainly attributed to the change in cross sections. As shown by the figure, there is a clear trend in the results, with greater sensitivities resulting in greater changes in criticality. With 100 or more pcm change, the selected set of benchmarks is appropriate for measuring the impacts of cross section changes. While an increased precision would

likely improve the data on lower sensitivity configurations and remove contributions from uncertainty, the overall trend would remain largely the same.

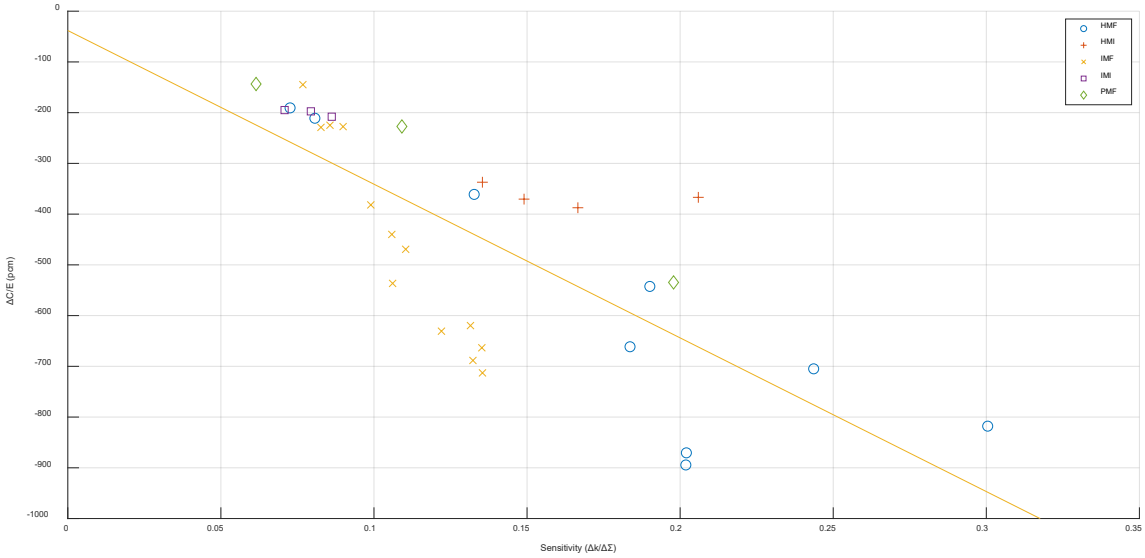

Figure 49– Copper ENDF/B-VIII.0 Change in C/E by Sensitivity

Combining effects of ^{63}Cu and ^{65}Cu, the impact on HMI and FR0 series is more apparent. The least intermediate, most copper sensitive HMI case shows lessened reduction relative to other HMI cases, as a result of the first 3 cases being the aforementioned ^{65}Cu outliers. The FR0 series still show the trend of increased reduction with increased sensitivity and the related general increase in number of fast fissions.

4.3 Complete ENDF/B-VIII.0 Library Assessment

The results of the full ENDF/B-VIII.0 library substitution are located in APPENDIX B, as well as the uncertainties and calculated C/E values from data in APPENDIX A and C. These C/E values are plotted by identifier in Figure 51. Unlike

other plots, identifiers are removed from the axes for visibility, with 102 cases; they remain in alphanumerical order as in APPENDIX B, and are numbered accordingly.

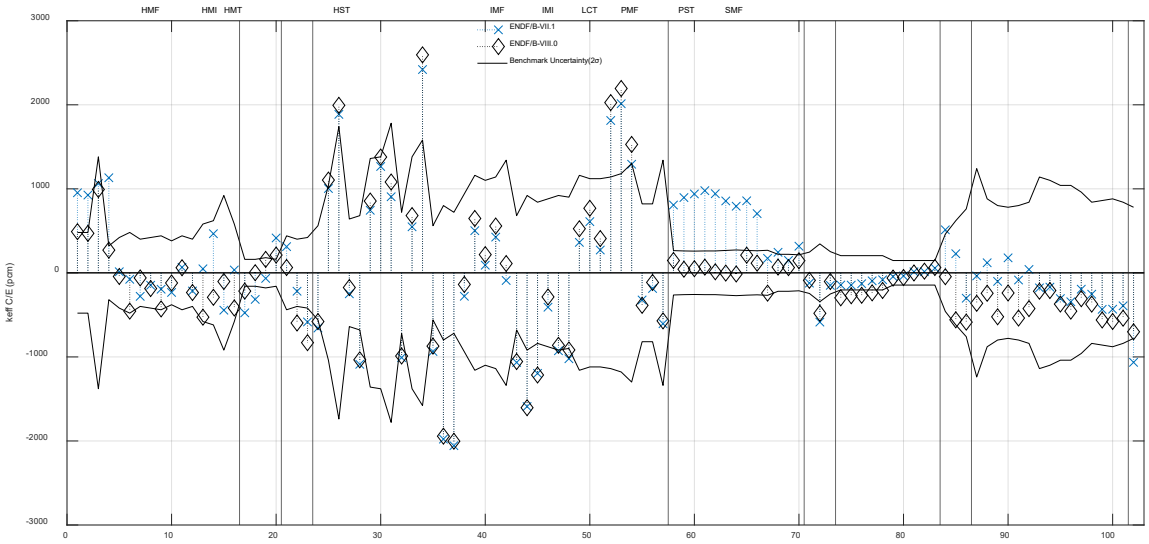

Figure 50– ENDF/B-VIII.0 C/E by Library

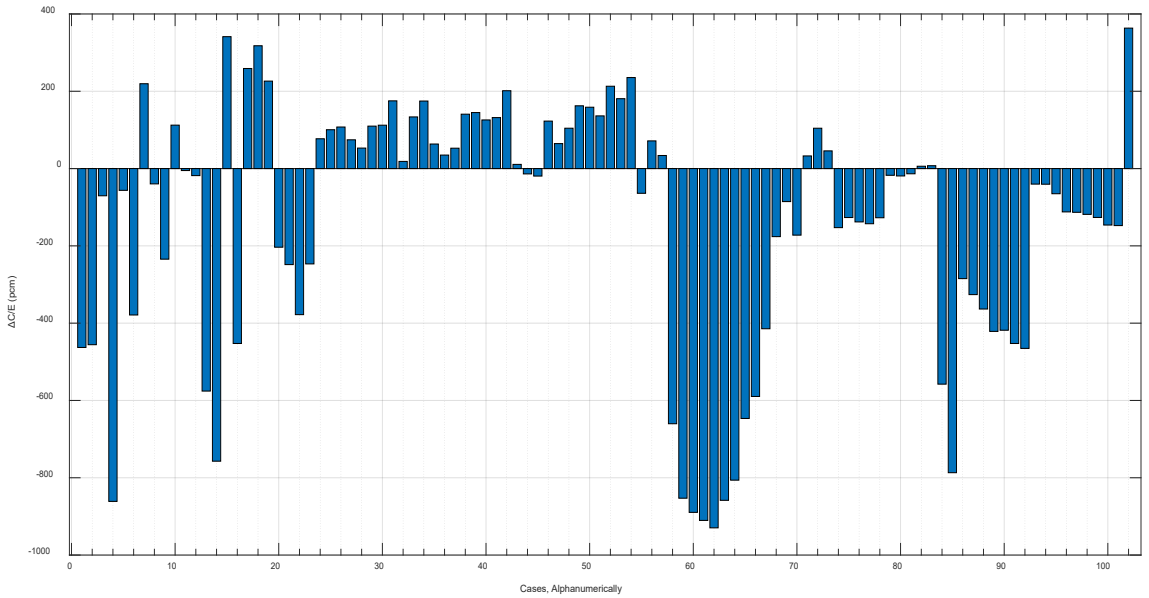

Figure 51– ENDF/B-VIII.0 Change in C/E

C/E values are presented with the full ENDF/B-VII.1 library and the full ENDF/B-VIII.0 library. Changes from ENDF/B-VIII.0 data result in an improvement in the agreement with experimental data, with 65% of benchmarks in ENDF/B-VII.1 bounded by 2 sigma, and 74% of benchmarks in ENDF/B-VIII.0. Expressing deviation in terms of sigma results in an average deviation of 2.01 sigma for ENDF/B-VII.1 and 1.45 sigma for the full ENDF/B-VIII.0 library. Figure 52 shows changes from the full library substitution; 85% of cases resulted in a change greater than 50 pcm, attributable to cross section library change.

Table 11 lists the averages of all configurations in this work, in both ENDF/B-VII.1 and ENDF/B-VIII.0 libraries. The overall mean deviation decreases 125.9 pcm. Absolute measures of deviation show a considerable decrease; in terms of experimental error, deviations decreased 0.56 sigma; in absolute terms, experiment deviations decreased an average of 42.2 pcm; and expressed as a root mean square, deviations decreased 20.7 pcm. 40% of cases had a change of 1 sigma experimental uncertainty or greater, 18% of configurations had a change of 2 sigma or greater, and 13% of cases had a change of 3 sigma or greater.

Table 11– ENDF/B-VII.1 vs ENDF/B-VIII.0 Averages

Average:	ENDF/B-VII.1	ENDF/B-VIII.0
Relative Deviation	2.01σ	1.45σ
Mean Deviation	65.4±39.2	-60.5±39.2
Absolute Mean Deviation	550.3±39.2	508.1±39.2
Root Mean Square Deviation	760.5±52.2	739.8±57.4

Finally, as shown in Figure 53, there was remarkable improvement in the distribution of C/E deviations when related to experimental uncertainties. A 0.56 decrease from an average of 2.01 to 1.45 seems unremarkable; after all, being absolute measures, values are limited to a minimum of zero.

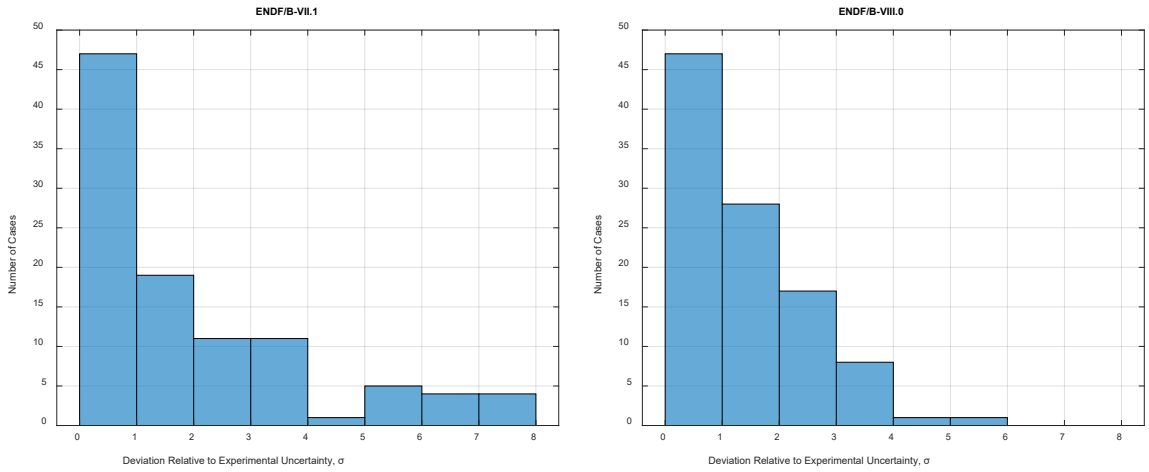

Figure 52– ENDF/B-VIII.0 Improvements Relative to Experimental Error

However, when noted that for a true normal distribution, the average deviation would be sqrt(2/pi) ≈ 0.8, this 0.56 decrease is nearly half of the 1.21 sigma change that necessary for the ENDF/B-VIII.0 deviations to be normal [39]. While the number of cases within 1 sigma remained the same, peripheral values noticed enormous improvement; the 25 cases greater than 3 sigma reduced to 10, while the 14 cases greater than four sigma reduced to two cases. These outliers are listed in Table 12. As evidenced by these outliers, the full library substitution substantially improved agreement; only one case (HMT-015) out of all 102 became an outlier in ENDF/B-VIII.0 where it wasn't in ENDF/B-VII.1. Of the remaining outliers greater than 3 sigma, only iron and oxygen sensitive experiments remain. All 16 cases that lost their status as 3 sigma outliers were copper sensitive, as were

all 12 cases that lost their status as 4 sigma outliers, again establishing the value of the copper evaluation.

Table 12– ENDF/B-VII.1 and ENDF/B-VIII.0 Outliers

ENDF/B-VII.1 Outliers (>3σ)	ENDF/B-VIII.0 Outliers (>3σ)	ENDF/B-VII.1 Outliers (>4σ)	ENDF/B-VIII.0 Outliers (>4σ)
HMF-072-001			
HMF-072-002			
HMF-073-001		HMF-073-001	
HMI-006-001		HMI-00 6-001	
HMI-006-002			
HMI-006-004		HMI-006-004	
	HMT-015-001		
HST-015-002	HST-015-002		
HST-016-003	HST-016-003		
HST-017-001	HST-017-001		
HST-017-002	HST-017-002	HST-017-002	HST-017-002
HST-017-003	HST-017-003	HST-017-003	HST-017-003
HST-018-001	HST-018-001		
HST-018-002	HST-018-002		
HST-018-010	HST-018-010		
HST-018-011	HST-018-011		
IMF-020-001		IMF-020-001	
IMF-020-002		IMF-020-002	
IMF-020-003		IMF-020-003	
IMF-020-004		IMF-020-004	
IMF-020-005		IMF-020-005	
IMF-020-006		IMF-020-006	
IMF-020-007		IMF-020-007	
IMF-020-008		IMF-020-008	
IMF-020-009		IMF-020-009	
IMI-001-003			

Figure 54 displays the data as relative non-absolute deviations; while Figure 53 displays the improvements absolutely in terms of distance from complete agreement with experimental, the use of bins loses accuracy in determining the actual performance. In effect, a deviation of -0.99 sigma and 0.99 sigma would be portrayed within the same bin,

despite a 2 sigma deviation between the two values. Testing for normality does so on the values themselves, rather than grouping by indices.

While the distribution seemingly becomes more normalized in absolute terms, removing this absoluteness shows that both distributions are not normal, with ENDF/B-VIII.0 having a lower p-value; not in itself an indicator ENDF/B-VIII.0 values are less normal, particularly considering the magnitude of the p-values in both cases are effectively zero, but there is no definite improvement on the surface.

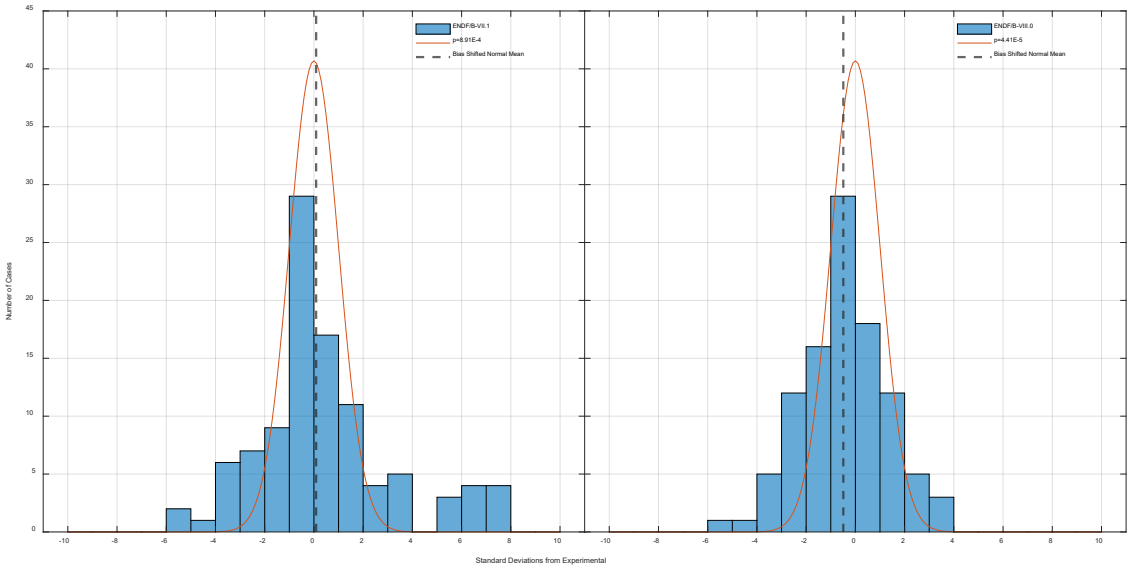

Figure 53– Effect of Full ENDF/B-VIII.0 Library on Normality

Accounting for the known bias and negative shift however, Table 13 exhibits what is visible in both previous figures.

Table 13– P-values Accounting for Full ENDF/B-VIII.0 Library Bias

	Maximum P-value	Shift from Normality
ENDF/B-VII.1	0.0016	0.09σ
ENDF/B-VIII.0	0.0098	-0.49σ

While the raw data has a lower p-value, accounting for the bias and shifting the distribution shows an improvement in the agreement in the ENDF/B-VIII.0 shape relative to ENDF/B-VII.1; the values are overall lower, but in a slightly more defined normal distribution. Given 60% of cases are oxygen sensitive, which showed a worsened decrease in values, future work could address the improvement as a result of removing the ENDF/B-VIII.0 ^{16}O data, and determining normality of the near full library with the removal of this established negative bias.

CHAPTER 5. SUMMARY AND CONCLUSIONS

In total, 102 benchmarked configurations pulled from 22 evaluations were modeled in SCALE 6.2.3 based on sensitivities to ^{16}O, ^{56}Fe, ^{63}Cu, and ^{65}Cu. While some changes from cross section substitutions were insignificant, ENDF/VIII.0 revisions showed considerable variations regarding several specific isotope changes, and the library as a whole.

Most ^{16}O results were statistically significant, resulting in a consistent decrease in criticality, representing a worsening of agreement with experimental values. Criticality changes seemed to floor at a reduction of 180 pcm regardless of sensitivity, while decreasing an average of about 140 pcm. A net 12% of cases were no longer bounded by a two sigma experimental uncertainty interval, and the average sigma of all cases increased by 0.34, reflecting deterioration in the accuracy of ^{16}O cross sections. Every other measure of comparing calculated and experimental values also showed a deterioration with absolute increases in deviations. The change in criticality per sensitivity was, perhaps coincidentally, on par with the cross-section revisions themselves. However, given the consistent cross section changes in thermal and intermediate energies and the abundance of thermal experiments, changes resemble a density perturbation, the exact method used for the confirmation of sensitivity data. In summary, a slight negative bias in ^{16}O benchmarks was augmented by a further decrease in the ENDF/B-VIII.0 ^{16}O elastic scattering cross section. The overall ENDF/B-VIII.0 library substitution somewhat offset this increased negative bias, with selected experiments re-approaching experimental values relative to the isotopic substitutions, but without ^{16}O substitutions, perhaps the full library would perform more accurately.

Most ^{56}Fe variations were statistically insignificant; of the significant changes, variations were an increase in criticality, as reflected with the mean increasing by 30 pcm. Net containment by two-sigma increased by 8%, and the average departure expressed as sigma decreased 0.07, a marginal if not negligible improvement. With such minimal changes in criticalities and the underlying cross sections, ^{56}Fe cross section revisions may not be variable enough to produce a significant effect; alternatively, additional cases may be needed before determination of whether the improvement noticed are legitimate improvements. Given the slight variations, such modeling should be performed at a higher level of precision to decrease computational uncertainty intervals. However, even at a higher precision, the results given are accurate for determining general changes; even with improved uncertainties, variations would still be under 50 pcm and marginal. While selected experiments show effectively no variation as a result of revisions, the bias marginally increased, contradictory to the decrease in terms of average deviation in experimental uncertainty. Given this contradiction, previously negatively biased configurations gained positive reactivity as a counter, resulting in more accurate results with a higher bias. For the selected experiments, the full ENDF/B-VIII.0 library substitution significantly reduced overall bias, with decreased uncertainty deviations as well. While ENDF/B-VIII.0 ^{56}Fe alone had minimal effect on its sensitive benchmarks using a ENDF/B-VII.1 base library, the revised ^{56}Fe cross sections along with the full library may have been an improvement relative to an ENDF/B-VIII.0 base library and ENDF/B-VII.1 ^{56}Fe data.

^{63}Cu showed remarkable improvements between calculated and experimental criticalities. On average, configurations' criticalities decreased over 520 pcm, resulting in

a 1.51 average decrease in sigma. All measures of deviations showed improvement. A net increase of 28% of cases were bounded by two-sigma uncertainty. Given the established significant positive bias in ENDF/B-VII.1 copper cross sections, the evaluation included in ENDF/VIII.0 greatly improves the accuracy of ^{63}Cu, primarily as a result of elastic scattering reductions. Coupled with the full ENDF/B-VIII.0 library, bias reduces even further to near parity with experimental values.

^{65}Cu criticality variations were largely significant, resulting in a 0.51 sigma increase in deviations, and a mean increase of 90 pcm. The three most intermediate ZEUS cases were outliers in the general trend, showing decreases as opposed to increases in all other configurations. Based on the sensitivity profile and known cross section variations, the potential source for this discrepancy is an elastic scattering intermediate resonance, where the three cases in question exhibited a heightened sensitivity to the scattering cross section. There was a 10% net decrease in the number of configurations which had criticalities within two experimental sigma. Whereas ^{63}Cu reduced the significant positive bias in copper benchmarks, ^{65}Cu amplified it with a general increase in criticality. With the same selection of critical experiments, the effect of the full ENDF/B-VIII.0 library is the same as for ^{63}Cu, ^{65}Cu, and natural abundance.

The natural copper abundance, combining ^{63}Cu and ^{65}Cu, shows a muted bias reduction, but still significant progress. As copper is used in its natural abundance, the performance of ^{63}Cu and ^{65}Cu together is more useful for actual applications; knowing how both perform independently is still of interest to continue improvements in data accuracy. The mean deviation decreased 440 pcm, and in terms of experimental uncertainty, the average decreased 1.39 sigma. The changes in the mean for ^{63}Cu and ^{65}Cu sum to the mean

change for elemental copper, within 15 pcm. There was a 22% net increase in the number of configurations which had criticalities within two experimental sigma.

The ENDF/B-VIII.0 library, when replaced for all materials in every configuration, resulted in an average decrease in criticality of 125 pcm and a decrease in terms of experimental error of 0.56 sigma. For the full library, most cases had statistically meaningful variations in criticality as a result of cross section revisions. There was a net 9% increase in the number of configurations which had criticalities within two sigma experimental uncertainty. Cases with extreme discrepancies (greater than four sigma deviation relative to their uncertainties) in ENDF/B-VII.1 showed particularly excellent improvement when substituted with ENDF/B-VIII.0 cross sections, mainly a result of copper substitutions. The distribution of absolute variations as a function of their uncertainties, while not a normal distribution, attains an unmistakable suppressed bell curve shape. This is certainly an improvement, with the lesser deviations increasing in frequency. While bias remains effectively the same magnitude, the sign change and deviations in terms of sigma indicate major reductions took place in mostly supercritical benchmark calculations, i.e. copper sensitive benchmarks. The bias magnitude stability with improved results indicates that bias is reaching a threshold within which bias will oscillate as the overall values converge to as well. After all, even with entirely accurate cross sections, the average k_{eff} will fluctuate about exact criticality due to computational uncertainty, while the standard deviation decreases, and the divergence tightens.

Based on these results, the significance of these variations indicates the utility of sensitivity profiles to accurately predict changes in criticality. Even though individually, ^{16}O and ^{65}Cu showed increased divergence from benchmark experimental criticalities, the

potential for an improvement in ^{56}Fe cross sections remains, and ^{63}Cu cross sections overwhelmingly improved. While not all isotopes showed improvements, ^{63}Cu and the full library variations resulted in greatly improved experimental agreement, showing the benefits of consistent cross section revisions.

This data provides an initial foundation for those involved in the nuclear criticality safety validation of ^{16}O, ^{56}Fe, and ^{63,65}Cu systems, providing data on validation for similar systems of interest. To such an audience, this work exhibits a selection of potentially appropriate benchmark evaluations for use in respective criticality safety evaluations and validations, as well as provides initial results with which to contrast their own self-determined biases and performance concerns. For such application systems, this data would prove useful in providing nuclear data trends early in the evaluation process for those utilizing ENDF/B-VIII.0 cross sections. The produced results, representing the determined bias effects from the ENDF/B-VIII.0 nuclear data evaluation relative to ENDF/B-VII.1, while dependent on the benchmark parameters and therefore uncertainties, are largely a function of the nuclear data changes and calculational uncertainties, as benchmark parameters are consistent across nuclear data substitutions. These biases and accompanying uncertainties, along with the benchmark and application system uncertainties, would contribute to the application's calculated criticality and bias.

For nuclear criticality safety applications, these produced biases would be applied to the bias and uncertainty of the appropriate application system to determine the system's total bias, the uncertainty in said bias, and subsequently an appropriate subcriticality limit constructed in part by these values. In the instance of ^{16}O displaying a solid negative bias with ENDF/B-VIII.0, systems would show a reduction in the likelihood of criticality as a

result of the increased negative bias, culminating in an appropriately revised subcritical limit after accounting for the respective uncertainties. In addition to providing feedback on subcritical limits, these bias estimates reflect the performance of the underlying nuclear data.

With the stated results, recommendations can be given to the appropriate utilization and continued evaluation of the presented cross sections. It has thus far been established that the evaluation of nuclear data is an enduring process, cyclically dependent on validation to bring notice to data requiring improvement, with validation driving evaluation interests. In the instance of ^{65}Cu, results show notable outliers in the incorporation of ENDF/B-VIII.0 data, in addition to an increased positive bias. The general trend, outliers notwithstanding, points to considerable discrepancies between calculated and experimental results. The bias effect as a result of ENDF/B-VIII.0 substitution is small, particularly relative to ^{63}Cu bias reductions, but comes atop the significant previous ENDF/B-VII.1 bias as well. The outliers themselves point to further issues in the ^{65}Cu evaluation, as not only are the outliers substantially different in ^{65}Cu's effect on the likelihood of criticality, but they increase the deviation in agreement with experimental data as well. With considerable interest in the evaluation of the copper cross sections, the ^{65}Cu data is warranted further evaluation to address the shortcomings between continuous-energy calculations and integral experiment data.

Additionally, further evaluation of ^{16}O is recommended, though regularly occurring regardless. However, with increased negative biases from elastic scattering and to an extent (n,α) capture, and supporting evidence from previous studies, evaluations should consider resolving sources of this increased depression. For example, while the ENDF/B-VIII.0

elastic scattering was largely the source of this increased negative bias, the scattering evaluation itself may be accurate; that is, a competing reaction such as radiative capture may be overly predicted in both ENDF/B-VII.1 and ENDF/B-VIII.0, resulting in increased negative bias that when corrected for would show improvement with current ENDF/B-VIII.0 scattering data. While adjusting data to fit desired objectives appears disreputable, the fact that the ^{56}Fe ENDF/B-VIII.0 evaluation artificially introduced radiative capture background to improve experimental agreement at intermediate energies indicates that doing so with a solid validation basis is permissible, particularly given the limits in cross section measurement and uncertainty.

In addition, while experimental facilities and funding are limited, additional experimentation sampling energy regions and materials of interest is always recommended, but priorities must be established. While ^{16}O and ^{56}Fe sensitive evaluations are abundant, the same cannot be said for ^{63,65}Cu. In the ICSBEP handbook, while there are dozens of copper sensitive configurations, these experiments are not appropriately diverse enough as to reflect most fissile material; that is, nearly all copper sensitive benchmarks are greater than 20% enriched uranium, or plutonium. Particularly given the operation of the KBS-3 storage technique at the Onkalo facility, sufficient experimentation for bias determination and accurate subcriticality limits is vital for long term geological waste depositories. With just over 10 low enriched or mixed uranium-plutonium fuel copper sensitive configurations, the selection of ICSBEP sensitive benchmarks is lacking for such waste storage applications, where fuel will not be such high grade fissile material. With decreased experimental capabilities and increased need for computational validations, such experiments must be performed at higher degrees of precision for increased accuracy and

reduced uncertainty to better suit current nuclear criticality safety procedures, which would also benefit validation work using such improved experimental data.

With this ability to measure cross section improvements, future work will perform similar analyses for the remainder of the CIELO isotopes (^{1}H, ^{235}U, ^{238}U, and ^{239}Pu), as well as additional NCSP isotopes in the 5 year plan: gadolinium ($^{155, 156, 157, 158, 160}$Gd), neptunium (^{237}Np), carbon (^{12}C), tungsten ($^{182, 183, 184, 186}$W), and nickel ($^{58, 60}$Ni). These future results, particularly the remaining CIELO isotopes, will provide data essential for nuclear criticality safety applications, as water (based on ^{16}O and ^{1}H biases) and fissile materials are so heavily applied in single parameter subcritical limits. Additionally, an adjusted ENDF/B-VIII.0 library will be estimated and validated, using the best performing isotopes of ENDF/B-VII.1 and VIII.0. Knowing the isotopes that show increased bias with ENDF/B-VIII.0 data, this estimate will be formed by subtracting the variation from those isotope substitutions from the ENDF/B-VIII.0 full library and validated with actual Monte Carlo calculations. Improvements, or lack thereof, found by producing such a best case library would seek to further confirm results in current and future work, while producing recommendations on appropriate library utilization.

APPENDIX A. SELECTED BENCHMARK EXPERIMENTS AND THEIR RESPECTIVE CRITICALITIES, UNCERTAINTIES, AND SENSITIVITIES; BY ISOTOPE

A.1 Oxygen-16

Evaluation Identifier	Benchmark Experimental Criticality	Benchmark Experimental Uncertainty	Total O-16 Sensitivity %Δk/%Σ
HMF-084-002	0.99940	±0.00210	0.06667
HMF-084-015	0.99950	±0.00210	0.04100
HST-014-001	1.00000	±0.00280	0.10775
HST-014-002	1.00000	±0.00520	0.09074
HST-014-003	1.00000	±0.00870	0.07380
HST-015-001	1.00000	±0.00320	0.11531
HST-015-002	1.00000	±0.00340	0.11355
HST-015-003	1.00000	±0.00680	0.09510
HST-015-004	1.00000	±0.00690	0.09341
HST-015-005	1.00000	±0.00890	0.06896
HST-016-001	1.00000	±0.00360	0.11967
HST-016-002	1.00000	±0.00690	0.10035
HST-016-003	1.00000	±0.00790	0.08147
HST-017-001	1.00000	±0.00280	0.13231
HST-017-002	1.00000	±0.00400	0.12694
HST-017-003	1.00000	±0.00360	0.12338
HST-017-004	1.00000	±0.00470	0.11462
HST-017-005	1.00000	±0.00580	0.09930
HST-017-006	1.00000	±0.00550	0.10007
HST-017-007	1.00000	±0.00570	0.09669
HST-017-008	1.00000	±0.00670	0.08576
HST-018-001	1.00000	±0.00340	0.13658
HST-018-002	1.00000	±0.00460	0.13084
HST-018-003	1.00000	±0.00420	0.12609
HST-018-004	1.00000	±0.00440	0.11812
HST-018-005	1.00000	±0.00460	0.11299
HST-018-006	1.00000	±0.00450	0.10966
HST-018-007	1.00000	±0.00580	0.09793
HST-018-008	1.00000	±0.00560	0.09935
HST-018-009	1.00000	±0.00560	0.09713
HST-018-010	1.00000	±0.00570	0.08661
HST-018-011	1.00000	±0.00590	0.08522
HST-018-012	1.00000	±0.00650	0.07258
HST-019-001	1.00000	±0.00410	0.13803

Evaluation Identifier, cont.	Benchmark Experimental Criticality	Benchmark Experimental Uncertainty	Total O-16 Sensitivity %Δk/%Σ
HST-019-002	1.00000	±0.00410	0.12286
HST-019-003	1.00000	±0.00670	0.11254
IMF-022-006	1.00564	±0.00110	0.01024
IMF-022-007	1.00147	±0.00107	0.02449
LCT-079-001	0.99996	±0.00102	0.08897
LCT-079-002	1.00019	±0.00102	0.08876
LCT-079-003	1.00056	±0.00102	0.08741
LCT-079-004	1.00055	±0.00102	0.08501
LCT-079-005	1.00046	±0.00102	0.08237
LCT-079-006	0.99934	±0.00073	0.08372
LCT-079-007	1.00016	±0.00073	0.08501
LCT-079-008	1.00075	±0.00073	0.08133
LCT-079-009	1.00030	±0.00073	0.08028
LCT-079-010	1.00071	±0.00073	0.07552
PST-034-001	1.00000	±0.00620	0.09955
PST-034-002	1.00000	±0.00440	0.08563
PST-034-003	1.00000	±0.00400	0.07417
PST-034-004	1.00000	±0.00390	0.06277
PST-034-005	1.00000	±0.00400	0.05161
PST-034-006	1.00000	±0.00420	0.04067
PST-034-007	1.00000	±0.00570	0.08797
PST-034-008	1.00000	±0.00550	0.08540
PST-034-009	1.00000	±0.00520	0.08312
PST-034-010	1.00000	±0.00520	0.07867
PST-034-011	1.00000	±0.00480	0.07547
PST-034-012	1.00000	±0.00420	0.07035
PST-034-013	1.00000	±0.00430	0.06597
PST-034-014	1.00000	±0.00440	0.06121
PST-034-015	1.00000	±0.00420	0.05841

A.2 Iron-56

Evaluation Identifier	Benchmark Experimental Criticality	Benchmark Experimental Uncertainty	Total Fe-56 Sensitivity %Δk/%Σ
HMF-072-001	0.99910	±0.00240	0.05682
HMF-072-002	1.00020	±0.00240	0.05543
HMF-072-003	1.00160	±0.00690	0.06326
HMF-084-007	0.99950	±0.00200	0.08021
HMF-084-019	0.99960	±0.00190	0.05225
HMF-084-026	0.99930	±0.00220	0.03597
HMF-084-027	0.99940	±0.00200	0.03476
HMF-085-003	0.99950	±0.00460	0.11862
HMT-013-001	1.00060	±0.00220	-0.05227
HMT-013-002	0.99730	±0.00200	-0.01378
HMT-015-001	1.00010	±0.00210	-0.02629
HST-017-006	1.00000	±0.00550	0.01280
HST-017-008	1.00000	±0.00670	0.00959
HST-018-005	1.00000	±0.00460	0.01605
HST-018-006	1.00000	±0.00450	0.01142
HST-018-008	1.00000	±0.00560	0.01209
HST-018-010	1.00000	±0.00570	0.00950
IMF-020-004	1.00080	±0.00130	0.00902
IMF-020-005	1.00140	±0.00130	0.00915
IMF-020-006	1.00120	±0.00133	0.00921
IMF-020-007	1.00110	±0.00136	0.00931
IMF-022-007	1.00147	±0.00107	0.00975
PMF-013-001	1.00340	±0.00230	0.02177
PMF-014-001	1.00370	±0.00310	0.02371
SMF-014-001	1.00010	±0.00390	0.10632

A.3 Copper-63 and Copper-65

Evaluation Identifier	Benchmark Experimental Criticality	Benchmark Experimental Uncertainty	Cu-63 Total Sensitivity %Δk/%Σ	Cu-65 Total Sensitivity %Δk/%Σ	Total Cu Sensitivity %Δk/%Σ
HMF-072-001	0.99910	±0.00240	0.12881	0.07305	0.20186
HMF-072-002	1.00020	±0.00240	0.12886	0.07318	0.20204
HMF-072-003	1.00160	±0.00690	0.11542	0.06821	0.18363
HMF-073-001	1.00040	±0.00160	0.19771	0.10274	0.30045
HMF-084-006	0.99940	±0.00240	0.06032	0.04241	0.13273
HMF-084-018	0.99950	±0.00220	0.05508	0.02562	0.08070
HMF-085-001	0.99980	±0.00290	0.12889	0.06121	0.19010
HMF-085-002	0.99970	±0.00310	0.16405	0.07956	0.24361
HMF-085-004	0.99960	±0.00290	0.04957	0.02303	0.07260
HMI-006-001	0.99770	±0.00080	0.07828	0.05714	0.13542
HMI-006-002	1.00010	±0.00080	0.08872	0.06030	0.14902
HMI-006-003	1.00150	±0.00090	0.10179	0.06481	0.16660
HMI-006-004	1.00160	±0.00080	0.12990	0.07604	0.20594
IMF-020-001	1.00060	±0.00132	0.07125	0.03911	0.11036
IMF-020-002	1.00150	±0.00130	0.08534	0.04619	0.13152
IMF-020-003	1.00040	±0.00129	0.08820	0.04703	0.13523
IMF-020-004	1.00080	±0.00130	0.08881	0.04664	0.13544
IMF-020-005	1.00140	±0.00130	0.08711	0.04521	0.13232
IMF-020-006	1.00120	±0.00133	0.08061	0.04143	0.12204
IMF-020-007	1.00110	±0.00136	0.07037	0.03572	0.10609
IMF-020-008	1.00030	±0.00133	0.06790	0.03794	0.10583
IMF-020-009	1.00070	±0.00131	0.06353	0.03544	0.09897
IMF-022-001	1.00570	±0.00134	0.05667	0.03326	0.08992
IMF-022-005	1.00022	±0.00110	0.05323	0.03240	0.08563
IMF-022-006	1.00564	±0.00110	0.04678	0.03000	0.07678
IMF-022-007	1.00147	±0.00107	0.05132	0.03137	0.08269
IMI-001-002	1.00042	±0.00123	0.05310	0.03311	0.08621
IMI-001-003	1.00131	±0.00172	0.04800	0.03139	0.07939
IMI-001-004	1.00100	±0.00126	0.04361	0.02721	0.07081
PMF-013-001	1.00340	±0.00230	0.13102	0.06683	0.19785
PMF-014-001	1.00370	±0.00310	0.04144	0.02005	0.06149
PMF-040-001	1.00000	±0.00380	0.07461	0.03451	0.10912

APPENDIX B. CALCULATED ENDF/B-VII.1 AND ENDF/B-VIII.0 CRITICALITIES

Evaluation Identifier	Alpha-numerical Ordering	CSAS ENDF/B-VII.1	CSAS ENDF/B-VIII.0	MCNP ENDF/B-VII.1	MCNP ENDF/B-VIII.0
HMF-072-001	1	1.008625	1.004000	1.00853	1.00397
HMF-072-002	2	1.009461	1.004903	1.00955	1.00485
HMF-072-003	3	1.012248	1.011543	1.01236	1.01146
HMF-073-001	4	1.011725	1.003110	1.01134	1.00284
HMF-084-002	5	0.999535	0.998972	0.99945	0.99895
HMF-084-006	6	0.998638	0.994852	0.99857	0.99481
HMF-084-007	7	0.996709	0.998903	0.99741	0.99886
HMF-084-015	8	0.998033	0.997637	0.99810	0.99785
HMF-084-018	9	0.997558	0.995215	0.99718	0.99445
HMF-084-019	10	0.997277	0.998400	0.99740	0.99843
HMF-084-026	11	0.999964	0.999913	1.00038	0.99994
HMF-084-027	12	0.997246	0.997064	0.99759	0.99701
HMF-085-001	13	0.999074	0.999525	0.99906	0.99906
HMF-085-002	14	0.999535	0.998972	0.99945	0.99895
HMF-085-003	15	0.999878	0.998532	1.00002	0.99854
HMF-085-004	16	0.998848	0.997673	0.99878	0.99781
HMI-006-001	17	0.992957	0.995540	0.99294	0.99584
HMI-006-002	18	0.996944	1.000122	0.99689	1.00027
HMI-006-003	19	1.000844	1.003110	1.00076	1.00325
HMI-006-004	20	1.005763	1.003725	1.00730	1.00537
HMT-013-001	21	1.003726	1.001240	-	-
HMT-013-002	22	0.995121	0.991352	-	-
HMT-015-001	23	0.994261	0.991794	-	-
HST-014-001	24	0.993438	0.994209	0.99413	0.99480
HST-014-002	25	1.010041	1.011046	1.01061	1.01157
HST-014-003	26	1.018862	1.019937	1.01934	1.02052
HST-015-001	27	0.997513	0.998257	0.99823	0.99879
HST-015-002	28	0.989123	0.989653	0.98962	0.99032
HST-015-003	29	1.007449	1.008547	1.00809	1.00911
HST-015-004	30	1.012663	1.013785	1.01312	1.01426
HST-015-005	31	1.009061	1.010813	1.00971	1.01124
HST-016-001	32	0.989922	0.990107	0.99039	0.99100
HST-016-002	33	1.005484	1.006820	1.00626	1.00749
HST-016-003	34	1.024197	1.025944	1.02496	1.02647
HST-017-001	35	0.990649	0.991284	0.99139	0.99188
HST-017-002	36	0.980219	0.980568	0.98087	0.98127
HST-017-003	37	0.979440	0.979967	0.98000	0.98051
HST-017-004	38	0.997217	0.998624	0.99598	0.99719
HST-017-005	39	1.005025	1.006474	1.00578	1.00720

Evaluation Identifier	Alpha-numerical Ordering	CSAS ENDF/B-VII.1	CSAS ENDF/B-VIII.0	MCNP ENDF/B-VII.1	MCNP ENDF/B-VIII.0
HST-017-006	40	1.000916	1.002174	1.00166	1.00294
HST-017-007	41	1.004260	1.005579	1.00500	1.00632
HST-017-008	42	0.999097	1.001111	0.99992	1.00152
HST-018-001	43	0.989340	0.989448	0.99007	0.99042
HST-018-002	44	0.984094	0.983956	0.98776	0.98747
HST-018-003	45	0.988042	0.987848	0.98863	0.98861
HST-018-004	46	0.995914	0.997142	0.99682	0.99772
HST-018-005	47	0.990734	0.991380	0.99151	0.99215
HST-018-006	48	0.989784	0.990828	0.99069	0.99148
HST-018-007	49	1.003629	1.005253	1.00552	1.00689
HST-018-008	50	1.006099	1.007686	1.00708	1.00818
HST-018-009	51	1.002721	1.004084	1.00347	1.00481
HST-018-010	52	1.018134	1.020264	1.01932	1.02067
HST-018-011	53	1.020132	1.021940	1.02098	1.02261
HST-018-012	54	1.012928	1.015283	1.01400	1.01596
HST-019-001	55	0.996775	0.996135	0.99751	0.99703
HST-019-002	56	0.998148	0.998864	0.99912	0.99962
HST-019-003	57	0.993953	0.994291	0.99481	0.99569
IMF-020-001	58	1.008681	1.002075	1.00832	1.00179
IMF-020-002	59	1.010477	1.001935	1.01035	1.00168
IMF-020-003	60	1.009798	1.000899	1.00979	1.00064
IMF-020-004	61	1.010595	1.001484	1.01041	1.00115
IMF-020-005	62	1.010837	1.001528	1.01068	1.00135
IMF-020-006	63	1.009771	1.001177	1.00962	1.00075
IMF-020-007	64	1.009041	1.000970	1.00908	1.00080
IMF-020-008	65	1.008878	1.002410	1.00850	1.00191
IMF-020-009	66	1.007758	1.001857	1.00744	1.00160
IMF-022-001*	67	1.007440	1.003272	1.00717	1.00279
IMF-022-005*	68	1.002669	1.000908	1.00080	0.99878
IMF-022-006*	69	1.007132	1.006273	1.00274	1.00247
IMF-022-007*	70	1.004649	1.002924	1.00142	0.99970
IMI-001-002*	71	0.999204	0.999531	0.99350	0.99420
IMI-001-003*	72	0.995446	0.996491	0.98174	0.98368
IMI-001-004*	73	0.999516	0.999974	0.98518	0.98627
LCT-079-001^{+}	74	0.998519	0.996991	0.99789	-
LCT-079-002^{+}	75	0.998736	0.997469	0.99867	-
LCT-079-003^{+}	76	0.999271	0.997890	0.99903	-
LCT-079-004^{+}	77	0.999602	0.998174	0.99934	-
LCT-079-005^{+}	78	0.999640	0.998367	0.99900	-
LCT-079-006^{+}	79	0.998898	0.998724	0.99812	-
LCT-079-007^{+}	80	0.999798	0.999607	0.99957	-
LCT-079-008^{+}	81	1.000878	1.000743	1.00043	-
LCT-079-009^{+}	82	1.000445	1.000505	0.99984	-
LCT-079-010^{+}	83	1.001278	1.001352	1.00049	-
PMF-013-001	84	1.008542	1.002945	1.00809	1.00288
PMF-014-001	85	1.005991	0.998093	1.00648	0.99909

Evaluation Identifier	Alpha-numerical Ordering	CSAS ENDF/B-VII.1	CSAS ENDF/B-VIII.0	MCNP ENDF/B-VII.1	MCNP ENDF/B-VIII.0
PMF-040-001	86	0.996986	0.994139	0.99672	0.99415
PST-034-001	87	0.999638	0.996377	0.99980	0.99670
PST-034-002	88	1.001205	0.997571	1.00166	0.99790
PST-034-003	89	0.998988	0.994775	0.99941	0.99539
PST-034-004	90	1.001791	0.997608	1.00252	0.99825
PST-034-005	91	0.999152	0.994626	0.99986	0.99532
PST-034-006	92	1.000406	0.995753	1.00131	0.99647
PST-034-007	93	0.998217	0.997815	0.99861	0.99839
PST-034-008	94	0.998305	0.997900	0.99907	0.99853
PST-034-009	95	0.996943	0.996292	0.99763	0.99705
PST-034-010	96	0.996566	0.995445	0.99722	0.99646
PST-034-011	97	0.998059	0.996927	0.99880	0.99795
PST-034-012	98	0.997466	0.996281	0.99844	0.99741
PST-034-013	99	0.995660	0.994395	0.99688	0.99572
PST-034-014	100	0.995681	0.994220	0.99677	0.99560
PST-034-015	101	0.996081	0.994606	0.99725	0.99607
SMF-014-001	102	0.989454	0.993088	-	-

*IMF-022 and IMI-001 MCNP values were results of simplified rather than detailed models; the effect of cross section substitutions were similar

[+]LCT-079 MCNP ENDF/B-VII.1 values were taken from the ICSBEP evaluation, being one of the few evaluations with published and evaluated MCNP ENDF/B-VII.1 result

APPENDIX C. SELECTED BENCHMARK EXPERIMENTS AND THEIR ISOTOPE SUBSTITUTION C/E VALUES; BY ISOTOPE

C.1 Oxygen-16

Evaluation Identifier	O-16 ENDF/B-VIII.0 Criticality	ENDF/B-VII.1 C/E	O-16 ENDF/B-VIII.0 C/E	ENDF/B-VIII.0 C/E	O-16 ENDF/B-VIII.0 C/E Uncertainty
HMF-084-002	0.998592	13.5	-80.8	-42.8	±210.4
HMF-084-015	0.997610	-146.8	-189.1	-186.4	±210.3
HST-014-001	0.992122	-656.2	-787.8	-579.1	±280.2
HST-014-002	1.008927	1004.1	892.7	1104.6	±520.1
HST-014-003	1.017698	1886.2	1769.8	1993.7	±870.1
HST-015-001	0.996132	-248.7	-386.8	-174.3	±320.2
HST-015-002	0.987376	-1087.7	-1262.4	-1034.7	±340.2
HST-015-003	1.006029	744.9	602.9	854.7	±680.1
HST-015-004	1.011184	1266.3	1118.4	1378.5	±690.1
HST-015-005	1.008074	906.1	807.4	1081.3	±890.1
HST-016-001	0.988254	-1007.8	-1174.6	-989.3	±360.1
HST-016-002	1.004202	548.4	420.2	682.0	±690.1
HST-016-003	1.022963	2419.7	2296.3	2594.4	±790.1
HST-017-001	0.988845	-935.1	-1115.5	-871.6	±280.2
HST-017-002	0.978612	-1978.1	-2138.8	-1943.2	±400.1
HST-017-003	0.977805	-2056.0	-2219.5	-2003.3	±360.1
HST-017-004	0.995794	-278.3	-420.6	-137.6	±470.1
HST-017-005	1.003591	502.5	359.1	647.4	±580.1
HST-017-006	0.999514	91.6	-48.6	217.4	±550.1
HST-017-007	1.003087	426.0	308.7	557.9	±570.1
HST-017-008	0.997871	-90.3	-212.9	111.1	±670.1
HST-018-001	0.987765	-1066.0	-1223.5	-1055.2	±340.2
HST-018-002	0.982350	-1590.6	-1765.0	-1604.4	±460.1
HST-018-003	0.986280	-1195.8	-1372.0	-1215.2	±420.1
HST-018-004	0.994662	-408.6	-533.8	-285.8	±440.1
HST-018-005	0.989123	-926.6	-1087.7	-862.0	±460.1
HST-018-006	0.988340	-1021.6	-1166.0	-917.2	±450.1
HST-018-007	1.002325	362.9	232.5	525.3	±580.1
HST-018-008	1.004864	609.9	486.4	768.6	±560.1
HST-018-009	1.001378	272.1	137.8	408.4	±560.1
HST-018-010	1.017073	1813.4	1707.3	2026.4	±570.1
HST-018-011	1.018902	2013.2	1890.2	2194.0	±590.1
HST-018-012	1.011796	1292.8	1179.6	1528.3	±650.1
HST-019-001	0.994927	-322.5	-507.3	-386.5	±410.1
HST-019-002	0.996646	-185.2	-335.4	-113.6	±410.1

Evaluation Identifier, cont.	O-16 ENDF/B-VIII.0 Criticality	ENDF/B-VII.1 C/E	O-16 ENDF/B-VIII.0 C/E	ENDF/B-VIII.0 C/E	O-16 ENDF/B-VIII.0 C/E Uncertainty
HST-019-003	0.992386	-604.7	-761.4	-570.9	±670.1
IMF-022-006	1.007048	148.4	140.0	62.9	±109.8
IMF-022-007	1.003914	317.4	244.0	145.2	±107.3
LCT-079-001	0.996902	-144.1	-305.8	-296.9	±102.5
LCT-079-002	0.997199	-145.4	-299.0	-272.0	±102.5
LCT-079-003	0.997727	-128.8	-283.1	-266.9	±102.4
LCT-079-004	0.997991	-94.7	-255.8	-237.5	±102.4
LCT-079-005	0.998163	-82.0	-229.6	-209.2	±102.4
LCT-079-006	0.997718	-44.2	-162.3	-61.6	±73.7
LCT-079-007	0.998482	-36.2	-167.8	-55.3	±73.7
LCT-079-008	0.999535	12.8	-121.4	-0.7	±73.6
LCT-079-009	0.999271	14.5	-102.9	20.5	±73.7
LCT-079-010	1.000095	56.8	-61.5	64.2	±73.6
PST-034-001	0.998165	-36.2	-183.5	-362.3	±620.1
PST-034-002	1.000075	120.5	7.5	-242.9	±440.1
PST-034-003	0.997668	-101.2	-233.2	-522.5	±400.1
PST-034-004	1.000657	179.1	65.7	-239.2	±390.1
PST-034-005	0.997955	-84.8	-204.5	-537.4	±400.1
PST-034-006	0.999256	40.6	-74.4	-424.7	±420.1
PST-034-007	0.996480	-178.3	-352.0	-218.5	±570.1
PST-034-008	0.996845	-169.5	-315.5	-210.0	±550.1
PST-034-009	0.995281	-305.7	-471.9	-370.8	±520.1
PST-034-010	0.994788	-343.4	-521.2	-455.5	±520.1
PST-034-011	0.996300	-194.1	-370.0	-307.3	±480.1
PST-034-012	0.995748	-253.4	-425.2	-371.9	±420.1
PST-034-013	0.994150	-434.0	-585.0	-560.5	±430.1
PST-034-014	0.993908	-431.9	-609.2	-578.0	±440.1
PST-034-015	0.994576	-391.9	-542.4	-539.4	±420.1

C.2 Iron-56

Evaluation Identifier	Fe-56 ENDF/B-VIII.0 Criticality	ENDF/B-VII.1 C/E	Fe-56 ENDF/B-VIII.0 C/E	ENDF/B-VIII.0 C/E	Fe-56 ENDF/B-VIII.0 C/E Uncertainty
HMF-072-1	1.008620	953.4	952.9	490.4	±240.4
HMF-072-2	1.009897	925.9	969.5	470.2	±240.2
HMF-072-3	1.012084	1063.1	1046.7	992.7	±689.0
HMF-084-007	0.997876	-279.2	-162.5	-59.7	±200.4
HMF-084-019	0.997912	-232.4	-168.9	-120.0	±190.3
HMF-084-026	1.000559	66.4	126.0	61.3	±220.4
HMF-084-027	0.997719	-215.5	-168.2	-233.7	±200.4
HMF-085-3	0.996838	-436.8	-266.3	-97.6	±460.3
HMT-013-001	1.004121	312.4	351.9	64.0	±220.1
HMT-013-002	0.995144	-218.5	-216.2	-596.4	±200.8
HMT-015-001	0.994295	-583.8	-580.4	-830.5	±210.2
HST-017-6	1.001154	91.6	115.4	217.4	±550.1
HST-017-8	0.999332	-90.3	-66.8	111.1	±670.1
HST-018-005	0.990912	-926.6	-908.8	-862	±460.1
HST-018-006	0.990287	-1021.6	-971.3	-917.2	±450.1
HST-018-008	1.006448	609.9	644.8	768.6	±560.1
HST-018-010	1.018241	1813.4	1824.1	2026.4	±570.1
IMF-020-004	1.004062	978.7	958.5	68.3	±107.3
IMF-020-005	1.010393	942.4	940.7	12.8	±130.3
IMF-020-006	1.010820	856.1	849.6	-2.3	±130.2
IMF-020-007	1.009706	793.2	785.6	-13.0	±133.2
IMF-022-007	1.008965	317.4	258.8	145.2	±136.2
PMF-013-1	1.008697	512.5	527.9	-45.3	±229.4
PMF-014-1	1.006240	228.3	253.1	-558.6	±309.0
SMF-014-001	0.990761	-1064.5	-933.8	-701.1	±390.1

C.3 Copper-63

Evaluation Identifier	Cu-63 ENDF/B-VIII.0 Criticality	ENDF/B-VII.1 C/E	Cu-63 ENDF/B-VIII.0 C/E	ENDF/B-VIII.0 C/E	Cu-63 ENDF/B-VIII.0 C/E Uncertainty
HMF-072-001	0.998173	953.4	-92.8	490.4	±240.4
HMF-072-002	0.999116	925.9	-108.4	470.2	±240.2
HMF-072-003	1.004593	1063.1	298.8	992.7	±689.0
HMF-073-001	1.000607	1132.0	20.7	270.9	±160.2
HMF-084-006	0.994310	-76.2	-509.3	-455.1	±240.4
HMF-084-018	0.995023	-194.3	-447.9	-428.7	±220.3
HMF-085-001	0.993688	48.5	-611.3	-527.2	±290.2
HMF-085-002	0.995555	466.2	-414.6	-290.9	±310.3
HMF-085-004	0.997773	34.6	-182.8	418.0	±290.3
HMI-006-001	0.990422	-475.4	-729.5	-216.5	±80.8
HMI-006-002	0.993966	-315.6	-613.3	2.2	±80.6
HMI-006-003	0.997066	-65.5	-442.7	160.8	±90.4
HMI-006-004	1.001045	415.6	-55.4	212.2	±80.5
IMF-020-001	1.002973	807.6	237.2	147.4	±132.3
IMF-020-002	1.003436	896.4	193.3	43.4	±130.2
IMF-020-003	1.002469	939.4	206.8	49.9	±129.3
IMF-020-004	1.003185	978.7	238.3	68.3	±130.3
IMF-020-005	1.003588	942.4	218.5	12.8	±130.2
IMF-020-006	1.003104	856.1	190.2	-2.3	±133.2
IMF-020-007	1.003198	793.2	209.6	-13.0	±136.2
IMF-020-008	1.003371	857.5	307.0	210.9	±133.3
IMF-020-009	1.002761	705.3	206.0	115.6	±131.3
IMF-022-001	1.003863	173.0	-182.7	-241.4	±133.6
IMF-022-005	0.999661	244.8	-55.9	68.8	±110.4
IMF-022-006	1.005090	148.4	-54.7	62.9	±109.8
IMF-022-007	1.001908	317.4	43.7	145.2	±107.3
IMI-001-002	0.996466	-121.5	-395.2	-88.9	±123.4
IMI-001-003	0.993087	-585.6	-821.2	-481.3	±172.1
IMI-001-004	0.997422	-148.3	-357.4	-102.5	±126.3
PMF-013-001	1.001450	512.5	-194.3	-45.3	±229.4
PMF-014-001	1.003865	228.3	16.4	-558.6	±309.0
PMF-040-001	0.993933	-301.4	-606.7	-586.1	±380.1

C.4 Copper-65

Evaluation Identifier	Cu-65 ENDF/B-VIII.0 Criticality	ENDF/B-VII.1 C/E	Cu-65 ENDF/B-VIII.0 C/E	ENDF/B-VIII.0 C/E	Cu-65 ENDF/B-VIII.0 C/E Uncertainty
HMF-072-001	1.010139	953.4	1104.9	490.4	±240.4
HMF-072-002	1.011329	925.9	1112.7	470.2	±240.2
HMF-072-003	1.013268	1063.1	1164.9	992.7	±689.0
HMF-073-001	1.014713	1132.0	1430.7	270.9	±160.2
HMF-084-006	0.999652	-76.2	25.2	-455.1	±240.4
HMF-084-018	0.998123	-194.3	-137.8	-428.7	±220.3
HMF-085-001	1.001515	48.5	171.5	-527.2	±290.2
HMF-085-002	1.006256	466.2	655.8	-290.9	±310.3
HMF-085-004	1.000516	34.6	91.6	418.0	±290.3
HMI-006-001	0.992334	-475.4	-537.8	-216.5	±80.8
HMI-006-002	0.996357	-315.6	-374.3	2.2	±80.6
HMI-006-003	1.000662	-65.5	-83.7	160.8	±90.4
HMI-006-004	1.007173	415.6	556.4	212.2	±80.5
IMF-020-001	1.009750	807.6	914.5	147.4	±132.3
IMF-020-002	1.011582	896.4	1006.7	43.4	±130.2
IMF-020-003	1.010651	939.4	1024.7	49.9	±129.3
IMF-020-004	1.011299	978.7	1049.1	68.3	±130.3
IMF-020-005	1.011602	942.4	1018.8	12.8	±130.2
IMF-020-006	1.010452	856.1	924.1	-2.3	±133.2
IMF-020-007	1.009436	793.2	832.7	-13.0	±136.2
IMF-020-008	1.010102	857.5	979.9	210.9	±133.3
IMF-020-009	1.009132	705.3	842.6	115.6	±131.3
IMF-022-001	1.008722	173.0	300.5	-241.4	±133.6
IMF-022-005	1.003732	244.8	351.1	68.8	±110.4
IMF-022-006	1.008127	148.4	247.3	62.9	±109.8
IMF-022-007	1.005479	317.4	400.3	145.2	±107.3
IMI-001-002	1.000143	-121.5	-27.7	-88.9	±123.4
IMI-001-003	0.995747	-585.6	-555.6	-481.3	±172.1
IMI-001-004	1.000192	-148.3	-80.7	-102.5	±126.3
PMF-013-001	1.010069	512.5	664.6	-45.3	±229.4
PMF-014-001	1.006242	228.3	253.3	-558.6	±309.0
PMF-040-001	0.997765	-301.4	-223.5	-586.1	±380.1

C.5 Elemental Copper

Evaluation Identifier	Cu ENDF/B-VIII.0 Criticality	ENDF/B-VII.1 C/E	Cu ENDF/B-VIII.0 C/E	ENDF/B-VIII.0 C/E	Cu ENDF/B-VIII.0 C/E Uncertainty
HMF-072-001	0.999689	953.4	59.0	490.4	±240.4
HMF-072-002	1.000754	925.9	55.4	470.2	±240.2
HMF-072-003	1.005623	1063.1	401.7	992.7	±689.0
HMF-073-001	1.003542	1132.0	314.1	270.9	±160.2
HMF-084-006	0.995030	-76.2	-437.3	-455.1	±240.4
HMF-084-018	0.995449	-194.3	-405.3	-428.7	±220.3
HMF-085-001	0.994861	48.5	-494.0	-527.2	±290.2
HMF-085-002	0.997314	466.2	-238.7	-290.9	±310.3
HMF-085-004	0.998041	34.6	-156.0	418.0	±290.3
HMI-006-001	0.989594	-475.4	-812.5	-216.5	±80.8
HMI-006-002	0.993239	-315.6	-686.0	2.2	±80.6
HMI-006-003	0.996964	-65.5	-452.9	160.8	±90.4
HMI-006-004	1.002088	415.6	48.7	212.2	±80.5
IMF-020-001	1.003985	807.6	338.3	147.4	±132.3
IMF-020-002	1.004271	896.4	276.7	43.4	±130.2
IMF-020-003	1.003161	939.4	276.0	49.9	±129.3
IMF-020-004	1.003460	978.7	265.8	68.3	±130.3
IMF-020-005	1.003944	942.4	254.0	12.8	±130.2
IMF-020-006	1.003457	856.1	225.4	-2.3	±133.2
IMF-020-007	1.003670	793.2	256.7	-13.0	±136.2
IMF-020-008	1.004476	857.5	417.5	210.9	±133.3
IMF-020-009	1.003937	705.3	323.5	115.6	±131.3
IMF-022-001	1.005152	173.0	-54.5	-241.4	±133.6
IMF-022-005	1.000420	244.8	20.0	68.8	±110.4
IMF-022-006	1.005676	148.4	3.6	62.9	±109.8
IMF-022-007	1.002355	317.4	88.4	145.2	±107.3
IMI-001-002	0.997124	-121.5	-329.5	-88.9	±123.4
IMI-001-003	0.993470	-585.6	-783.0	-481.3	±172.1
IMI-001-004	0.997565	-148.3	-343.2	-102.5	±126.3
PMF-013-001	1.003178	512.5	-22.1	-45.3	±229.4
PMF-014-001	1.004551	228.3	84.8	-558.6	±309.0
PMF-040-001	0.994714	-301.4	-528.6	-586.1	±380.1

APPENDIX D. DIRECT PERTURBATIONAL CONFIRMATION OF SELECT SENSITIVITIES

Evaluation Identifier	Material	TSUNAMI Sensitivity	TSUNAMI Uncertainty	Direct Perturbation Sensitivity	Direct Perturbation Uncertainty	Difference in Standard Deviations
HMF-072-001	^{63}Cu	1.29E-01	5.05E-04	0.1278	0.0008	1.02
	^{65}Cu	7.30E-02	2.82E-04	0.0732	0.0005	0.27
	^{235}U	3.99E-02	3.82E-05	0.0403	0.0002	1.75
	^{235}U	3.95E-02	3.81E-05	0.0396	0.0002	0.43
	^{235}U	3.87E-02	3.81E-05	0.0386	0.0002	0.52
	^{235}U	3.84E-02	3.70E-05	0.0383	0.0002	0.39
HMF-072-002	^{63}Cu	1.29E-01	4.96E-04	0.1285	0.0008	0.94
	^{65}Cu	7.32E-02	2.74E-04	0.0736	0.0005	0.81
	^{235}U	4.00E-02	3.80E-05	0.0399	0.0003	0.29
	^{235}U	3.97E-02	3.79E-05	0.0396	0.0002	0.24
	^{235}U	3.88E-02	3.76E-05	0.0389	0.0002	0.19
	^{235}U	3.85E-02	3.70E-05	0.0386	0.0002	0.37
HMF-072-003	^{63}Cu	1.15E-01	5.01E-04	0.1125	0.0007	2.80
	H-Poly	7.96E-02	1.55E-04	0.0800	0.0005	0.87
	^{65}Cu	6.80E-02	2.89E-04	0.0674	0.0004	1.02
	^{235}U	4.45E-02	4.64E-05	0.0446	0.0003	0.45
	^{235}U	4.34E-02	4.48E-05	0.0434	0.0003	0.06
	^{235}U	4.28E-02	4.51E-05	0.0430	0.0003	0.85
HMF-073-001	^{235}U	3.72E-01	9.08E-05	0.3737	0.0024	0.90
	^{235}U	1.57E-01	5.83E-05	0.1586	0.0010	1.89
	^{63}Cu	9.77E-02	2.37E-04	0.0981	0.0006	0.55
	^{63}Cu	7.35E-02	2.50E-04	0.0733	0.0005	0.55
	^{65}Cu	5.01E-02	1.33E-04	0.0502	0.0003	0.40
	^{65}Cu	3.82E-02	1.41E-04	0.0379	0.0002	0.88
HMI-006-001	C	3.98E-01	2.00E-03	0.3948	0.0025	1.01
	^{235}U	2.87E-01	1.02E-04	0.2865	0.0019	0.29
	^{63}Cu	7.83E-02	5.45E-04	0.0774	0.0005	1.19
	^{63}Cu	5.71E-02	3.42E-04	0.0565	0.0004	1.23
HMI-006-002	C	3.75E-01	1.59E-03	0.3737	0.0025	0.45
	^{235}U	3.14E-01	1.07E-04	0.3155	0.0020	0.95
	^{63}Cu	8.87E-02	5.14E-04	0.0883	0.0006	0.53
	^{63}Cu	6.03E-02	3.17E-04	0.0595	0.0004	1.62

Evaluation Identifier	Material	TSUNAMI Sensitivity	TSUNAMI Uncertainty	Direct Perturbation Sensitivity	Direct Perturbation Uncertainty	Difference in Standard Deviations
HMI-006-003	^{235}U	3.51E-01	1.10E-04	0.3530	0.0023	0.82
	C	3.32E-01	1.15E-03	0.3341	0.0021	0.77
	^{63}Cu	1.02E-01	4.88E-04	0.1018	0.0006	0.02
	^{63}Cu	6.48E-02	2.94E-04	0.0643	0.0004	0.94
HMI-006-004	^{235}U	4.24E-01	1.13E-04	0.4229	0.0026	0.29
	C	2.25E-01	6.22E-04	0.2255	0.0014	0.21
	^{63}Cu	1.30E-01	4.67E-04	0.1285	0.0008	1.48
	^{63}Cu	7.60E-02	2.73E-04	0.0766	0.0005	0.99
HMF-084-002	^{235}U	7.38E-01	8.38E-05	0.7295	0.0088	0.96
	^{16}O	6.67E-02	2.78E-05	0.0670	0.0009	0.32
	^{27}Al	4.10E-02	2.27E-05	0.0408	0.0006	0.43
HMF-084-015	^{235}U	7.57E-01	8.19E-05	0.7519	0.0055	0.99
	^{16}O	4.10E-02	1.75E-05	0.0404	0.0006	1.06
	^{27}Al	2.52E-02	1.40E-05	0.0249	0.0004	0.75
LCT-079-001	^{1}H	3.37E-01	3.71E-03	0.3425	0.0047	0.94
	^{235}U	1.44E-01	8.93E-05	0.1433	0.0020	0.19
	^{16}O	3.44E-02	2.20E-04	0.0344	0.0005	0.03
	^{16}O	3.28E-02	4.45E-04	0.0340	0.0005	1.78
	^{16}O	2.17E-02	3.89E-04	0.0220	0.0003	0.67
LCT-079-002	^{1}H	3.41E-01	3.58E-03	0.3418	0.0047	0.20
	^{235}U	1.44E-01	8.74E-05	0.1468	0.0020	1.62
	^{16}O	3.47E-02	2.17E-04	0.0353	0.0005	1.01
	^{16}O	3.27E-02	4.42E-04	0.0333	0.0005	0.87
	^{16}O	2.13E-02	4.03E-04	0.0214	0.0003	0.21
LCT-079-003	^{1}H	3.39E-01	3.28E-03	0.3333	0.0033	1.20
	^{235}U	1.47E-01	7.56E-05	0.1463	0.0014	0.61
	^{16}O	3.37E-02	1.89E-04	0.0331	0.0003	1.52
	^{16}O	3.21E-02	4.03E-04	0.0323	0.0003	0.26
	^{16}O	2.15E-02	3.51E-04	0.0209	0.0002	1.58
LCT-079-004	^{1}H	3.33E-01	3.06E-03	0.3324	0.0033	0.07
	^{235}U	1.50E-01	7.93E-05	0.1506	0.0015	0.51
	^{16}O	3.30E-02	1.90E-04	0.0334	0.0003	0.97
	^{16}O	3.15E-02	3.90E-04	0.0315	0.0003	0.08
	^{16}O	2.05E-02	3.52E-04	0.0205	0.0002	0.01

Evaluation Identifier	Material	TSUNAMI Sensitivity	TSUNAMI Uncertainty	Direct Perturbation Sensitivity	Direct Perturbation Uncertainty	Difference in Standard Deviations
LCT-079-005	^{1}H	3.30E-001	3.29E-003	0.3290	0.0047	0.13
	^{235}U	1.54E-001	8.40E-005	0.1526	0.0022	0.68
	^{16}O	3.28E-002	2.04E-004	0.0321	0.0005	1.35
	^{16}O	3.04E-002	4.08E-004	0.0310	0.0004	0.97
LCT-079-006	^{235}U	2.03E-001	6.20E-005	0.2031	0.0020	0.17
	^{1}H	1.91E-001	6.02E-003	0.1955	0.0018	0.78
	^{16}O	4.53E-002	5.27E-004	0.0458	0.0004	0.67
	^{16}O	2.65E-002	1.59E-004	0.0266	0.0003	0.35
LCT-079-007	^{1}H	2.09E-001	6.66E-003	0.2025	0.0042	0.80
	^{235}U	2.04E-001	7.44E-005	0.2037	0.0019	0.02
	^{16}O	4.64E-002	5.70E-004	0.0460	0.0005	0.49
	^{16}O	2.63E-002	1.82E-004	0.0267	0.0003	1.46
LCT-079-008	^{1}H	2.09E-001	7.64E-005	0.2067	0.0020	1.10
	^{235}U	1.89E-001	6.89E-003	0.1892	0.0019	0.03
	^{16}O	4.43E-002	6.23E-004	0.0436	0.0004	0.95
	^{16}O	2.56E-002	1.74E-004	0.0257	0.0002	0.28
LCT-079-009	^{1}H	2.13E-001	7.82E-005	0.2129	0.0021	0.20
	^{235}U	1.93E-001	6.95E-003	0.1865	0.0007	0.98
	^{16}O	4.40E-002	6.20E-004	0.0437	0.0004	0.29
	^{16}O	2.50E-002	1.75E-004	0.0253	0.0002	1.02
LCT-079-010	^{1}H	2.20E-001	8.31E-005	0.2201	0.0021	0.09
	^{235}U	1.73E-001	6.79E-003	0.1748	0.0017	0.24
	^{16}O	4.10E-002	6.14E-004	0.0397	0.0004	1.77
	^{16}O	2.43E-002	1.76E-004	0.0244	0.0002	0.07

All differences between direct perturbation confirmations and TSUNAMI results are within 5%, with a maximum of 3.68%, and all absolute differences are less than 0.01, with a maximum of 0.0084. All but one perturbations are within 2 sigma of TSUNAMI values. These are closely related to sensitivity data standards for the VALID library and will ultimately be revised for further precision before review and inclusion in the collection [40].

REFERENCES

[1] D.A. Brown, et al., “ENDF/B-VIII.0: The 8th Major Release of the Nuclear Reaction Data Library with CIELO-project Cross Sections, New Standards and Thermal Scattering Data”, *Nuclear Data Sheets*, Volume 148, Pages 1-142, 2018.

[2] A. Chambers, “Five-Year Execution Plan for the Mission and Vision of the United States Department of Energy Nuclear Criticality Safety Program, October 2019, Revision 1”, https://ncsp.llnl.gov/docs/FY20-24_NCSP_Five-Year_Execution_Plan.pdf

[3] J. Bess, ed., *International Handbook of Evaluated Criticality Safety Benchmark Experiments (ICSBEP).* Paris: Organization for Economic Co-operation and Development-Nuclear Energy Agency (OECD-NEA). NEA/NSC/DOC (95)03, 2018.

[4] Chadwick, et al., “The CIELO Collaboration: Neutron Reactions on ^{1}H, ^{16}O, ^{56}Fe, ^{235,238}U, and ^{239}Pu”, Nuclear Data Sheets, Volume 118, Pages 1-25, 2014.

[5] M. Chadwick, et al., “ENDF/B-VII.1: Nuclear Data for Science and Technology: Cross Sections, Covariances, Fission Product Yields, and Decay Data", *Nuclear Data Sheets*, Volume 112, Pages 2887-2996, 2011.

[6] Edited by David Brown et al., “Evaluated Nuclear Data File (ENDF)”, https://www.nndc.bnl.gov/exfor/endf00.jsp.

[7] M.B. Chadwick, et al., "CIELO Collaboration Summary Results: International Evaluations of Neutron Reactions on Uranium, Plutonium, Iron, Oxygen and Hydrogen", Nuclear Data Sheets, Volume 148, Pages 189-213, 2018. https://doi.org/10.1016/j.nds.2018.02.003.

[8] Herman, M. et al., "Evaluation of Neutron Reactions on Iron Isotopes for CIELO and ENDF/B-VIII.0", Nuclear Data Sheets, Volume 148, Pages 214-253, 2018. DOI: 10.1016/j.nds.2018.02.004

[9] Grahn, Per, et al. “Spent Nuclear Fuel for Disposal in the KBS-3 Repository” Svensk Kärnbränslehantering AB, 2010

[10] J. Bess, ed., DICE: User's Manual. Paris: Organization for Economic Co-operation and Development-Nuclear Energy Agency (OECD-NEA). NEA/NSC/DOC (95)03/II, 2019.

[11] SCALE Training Course: SCALE Sensitivity/Uncertainty Analysis and Uncertainty Quantification for Criticality Safety Validation. B.J. Marshall, Vlad Sobes, and Justin Clarity

[12] B. T. Rearden, M. L. Williams, M. A. Jessee, D. E. Mueller and D. A. Wiarda, "Sensitivity and Uncertainty Analysis Capabilities and Data in SCALE", *Nuclear Technology*, Volume 174(2), Pages 236–288, 2011.

[13] B. T. Rearden and M.A. Jessee, Eds., *SCALE Code System*, ORNL/TM-2005/39, Version 6.2.3, Oak Ridge National Laboratory, Oak Ridge, Tennessee (2018).

[14] C.J. Werner, et al., "MCNP6.2 Release Notes", Los Alamos National Laboratory, Report LA-UR-18-20808 (2018).

[15] "Nuclear Data Libraries from Los Alamos National Laboratory", https://nucleardata.lanl.gov/index.html

[16] ZEUS: Fast-spectrum Critical Assemblies with an Iron-HEU Core Surrounded by a Copper Reflector. Technical Report HEU-MET-FAST-072, International Criticality Safety Benchmark Evaluation Project, 2006.

[17] The Unmoderated ZEUS Experiment: A Cylindrical HEU Core Surrounded by a Copper Reflector. Technical Report HEU-MET-FAST-073, International Criticality Safety Benchmark Evaluation Project, 2005.

[18] HEU Metal Cylinders with Magnesium, Titanium, Aluminum, Graphite, Mild Steel, Nickel, Copper, Cobalt, Molybdenum, Natural Uranium, Tungsten, Beryllium, Aluminum Oxide, Molybdenum Carbine, and Polyethylene Reflectors. Technical Report HEU-MET-FAST-084, International Criticality Safety Benchmark Evaluation Project, 2007.

[19] Highly Enriched Uranium Metal Spheres Surrounded by Copper, Cast Iron, Nickel, Nickel-Copper-Zinc Alloy, Thorium, Tungsten Alloy, or Zinc Reflectors. Technical Report HEU-MET-FAST-085, International Criticality Safety Benchmark Evaluation Project, 2007.

[20] The Initial Set of ZEUS Experiments: Intermediate-Spectrum Critical Assemblies with a Graphite-HEU Core Surrounded by a Copper Reflector. Technical Report HEU-MET-INTER-006, International Criticality Safety Benchmark Evaluation Project, 2004.

[21] Polyethylene Reflected and Moderated Highly Enriched Uranium Systems with Iron. Technical Report HEU-MET-THERM-013, International Criticality Safety Benchmark Evaluation Project, 2003.

[22] 2x2 Array of Highly Enriched Uranium with Iron, Moderated and Reflected by Polyethylene. Technical Report HEU-MET-THERM-015, International Criticality Safety Benchmark Evaluation Project, 2005.

[23] Uranium Nitrate Solution (70gU/l) with Gadolinium. Technical Report HEU-SOL-THERM-014, International Criticality Safety Benchmark Evaluation Project, 1998.

[24] Uranium Nitrate Solution (100gU/l) with Gadolinium. Technical Report HEU-SOL-THERM-015, International Criticality Safety Benchmark Evaluation Project, 1998.

[25] Uranium Nitrate Solution (150gU/l) with Gadolinium. Technical Report HEU-SOL-THERM-016, International Criticality Safety Benchmark Evaluation Project, 1998.

[26] Uranium Nitrate Solution (200gU/l) with Gadolinium. Technical Report HEU-SOL-THERM-017, International Criticality Safety Benchmark Evaluation Project, 1998.

[27] Uranium Nitrate Solution (300gU/l) with Gadolinium. Technical Report HEU-SOL-THERM-018, International Criticality Safety Benchmark Evaluation Project, 2000.

[28] Uranium Nitrate Solution (400gU/l) with Gadolinium. Technical Report HEU-SOL-THERM-019, International Criticality Safety Benchmark Evaluation Project, 1998.

[29] The FR0 Series 1: Copper-Reflected “Cylindrical” Uranium (20% 235U) Metal. Technical Report IEU-MET-FAST-020, International Criticality Safety Benchmark Evaluation Project, 2012.

[30] The FR0 Experiments with Diluted 20%-Enriched “Cylindrical” Uranium Metal Reflected by Copper. Technical Report IEU-MET-FAST-022, International Criticality Safety Benchmark Evaluation Project, 2011.

[31] The FR0 Experiments with Diluted 20%-Enriched “Cylindrical” Uranium Metal Reflected by Copper. Technical Report IEU-MET-INTER-001, International Criticality Safety Benchmark Evaluation Project, 2011.

[32] Water Moderated U(4.31)O_2 Fuel Rod Lattices Containing Rhodium Foils. Technical Report LEU-COMP-THERM-079, International Criticality Safety Benchmark Evaluation Project, 2018.

[33] Copper-Reflected Array of Plutonium Fuel Rods. Technical Report PU-MET-FAST-013, International Criticality Safety Benchmark Evaluation Project, 1996.

[34] Nickel-Reflected Array of Plutonium Fuel Rods. Technical Report PU-MET-FAST-014, International Criticality Safety Benchmark Evaluation Project, 1999.

[35] Spherical Assembly of 239Pu (δ, 98%) with a 1.6-cm Copper Reflector. Technical Report PU-MET-FAST-040, International Criticality Safety Benchmark Evaluation Project, 1998.

[36] Plutonium (8.3 wt.% ^{240}Pu) Nitrate Solution with Gadolinium in Water-Reflected 24-inch Diameter Cylinder. Technical Report PU-SOL-THERM-034, International Criticality Safety Benchmark Evaluation Project, 2007.

[37] Neptunium-237 Sphere Surrounded by Highly Enriched Uranium and Reflected by Low-Carbon Steel. Technical Report SPEC-MET-FAST-014, International Criticality Safety Benchmark Evaluation Project, 2004.

[38] Weisstein, Eric W. "Root-Mean-Square." From MathWorld--A Wolfram Web Resource. https://mathworld.wolfram.com/Root-Mean-Square.html

[39] Geary, R. C., “The Ratio of the Mean Deviation to the Standard Deviation as a Test of Normality”. Biometrika, 27(3/4), Page 312, 1935

[40] W. J. Marshall and B. T. Rearden, “The SCALE Verified, Archived Library of Inputs and Data–VALID”, ANS Nuclear Criticality Safety Division Topical Meetings (NCSD2013), Wilmington, NC, September 29–October 3, 2013.